AKATSUKI Reverse Engineering Study

Full Report

Team 9

P. Code	Surname	Name
10847166	Alberghetti	Marco
11066730	D'Aloisio	Giovanni Nicola
10674015	Pifano	Nicola
11090696	Cancela Sanchez	Loreta
11108295	D'Agostini Barsanti	Fernanda
10749621	Maggi	Giacomo

Space System Engineering and Operations

Prof: M. Lavagna
L. Bianchi, M. Bussolino

M.Sc Space Engineering
A.Y. 2025-2026

Cover image credit: AKATSUKI mission logo, sourced from JAXA.

Change log	
Issue	*Comments*
1	First consolidated release — merges Assignments #1, #2.1, #2.2, #3, #4, #5, #6, #7, #8, #9.

Contents

List of Acronyms

C/N_0 Carrier-to-Noise Density Ratio.

C_3 Characteristic Energy.

E_b/N_0 Energy per Bit to Noise Spectral Density Ratio.

H_a Apoapsis Altitude.

H_p Periapsis Altitude.

I_{sp} Specific Impulse.

J_2 Second Zonal Harmonic of Gravitational Field.

$R_{\mathbf{C}}$ Convolutional Code Rate.

$R_{\mathbf{RS}}$ Reed–Solomon Code Rate.

T Orbital Period.

$T_{\mathbf{sys}}$ Equivalent Noise Temperature.

V_∞ Hyperbolic Excess Velocity.

V_{MPP} Voltage at Maximum Power Point.

ΔV Velocity Increment.

i Orbital Inclination.

3BP Three-Body Perturbation.

ACM Accelerometer.

ADCS Attitude Determination and Control System.

AKE Absolute Knowledge Error.

Al Aluminum.

AM0 Air Mass Zero.

AOCS Attitude and Orbit Control Subsystem.

AOCU Attitude and Orbit Control Unit.

APE Absolute Performance Error.

APV Apoapsis/Periapsis Velocity Adjustment Maneuver.

AR Anti-Reflection.

ATC Active Thermal-Control.

AU Astronomical Unit.

B/U Backup Maneuver.

BER Bit Error Rate.

BOL Beginning Of Life.

BPSK Binary Phase Shift Keying.

CCD Charge-Coupled Device.

CCSDS Consultative Committee for Space Data Systems.

CDF Concurrent Design Facility.

CFD Computational Fluid Dynamics.

CFRP Carbon Fiber Reinforced Plastic.

CMD Command.

CMG Cerium-doped Micro-Sheet Glass.

CoM Center of Mass.

CONF Configuration.

ConOps Conceptual Operations.

CR3BP Circular Restricted Three-Body Problem.

CSS Coarse Sun Sensor.

Cu copper.

DC Direct Current.

DE Digital Electronics.

Det Deterministic Margin.

DH Data Handling.

DL Downlink.

DOD Depth Of Discharge.

DOR Differential One-way Ranging.

DPU Data Processing Unit.

DRAG Aerodynamic Drag.

DRV Driving Unit.

DSN Deep Space Network.

ECSS European Cooperation for Space Standardization.

EIRP Effective Isotropic Radiated Power.

EOL End Of Life.

EPS Electrical Power Subsystem.

ESA European Space Agency.

FDIR Fault Detection, Isolation, and Recovery.

FoV Field of View.

FPGA Field-Programmable Gate Array.

FSS Fine Sun Sensor.

FW Filter Wheel.

GA Genetic Algorithm.

GaAs Gallium Arsenide.

GG Gravity Gradient.

GHe Gaseous Helium.

GNC Guidance, Navigation & Control.

He Helium.

HGA High-Gain Antenna.

HK Housekeeping.

HKT Housekeeping Telemetry.

HP High Power.

IMU Inertial Measurement Unit.

InGaP/GaAs/Ge Indium Gallium Phosphide/Gallium Arsenide/Germanium.

IR Infrared.

IR1 1-µm Camera.

IR2 2-µm Camera.

IRU Inertial Reference Unit.

ISAS Institute of Space and Astronautical Science.

ITU International Telecommunication Union.

JAXA Japan Aerospace Exploration Agency.

JP Japan.

JPL Jet Propulsion Laboratory.

LAC Lightning and Airglow Camera.

LD Launcher Dispersion.

LEO Low Earth Orbit.

LGA Low-Gain Antenna.

Li Lithium.

LIR Longwave Infrared Camera.

LOS Line of Sight.

LP Low Power.

LV Launch Vehicle.

MA Mission Analysis.

MAG Magnetic Disturbances.

MAR-DV Mission Analysis Requirement – ΔV Margin.

Max-Q Maximum Dynamic Pressure.

MECH Mechanism.

MGA Medium-Gain Antenna.

MIPS Million Instructions Per Second.

MLI Multi-Layer Insulation.

MON-3 Mixed Oxides of Nitrogen (97% Nitrogen Tetroxide, 3% Nitric Oxide).

MPPT Maximum Power Point Tracking.

N_2H_4 Hydrazine.

Nav/App Navigation/Approach.

NGO Needs, Goals, and Objectives.

NiCd Nickel-Cadmium.

NiH_2 Nickel–Hydrogen.

NIR Near-Infrared.

OA Global Imaging.

OASPL Overall Sound Pressure Level.

OB Close-Up Imaging.

OBC On-Board Computer.

OBDH On-Board Data Handling.

OC Limb Imaging.

OD Zonal Scan.

OE Eclipse Observations.

OF Radio Occultation.

OME Orbital Maneuvering Engine.

OSR Optical Solar Reflector.

PAE Power-Added Efficiency.

PCDU Power Conditioning and Distribution Unit.

PCU Power Control Unit.

PD Proportional-Derivative.

PL Payload.

PM Phase Modulation.

PS Propulsion System.

PSD Power Spectrum Density.

PSO Primary Scientific Objective.

PTC Passive Thermal-Control.

PV Photovoltaic.

RCS Reaction Control System.

RF Radio Frequency.

RS Radio Science.

RSS Root Sum Square.

RTG Radioisotope Thermoelectric Generator.

RTP Reversible Thermal Panel.

RW Reaction Wheel.

RX Receiver/Received.

S/C Spacecraft.

SADA Solar Array Drive Assembly.

SAP Solar Array Paddle.

SAPs Solar Array Paddles.

SBD Solar Array Blocking Diode.

Si Silicon.

Si_3N_4 Silicon Nitride.

SK Station Keeping.

SNR Signal-to-Noise Ratio.

SOC Science Operation Center.

SoC State of Charge.

SPS Sun Presence Sensor.

SPSO Supporting Primary Scientific Objective.

SQP Sequential Quadratic Programming.

SR System Resource.

SRP Solar Radiation Pressure.

SRS Shock Response Spectrum.

SSD Solid-State Drive.

SSO Secondary Scientific Objective.

SSPA Solid-State Power Amplifier.

SSR Solid State Recorder.

SSR Series-Switching Regulator.

STR Structure.

STT Star Tracker.

TCM Trajectory Correction Maneuver.

TCS Thermal Control Subsystem.

Ti-6Al-4V Titanium alloy (6% Aluminum, 4% Vanadium).

TLM Telemetry.

TMTC Tracking, Telemetry, and Telecommand.

TOF Time of Flight.

TRM Trajectory Correction Maneuver.

TT&C Telemetry, Tracking, and Command.

TTMTC Telemetry, Tracking, and Telecommand.

TWTA Travelling-Wave Tube Amplifier.

TX Transmitter/Transmitted.

UDSC Usuda Deep Space Center.

UL Uplink.

USC Uchinoura Space Center.

USO Ultra-Stable Oscillator.

UV Ultraviolet.

UVI Ultraviolet Imager.

VCO Venus Climate Orbiter.

VLBI Very Long Baseline Interferometry.

VOI Venus Orbit Insertion.

VTO Venus Transfer Orbit.

X-TRP X-band Digital Transponder.

List of Figures

List of Tables

Assignment #1 Change log	
Paragraph	*Description of the change applied*
§1.1	p. 2: section revised to improve clarity and accuracy.
§1.3	pp. 2–3: clarified the relationship between the mission drivers and the Scientific Objectives; Table 2 revised.
§2	p. 3: refined the functional analysis to improve clarity, consistency, and flow; Figure 1 revised.
§2.1	p. 4: added a paragraph to clarify the distinction between Mission and System requirements; Tables 3 and 4 added to improve the separation between requirements types.
§4.2	p. 5: added an introductory paragraph to provide context
§5	p. 6: added an introductory paragraph to clarify the relationship between Mission Phases and the ConOps; Figure 2 caption changed.
§5.2, §5.4	p. 7: expanded sections with introductory paragraphs to improve readability and flow.

1 Mission Overview & High-Level Goals

1.1 Mission Overview

Venus Climate Orbiter (VCO) **"AKATSUKI"** (PLANET-C) is Japan's first orbiter beyond Earth orbit, developed by Japan Aerospace Exploration Agency (JAXA)/Institute of Space and Astronautical Science (ISAS) and proposed in 2001. Launched on May 21st, 2010 aboard H-IIA LV from Tanegashima Space Center, it successfully entered Venus orbit on December 7th, 2015, and operated until April 2025 — 14 years of total lifetime against a nominal 2-year design life [1, 2, 3].

1.2 Needs, Goals, and Objectives (NGO)

Primary Scientific Objective (PSO): *Understand the mechanism responsible for the global atmospheric circulation of Venus, particularly the phenomenon known as atmospheric super-rotation.*
The Venusian atmosphere exhibits a strong zonal westward circulation whose wind speeds increase with altitude, reaching up to 100 m/s near the cloud tops (65–70 km). In contrast, the planet's rotation is extremely slow, with a period of 243 Earth days. Determining how momentum and energy are transported within this atmosphere is therefore the main scientific objective of the mission [2, 4].

ID	Scientific Objective	Description
SPSO-1	Observation of cloud dynamics and atmospheric circulation at different altitudes	Study of large-scale circulation patterns, wave activity, and atmospheric turbulence
SPSO-2	Characterization of the cloud layer structure	Interpretation of atmospheric dynamics and planetary energy balance
SSO-1	Lightning detection	Investigation of convective processes and electrical charge separation within the sulfuric acid cloud layer
SSO-2	Night airglow observation	Mapping spatial distribution and variability of airglow to study circulation patterns and wave propagation
SSO-3	Surface investigation	Measurement of surface emissivity, mineralogical variations, and possible volcanic thermal anomalies
SSO-4	Zodiacal light mapping	Observation of sunlight scattered by interplanetary dust in the inner Solar System

Table 1: Scientific Objectives [2, 4, 5]

1.3 Mission Drivers

Mission drivers identify the primary engineering constraints arising from the mission *Needs, Goals, and Objectives* (NGOs) and guide the main architectural choices. Their derivation from the scientific objectives is summarized below:

- **D-1 is derived from SPSO-1.** Investigating the atmospheric super-rotation requires accurate retrieval of global wind fields through long-duration tracking of cloud features. This requires quasi-synchronous motion with the upper cloud-level circulation near apoapsis for continuous monitoring. At the same time, the observation geometry must preserve close-range, high-resolution observations near periapsis to resolve fine-scale atmospheric structures.
- **D-2 is derived from SPSO-1/2.** Three-dimensional atmospheric characterization requires simultaneous observations of multiple altitude layers under the same illumination conditions. This drives the need for synchronized multi-wavelength observations, enabling reconstruction of the vertical atmospheric structure.
- **D-3 is derived from SPSO-2, SSO-1, and SSO-2.** Specifically, probing the mid/lower clouds (SPSO-2) requires a cryogenically cooled IR2 detector. This, combined with the intense solar flux in Venus orbit and the need to operate through eclipses to gather science data — lightning detection (SSO-1) and night airglow observation (SSO-2) — creates a primary engineering constraint on spacecraft thermal control and power availability.

ID	Driver Name	System Impact
D-1	Long-Duration Atmospheric Monitoring	Implemented through a highly elliptical near-equatorial orbit combining long-duration monitoring near apoapsis with high-resolution observations near periapsis. Drives MA, PS, TMTC, ADCS.
D-2	Simultaneous Multi-Layer Atmospheric Observation	Implemented through synchronized multi-wavelength observations across different atmospheric layers. Drives PL, EPS, TCS, OBDH.
D-3	Thermal–Power Constraints in Venus Orbit	Imposes IR2 cryogenic cooling together with continuous power availability under high solar flux and eclipse conditions. Drives MA, EPS, TCS, STR, CONF.

Table 2: Mission Drivers Summary [2, 3, 4, 5, 6]

The three drivers are complementary and collectively define the mission architecture. D-1 drives the observation geometry required to achieve the scientific objectives, D-2 drives the payload architecture needed to achieve the scientific objectives, while D-3 captures the environmental constraints that drive the spacecraft thermal-control and power subsystems [2, 3, 4, 5, 6].

2 Nominal Mission Functional Analysis

The mission functional architecture is organized around the high-level operational capabilities required to achieve the mission objectives. The primary role of the space segment is science acquisition, directly supporting the high-level goal of understanding Venusian atmospheric circulation. This core function is decomposed into major mission activities, including multi-wavelength atmospheric observations, lightning detection during eclipse, radio occultation experiments, and science data management. These science functions are supported by parallel operational functions including orbit maintenance, attitude and thermal control, and data handling and communications [2, 4]. The space segment also interacts with the ground segment for mission planning, command uplink, orbit determination, and science data reception. The resulting functional decomposition is shown in Fig. 1.

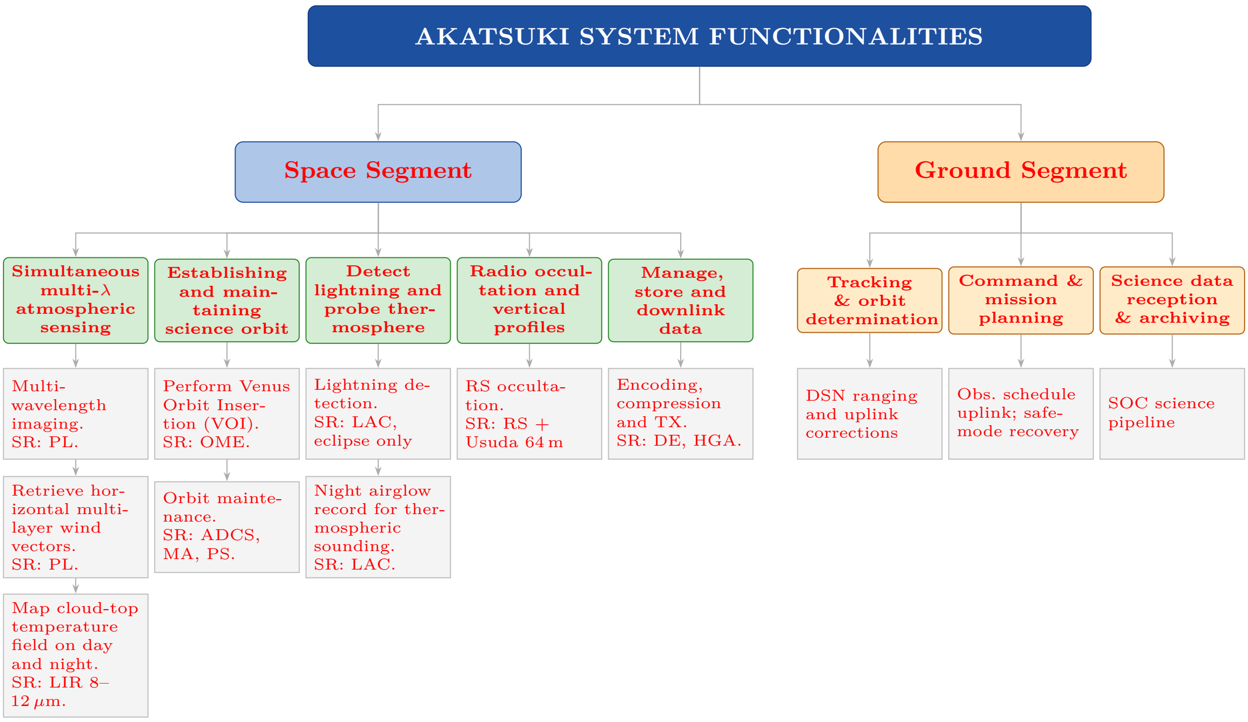

Figure 1: AKATSUKI Nominal Systems Functional Decomposition [2, 4]. Note: A sixth mission function, End-of-Life & Passivation, is not shown for clarity but is part of the nominal design – this includes propellant venting, battery discharge, and disposal maneuver planning. SR: System Resource.

2.1 Mission-Level & System-Level Requirements

Requirements are derived from the mission NGOs and the mission drivers identified in Sec. 1.3, and are structured according to ECSS-10-06C, which distinguishes *mission requirements* from *system requirements* within the Technical Requirements Specification [7]. Mission requirements define the scientific and operational capabilities that the mission shall achieve without prescribing a specific implementation, whereas system requirements specify the spacecraft performance needed to realize those capabilities. Each requirement is traced to the corresponding NGO(s) and mission driver(s), providing end-to-end traceability from mission objectives to system implementation.

Mission Requirement — The mission shall...	**Verification Method**	**Traced to (NGO → Driver)**	**Ref.**
characterize atmospheric circulation through repeated observations of cloud features.	Science data review; image correlation	SPSO-1 → D-1	[2, 4]
characterize the three-dimensional structure of the Venus atmosphere.	Science data review; multi-wavelength image analysis	SPSO-1, SPSO-2 → D-2	[2, 4]
support science observations during both sunlit and eclipse orbital phases.	Mission operations log; telemetry analysis	SPSO-2, SSO-1, SSO-2 → D-3	[2]

Table 3: Mission-level requirements (nominal design) [2, 4]

System Requirement — The spacecraft shall...	**Verification Method**	**Traced to (NGO → Driver)**	**Ref.**
be inserted into the nominal westward, highly elliptical, near-equatorial science Venus orbit.	Orbit determination via radiometric tracking post-VOI	SPSO-1 → D-1	[2]
maintain the nominal orbital geometry throughout the science mission.	Orbit determination analysis using radiometric tracking	SPSO-1 → D-1; SPSO-2, SSO-1, SSO-2 → D-3	[2]
maintain three-axis attitude stabilization during science observations to satisfy pointing requirements.	Star tracker / IMU telemetry; limb-fitting techniques	SPSO-1 → D-1; SPSO-1, SPSO-2 → D-2	[4]
maintain the operational temperatures of all spacecraft and payload units.	Thermal telemetry; in-flight cross-check	SPSO-2, SSO-1, SSO-2 → D-3	[5, 6]
provide continuous electrical power throughout the mission.	Power budget analysis; in-flight telemetry	SPSO-2, SSO-1, SSO-2 → D-3	[2]
achieve the downlink data rate required for each mission phase.	Link budget analysis; in-flight measurements	SPSO-1, SPSO-2 → D-2	[2]
provide onboard storage for science data between communication windows.	Memory diagnostics; data integrity verification	SPSO-1, SPSO-2 → D-2	[2]
comply with the launch vehicle mass constraint (launch mass $\leq$ 640 kg, including propellant).	Mass budget review; pre-launch weighing	SPSO-2, SSO-1, SSO-2 → D-3	[2, 8]

Table 4: System-level requirements (nominal design) [2, 4, 5, 6]

3 Trajectory Overview and Orbital Design Rationale

The nominal orbit is the direct engineering translation of Driver D-1. Selecting a westward near-equatorial elliptical orbit with apoapsis 78,500 km (13 Venus radii) and a 30-h period creates the 20-hour quasi-synchronization window between the spacecraft's apparent angular motion and the super-rotating atmosphere, enabling successive global images for cloud-tracking and wind field retrieval. The orbit is therefore the engineering solution adopted to satisfy Driver D-1 [2, 4].

4 Payload Analysis

The science payload (35 kg) consists of five photometric sensors, one radio science experiment, and the Digital Electronics (DE). The DE unit is critical: it translates observation programmes into hardware commands within the constraints of downlink capacity and available power [2, 4]. The PL was specifically designed to investigate the dynamics and vertical structure of the Venusian atmosphere through multi-wavelength observations. Probing different atmospheric altitudes and physical processes, the instruments enable a three-dimensional multi-wavelength characterization of atmospheric circulation [2, 4].

4.1 Instruments Overview

Instr.	Altitude Probed	Description
UVI	Cloud-top (65 km)	Dayside imaging of scattered solar radiation at 283 and 365 nm, sensitive to SO_2 and unknown UV absorber; mapping of absorber distribution to constrain composition and radiative properties of the upper clouds; cloud tracking from sequential images to derive horizontal wind fields.
LIR	Cloud top (65 km)	Continuous thermal imaging at 8–12 µm of cloud-top emission to retrieve temperature maps; inference of cloud-top altitude and vertical structure from temperature variations; detection of atmospheric waves and mesoscale dynamics from spatial and temporal variability.
IR1	Cloud layer (day); lower atm. + surface (night)	Dayside imaging at 0.90 µm for cloud tracking and wind retrieval; nightside observations at 0.90, 0.97, and 1.01 µm probing thermal emission from lower atm and surface, constraining surface emissivity, composition, and possible volcanic activity; H_2O abundance from differential absorption (0.97 vs 1.01 µm).
IR2	Mid/lower cloud (50–55 km); sub-cloud CO (35 km)	Nightside imaging at 1.7–2.3 µm probing thermal emission from the middle and lower cloud layers; retrieval of cloud opacity and structure to investigate cloud morphology and dynamics; cloud tracking to derive horizontal winds at multiple altitudes.
LAC	Lower thermosphere (90–120 km) and cloud layer.	Nightside detection of optical emissions from lightning (777.4 nm atomic oxygen line from electrical discharges) and airglow (557.7, 552.5 nm from upper atmospheric chemical reactions); mapping of airglow variability to investigate large-scale circulation and wave activity.
RS	Neutral atmosphere, ionosphere (32 km to >120 km)	Radio occultation at X-band (8.4 GHz) to derive vertical profiles of temperature, pressure, and electron density from the neutral atmosphere to the ionosphere; characterization of atmospheric structure and stability, including small-scale layering and wave activity; investigation of ionospheric variability and its interaction with solar radiation and solar wind.

Table 5: Payload Instrument Summary [2, 4, 5, 6]

4.2 Goal-to-Payload Correlation Matrix

The correlation matrix in Tab. 6 establishes the necessary instrument combinations required to achieve each scientific objective. However, to achieve these objectives, the payloads cannot operate continuously. Instead, their activation is strictly dictated by the mission's Conceptual Operations (ConOps), which structures observation modes around orbital and environmental constraints.

Scientific Objective (NGOs)	UVI	LIR	IR1	IR2	LAC	RS	DE
SPSO-1: Observation of cloud dynamics & atmospheric circulation	P	P	P	P	S	–	P
SPSO-2: Characterization of the cloud layer structure	P	P	S	P	–	S	S
SSO-1: Lightning detection	–	–	–	–	P	–	–
SSO-2: Night airglow observation	–	–	–	–	P	–	–
SSO-3: Surface investigation	–	–	P	S	–	–	S
SSO-4: Zodiacal light mapping	–	–	–	P	–	–	S

Table 6: Goal × Payload correlation matrix [2, 4, 5, 6]
Note: P = Primary, S = Secondary, – = Not active

5 Mission Phases – Gantt & Conceptual Operations (ConOps)

The mission timeline is divided into distinct chronological phases representing shifts in spacecraft priorities between navigation, survival, and scientific research. Five phases dictate spacecraft priorities, resource allocation, and risk postures, with recurring operational modes activating within Ph-4 at each orbital revolution. As illustrated in the nominal Gantt (Fig. 2), Ph-1 handles post-separation health checkout and ADCS initialization, establishing baseline attitude and communications [9]. Ph-2 focuses on heliocentric transfer; with most science payloads dormant, only IR1 executes secondary zodiacal-light observations, while TCMs refine Venus approach. Ph-3 is the most critical phase: an autonomous OME burn achieves a bound orbit, prioritizing all resources on maneuver monitoring to avert mission failure. Ph-4 initiates with commissioning before recurring science modes (see Sec.5.1) execute per orbit. Ph-5 spans operations past design life under depleted propellant margins, ending with passivation [10]. The ground segment operates continuously throughout all the phases [2, 4].

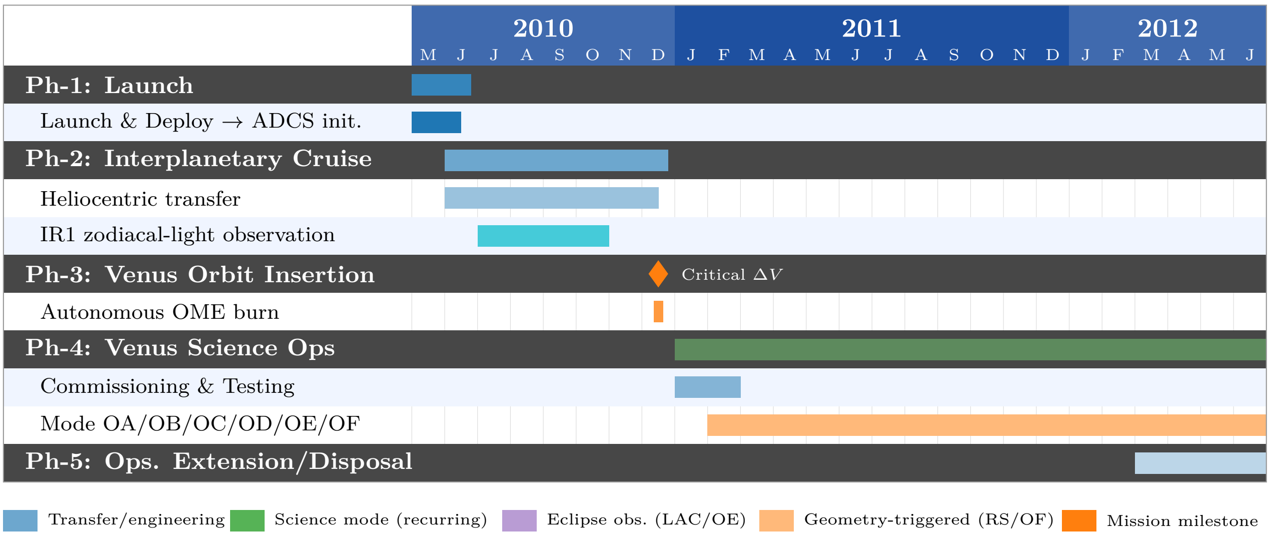

Figure 2: Nominal mission Gantt and ConOps (phases, orbit modes, active functions, ground segment operations) [2, 4]. Monthly resolution, May 2010 – Dec 2012. Nominal 2-year science design life counted from VOI (Dec 2010). Time starts at spacecraft separation from H-IIA LV, May 21st 2010.

5.1 Operational Observation Modes

ID	Mode	Geometry	Payload	Science Product	Geometry & ConOps Logic
OA	Global Imaging	Near apoapsis	IR1,IR2, UVI, LIR + DE	Synoptic cloud maps; long-term variability of cloud morphology and wind fields.	Venus disk fits in camera FoV. DE automates multi-camera sequences every $\sim$ 2h. Primary science mode enables D-1 quasi-sync cloud tracking.
OB	Close-Up Imaging	Towards periapsis	IR1,IR2, UVI, LIR	Mesoscale cloud evolution; high-res surface features; stereo cloud-top mapping.	S/C within 10,000 km from Venus. Resolution 0.2–6 km/px for near-IR cameras. Sacrifices planetary coverage for mesoscale dynamical detail.
OC	Limb Imaging	Dayside near periapsis	UVI, IR1, LIR	Aerosol vertical profile up to 100 km altitude; haze stratification.	Planetary limb in FoV. Vertical resolution: $\sim$ 0.7 km (UVI, IR1), $\sim$ 3 km (LIR) from 1,000 km altitude.
OD	Zonal Scan	Around periapsis (1–2 h, 300 km)	IR1, IR2, UVI, LIR	Quasi-1D zonal strips along orbital track; intermediate spatial scale.	Image intervals <10 min. Complementing apoapsis disk images. 0.2–6 km/px near-IR images @ 1000–8000 km.
OE	Eclipse Observations	Umbra passage (at each orbit)	LAC (primary only)	Lightning flash detection; O_2 airglow maps; thermospheric waves.	Illumination-constrained. Eclipse duration $\leq$ 90 min actively managed (Driver D-3).

Continued on next page

Table 7 – continued from previous page

ID	Mode Name	Orbital Position	Active Payload	Science Product	Geometry Trigger / ConOps Logic
OF	Radio Occultation	Spacecraft occulted by Venus from Usuda (JP)	RS/USO + Usuda 64 m DSN	Vertical temperature, H_2SO_4 density, and ionospheric electron density profiles.	Camera images same region before/after occultation — near-simultaneous correlation of vertical profiles with cloud morphology.

Table 7: Operational Observation Modes (recurring per orbital revolution) [2, 4]

5.2 Instrument × Operational Mode Matrix

The specific allocation of payload instruments across the various observation modes is summarized in Tab. 8, reflecting the operational constraints established by the ConOps.

Instrument	Cruise	OA	OB	OC	OD	OE	OF
UVI	–	P	P	P	P	–	–
LIR	–	P	P	P	P	–	–
IR1	–	P	P	P	P	–	–
IR2	S	P	P	–	P	–	–
LAC	–	–	–	–	–	P	–
RS / USO	–	–	–	–	–	–	P
DE (coordination)	S	P	P	P	P	–	–

Table 8: Instrument × Operational Mode matrix [2, 4, 5]
Note 1: P = Primary, S = Secondary, – = Not active
Note 2: Cryogenic cooling not activated during cruise to conserve power budget.

5.3 Phases × ConOps Matrix

Tab. 9 synthesizes the chronological mission phases with their corresponding ConOps logic, illustrating how operational priorities shift throughout the mission lifetime.

Mission Phase	ConOps Logic
Ph-2 – Interp. Cruise	Secondary science during heliocentric transfer. Passive DE data ops.
Ph-3 – Venus Orbit Insertion (VOI)	All resources devoted to OME monitoring. Autonomously executed.
Ph-4 – OA Mode	Global images every 2 h. DE automates multi-camera sequences.
Ph-4 – OB/OC/OD Mode	Proximity exploited for resolution. OB: sustained observation of restricted region. OC: attitude shifted for limb geometry (vertical aerosol sounding). OD: nadir strips along track; intermediate spatial scale.
Ph-4 – OE Mode	Illumination geometry changes operational priority: LAC uniquely allocated; all other instruments suspended. Battery must sustain full eclipse.
Ph-4 – OF Mode	LOS geometry exploited: equatorial orbit enables low-latitude atmospheric probing. Camera images before/after occultation → near-simultaneous correlation between vertical profiles and cloud morphology.

Table 9: ConOps, Phases and Functionalities: integrated summary (nominal design) [2, 4]

6 Mission Trajectory Design

6.1 Functionalities and Phases

The AKATSUKI interplanetary trajectory was designed as a direct transfer, consistent with the 0.5-revolution option selected by JAXA for the 2010 launch window [11], and a nominal Time of Flight (TOF) of 201 days. The interplanetary arc supports several functionalities that drive the ΔV budget:

1. **Trajectory Injection**: the H-IIA launcher inserts AKATSUKI onto the Venus Transfer Orbit (VTO), with a characteristic energy $C_3 = 18.46\,\text{km}^2/\text{s}^2$, within the launcher's capability [11].
2. **Cruise Corrections**: a set of trajectory correction manoeuvres (TRM-1, -2, -3) is performed to refine the Venus B-plane targeting conditions and compensate for injection errors. [11].
3. **VOI**: a sequence of three periapsis burns reduces the hyperbolic arrival trajectory into the final science orbit through progressive apoapsis reduction, complemented by small apoapsis maneuvers (APV) to refine the periapsis altitude [12].
4. **Station Keeping**: the station-keeping strategy is driven by the need to preserve the orbital conditions required for the scientific objectives, rather than maintaining a fixed set of Keplerian elements. The only critical constraint is the periapsis altitude, which must remain above 300 km for safety reasons. The orbit is inherently robust to long-term perturbations over the 2-year nominal science phase, and therefore only occasional corrective maneuvers may be required. [11]

6.2 Budget Breakdown per Maneuver

Interplanetary Transfer The launcher provides the ΔV to reach the VTO, no spacecraft ΔV is associated with this stage; further details are reported in App. A and Tab. 11.

VOI Sequence The Venus Orbit Insertion (VOI) sequence is modelled as three impulsive burns at periapsis. The periapsis radius is assumed constant at $r_p = R_{\text{Venus}} + 550\,\text{km}$ throughout all three burns, consistent with the JAXA targeting strategy [11, 12]. The vis-viva equation is used to compute the velocity at periapsis for each intermediate orbit, and the ΔV is obtained as the difference between successive periapsis velocities corresponding to apoapsis reduction. [13].

Station Keeping The station-keeping analysis accounts for the main perturbations listed as follows:

- Venus's oblateness induces secular drifts in the right ascension of the ascending node and argument of periapsis [13, 14], that over the two-year mission amount to $\Delta\Omega = -0.5°$ and $\Delta\omega = +1.0°$.
- The SRP acceleration at Venus is modelled with the solar radiation pressure at 0.71 AU, reflectivity $C_r = 1.5$, and area-to-mass ratio $A/m = 0.00631\,\text{m}^2/\text{kg}$ [12]. According to [13], these data lead to $a_{\text{SRP}} = 8.25 \times 10^{-11}\,\text{km/s}^2$.
- At 300 km, the Venusian atmospheric density is $\approx 10^{-14}\,\text{kg/m}^3$ [15]. According to [13, 12], the resulting semi-major axis decay over 2 years is $\Delta a_{\text{drag}} \approx 0.1\,\text{km}$, leading to $\Delta V_{\text{drag}} \sim 10^{-6}\,\text{m/s}$. No aerobraking was planned since the drag values obtained from this simulation.
- 3BP due to the Sun [13, 16] induces $\Delta\Omega_{\odot} = 6.6 \times 10^{-6}$ deg and $\Delta\omega_{\odot} = -1.3 \times 10^{-5}$ deg over 2 years — approximately 5×10^4 times smaller than J_2.
- Venus has no intrinsic global magnetic dipole [17, 18]. An upper bound for the acceleration on a hypothetical dipole moment $m_{\text{dip}} = 1\,\text{A}\cdot\text{m}^2$ gives $a_{\text{mag}} \sim 10^{-14}\,\text{km/s}^2 \ll \Delta a_{\text{drag}}$.

7 Budget Reconstruction

The Trajectory Correction Maneuver (TRM) and Apoapsis/Periapsis Velocity Adjustment Maneuver (APV) correction values were not independently computed, but estimated from Venus Express mission data [19], which provides a representative baseline for interplanetary cruise and approach corrections, given the similarity of both missions in interplanetary trajectory type and Venus approach geometry. Although the two missions operate in different orbits, the adopted values are consistent with the sum of maneuver magnitudes reported for Akatsuki (excluding backup maneuvers) by Ryne et al. [12].

For station keeping, no AKATSUKI-specific pre-launch budget was found in the available literature. The closest comparable mission, Venus Express, reports ∼17 m/s per year [19], but this value is not directly applicable due to differences in orbital altitude, area-to-mass ratio, and operational strategy. The computed $\Delta V_{\mathrm{SK}} = 5.21$ m/s is therefore retained as a conservative upper bound.

Interplanetary Trajectory			
Maneuver	**Computed** [m/s]	**From Literature** [m/s]	**Notes**
TRM-1	–	2.97	Correction maneuver [11]
(TRM-1c)	–	0.1	Correction not needed [12]
TRM-2	–	0.26	Approach correction [11]
(TRM-2c)	–	0.1	Correction not needed [12]
TRM-3	–	0.04	Final executed correction [11]
VOI-1	711.96	704.6	Hyperbola → ellipse capture [12]
(VOI-1c)	–	10.0	Post-insertion correction [12]
APV-1	–	56.1	Small periapsis correction [12]
APV-1 B/U	–	56.1	Backup maneuver [12]
VOI-2	99.38	99.4	Apoapsis reduction [12]
(APV-2)	–	1.0	Small periapsis correction [12]
VOI-3	94.76	100.1	Final orbit shaping (30 h orbit) [12]
TRM+APV	40	–	Estimated value [19]
Station Keeping (Disturbances)			
SK-J_2	0.0000	–	J_2-induced precession (drift accepted) [13]
SK-SRP	5.2069	–	Solar radiation pressure (dominant) [13]
SK-DRAG	0.0006	–	Atmospheric drag (order-of-magnitude) [13]
SK-3BP	0.0003	–	Solar third-body (negligible) [13, 16]
SK-MAG	0.0000	–	Magnetic effects (negligible) [13]
SUM	5.2078	–	Explained in the text
ESA ΔV Margins			
Det. Margin	47.57	–	MAR-DV-010 (5% · ΔV|| 10 m/s) [20]
LD	30.00	–	MAR-DV-080 [20]
Nav/App	10.00	–	MAR-DV-100 [20]
TOTAL	**1038.87**	**1030.57**	Including SK + ESA margins

Table 10: ΔV Budget Reconstruction

Step	**Adopted model**	**Reference**
Trajectory design	Genetic Algorithm (GA) + Sequential Quadratic Programming (SQP)	[13]
Interplanetary transfer	Multi-rev. Lambert problem, patched conics method; ephemeris from JPL Horizons DE441 vector tables, Ecliptic J2000, one day resolution.	[13]
Venus Orbit Insertion (VOI)	Vis viva at fixed periapsis: $v_p = \sqrt{\mu_V(2/r_p - 1/a)}$; $\Delta V = \lvert v_{p,k-1} - v_{p,k}\rvert$ for three successive apoapsis reductions (96 h → 48 h → 30 h)	[13]
Station Keeping	Disturbance models for SRP, magnetic torques, atmospheric drag, 3BP (Sun) and J_2 (according to Kozai) effects; upper bound for SRP computed as: $\Delta V_{\mathrm{SK}} = a_{\mathrm{SRP}} \cdot T_{\mathrm{mission}}$	[13, 12]
Margins	MAR-DV-010/080/100 from ESA CFD margin philosophy	[20]

Table 11: Synthetic Mathematical Flow and Adopted Models

A Appendix A – Nominal Trajectory and Optimized Transfer

A further mission analysis performed by the team is presented below, to gain a more in-depth understanding of the mission. This section contains additional efforts undertaken to independently validate the methodology and results, ensuring a higher level of mission analysis robustness.

The Lambert problem was solved using (JPL Horizons DE441 ephemerides (Ecliptic J2000, heliocentric) with a patched-conic approximation. The departure date and TOF were optimised with a Genetic Algorithm (GA) followed by Sequential Quadratic Programming (SQP) refinement, confirming the nominal 20 May 2010 departure as near-optimal for the 2010 launch window.

The interplanetary transfer was optimized through a multi-step algorithm that progressively narrows the search window: first, a global GA over June 2009–June 2011 (TOF between 60 and 310 days); then, a zoomed GA over April–July 2010 (TOF 80–260 days); and finally, a SQP refinement within ±5 days in departure date and ±10 days in TOF around the best solution from the zoomed GA.

LAUNCH VEHICLE		
Parameter	Value	Notes
Selected	H-IIA 202	[8]
$C_3{}^{max}$	30 km^2/s^2	[8]
NOMINAL TRAJECTORY (20 May 2010, TOF = 201 days)		
Parameter	Value	Notes
V_∞ Earth	$<$ 4.3 km/s	[11]
C_3	18.4572 km^2/s^2	H-IIA limit: ∼18.5 [11]
V_∞ Venus	3.3368 km/s	design constraint: $<$ 3.4 [11]
TARGET ORBIT		
Parameter	Value	Notes
H_p	550 km	[11]
H_a	80000 km	[11]
i	172 deg	[11]
T	30.534 h	[11]

OPTIMISED TRANSFER	
Parameter	Value
Departure	10 Jun 2010
TOF	185.5 days
$\Delta V_{Lambert}$	7.0101 km/s
C_3	15.9838 km^2/s^2
V_∞ Venus	3.0121 km/s

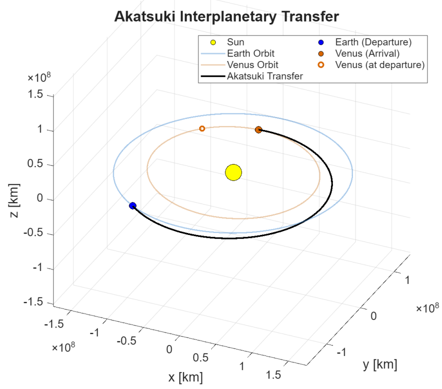

Figure 3: Mission parameters: on the left, the launch vehicle, the nominal trajectory and the target orbit; on the right, the parameters for the automated transfer and the 3D trajectory.

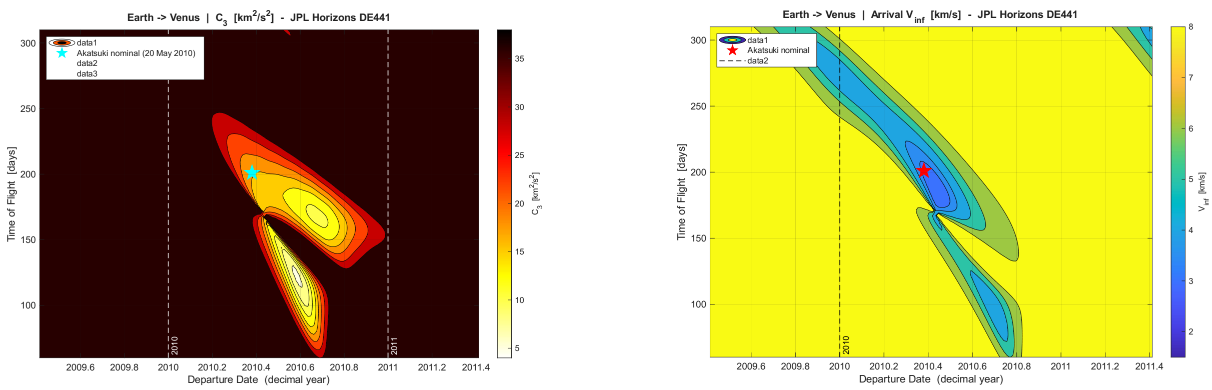

Figure 4: From left to right: C_3 and V_∞ porkchop plots for Earth departure and Venus arrival.

2 Mission Propulsion Architecture

The propulsion subsystem of the spacecraft is based on a chemical propulsion architecture, consisting of a bipropellant **Orbital Maneuvering Engine (OME)** and a monopropellant **Reaction Control System (RCS)**, allowing for efficient impulsive maneuvers throughout the mission.

2.1 Orbital Maneuvering Engine (OME)

The OME uses Hydrazine (N_2H_4) as fuel and Mixed Oxides of Nitrogen (97% Nitrogen Tetroxide, 3% Nitric Oxide) (MON-3) as oxidizer, which are hypergolic. The bipropellant configuration allows for restart capability and precise control of the burn duration. The system is pressure-fed, using an inert gas (Helium) to drive propellant flow, which simplifies the design and improves robustness at the expense of performance compared to pump-fed systems.

2.2 Reaction Control System (RCS)

The RCS is a monopropellant propulsion system based on the catalytic decomposition of hydrazine. This dual-level configuration allows both larger attitude adjustments and fine pointing accuracy. The system consists of 12 thrusters (more details in Tab. 16).

The thrusters are arranged in two independent groups of 6, providing redundancy and operational flexibility. This configuration ensures operational robustness in case of partial system failure. Unlike the main engine, the RCS provides pulsed thrust due to the system's ON/OFF valve-based operation.

2.3 Propulsion Subsystem & Roles Functional Allocation

The OME and RCS selection is driven by the requirements of the several mission phases. The most demanding maneuver in terms of ΔV is the Venus Orbit Insertion (VOI), which must be performed near periapsis - where spacecraft velocity is the highest - to maximize burn effectiveness in reducing orbital energy. A bipropellant system provides higher thrust and specific impulse than monopropellant alternatives, minimizing gravity losses and achieving the required ΔV at lower propellant mass, which is critical given VOI's dominant contribution to the overall ΔV budget. In contrast, the remaining operations - trajectory correction maneuvers (TCMs), orbit trimming after capture (APV), station-keeping, and attitude control - require smaller ΔV with high precision and controllability, for which a monopropellant system is preferable due to its simplicity, reliability, and suitability for pulsed operation. This leads to a clear functional separation between the two propulsion systems:

- The OME is used for large, energy-dominant maneuvers such as orbit insertion;
- The RCS is used for small trajectory corrections and attitude control.

At the same time, the two systems are functionally coupled. The RCS ensures proper spacecraft orientation during OME burns, enabling accurate thrust vector alignment and improving overall maneuver performance. In contingency scenarios, the RCS can also provide limited orbital maneuver capability, albeit at significantly lower efficiency. [3]

Overall, this propulsion architecture represents an optimal trade-off between efficiency, reliability, and controllability, and is consistent with standard design practices for interplanetary missions requiring both large impulsive maneuvers and precise long-term orbit management.

Phase	**Thruster**	ΔV [m/s]
Ph-1: Launch	LV	0
Ph-2: Interplanetary Cruise (TRM)	RCS	40
Ph-3: Venus Orbit Insertion (VOI + APV)	OME	906.1
Ph-4: Venus Science Ops (SK)	RCS	5.2076

Table 12: Spacecraft Propulsion Subsystem ΔV Allocation by Phase and Thruster, margins excluded.

3 Propulsion Subsystem Reverse Sizing

3.1 Propellant Selection

The OME uses anhydrous N_2H_4 as fuel and MON-3 as oxidizer. For the OME combustion chamber, a ceramic material (Si_3N_4) is chosen. This is a world-first, enabling higher combustion temperatures than metallic chambers, improving combustion efficiency and reducing cooling requirements. [3]

The RCS operates with monopropellant N_2H_4, catalytically decomposed over a ruthenium catalyst bed, and has $I_{sp} = 220\,\mathrm{s}$. The N_2H_4 supply is shared between the OME fuel line and the RCS feed branches via independent valve-controlled paths. This dual-mode arrangement eliminates a dedicated RCS propellant tank, reducing structural mass and plumbing complexity. [21]

Parameter	OME (Primary)	RCS (Secondary)
Propellant type	Bipropellant	Monopropellant
Fuel	N_2H_4 (hydrazine)	N_2H_4 (hydrazine)
oxidizer	MON-3 (NTO + 3 % NO)	—
Mixture ratio (O/F)	1.65	—
I_{sp}, vacuum	300 s	220 s
Thrust level	500 N	23 N (coarse) / 3 N (fine)

Table 13: Propellant selection summary.

Quantity (Symbol)	Value	Unit
Total propellant volume (V_{prop})	133.17	L
He tank volume (V_{He})	9.512	L
He mass (nominal) (m_{He})	0.4689	kg
He mass (+10 % margin) ($m_{\mathrm{He,\,marg}}$)	0.5158	kg
He tank diameter (d_{He})	262.9	mm
Wall thickness (Ti-6Al-4V) (t)	3.03	mm
Tank structural mass (m_{tank})	2.917	kg
Max He flow rate (VOI burn) ($\dot{m}_{\mathrm{He}}$)	0.6531	g/s

Table 14: Pressurant sizing results.

3.2 Tanks

Three tanks are required: one **N_2H_4 tank** (shared between OME and RCS), one **MON-3 tank** (OME oxidizer), and one **He pressurant tank**.

Material and shape All tanks are sized in **Ti-6Al-4V**, the standard material for storable-propellant pressure vessels on interplanetary missions due to its high strength-to-density ratio ($\sigma_y \approx 827\,\mathrm{MPa}$, $\rho = 4430\,\mathrm{kg/m^3}$) and compatibility with both hydrazine and nitrogen tetroxide compounds [21, 22]. A **spherical** geometry is adopted for all three tanks: the sphere minimises the surface-to-volume ratio, hence structural mass, for a given internal pressure and volume, and eliminates bending stresses [23].

Sizing method Wall thickness is determined from the thin-wall hoop stress criterion [23]:

$$t = \frac{P\,r}{2\,\sigma_{\mathrm{des}}} \tag{1}$$

$\sigma_{\mathrm{des}} = 827\,\mathrm{MPa}$ for propellant tanks (at feed pressure $P_{\mathrm{feed}} = 2.0\,\mathrm{MPa}$) and $\sigma_{\mathrm{des}} = 650\,\mathrm{MPa}$ for the He tank (at storage pressure $P_1 = 30.0\,\mathrm{MPa}$). A 5 % ullage volume is added to the propellant volume before sizing the tank radius [21]. Structural mass follows from the thin-shell volume: $m_{\mathrm{tank}} = \rho_{\mathrm{Ti}} \cdot 4\pi r^2 t$. [23] The propellant volumes are computed from the propellant properties (see Tab. 15).

Results					
Tank	**Propellant [kg]**	**Volume [L]**	**Inner ⌀ [mm]**	**Wall t [mm]**	**Struct. mass [kg]**
N_2H_4 (shared)	73.4	73.07 (+5 %)	527.2	0.32	1.233
MON-3	87.1	60.10 (+5 %)	494.0	0.30	1.014
He pressurant	0.4689 (+ 10% margin)	9.512	262.9	3.03	2.917
Notes: $\rho_{N_2H_4} = 1004\,\mathrm{kg/m^3}$,$\rho_{\mathrm{MON\text{-}3}} = 1450\,\mathrm{kg/m^3}$ [22]					

Table 15: Propellant and Pressurant Tank Sizing Results [20]

The N_2H_4 and MON-3 tank diameters are consistent with the spacecraft bus dimensions ($1.5 \times 1.4 \times 1.0$ m [12]), with both tanks fitting within the central bus volume.

3.3 Pressurant

Gaseous helium (GHe) is selected as pressurant for both the N_2H_4 and MON-3 tanks. Its low molecular weight ($M = 4.003$ g/mol) minimises pressurant mass for a given pressurised volume while its chemical inertness ensures full compatibility with both propellants.

The He tank is sized under an isothermal, pressure-regulated model. Helium stored at initial pressure $P_1 = 30$ MPa is regulated to a constant feed pressure $P_{\text{feed}} = 2.0$ MPa at the propellant tanks. Mass conservation under isothermal expansion gives the required He volume:

$$V_{\text{He}} = \frac{P_{\text{feed}} \cdot V_{\text{prop}}}{P_1 - P_{\text{feed}}}$$

where $V_{\text{prop}} = m_{\text{MON-3}}/\rho_{\text{MON-3}} + m_{N_2H_4}/\rho_{N_2H_4} = 87.1/1450 + 73.4/1004 = 133.2$ L. The required He mass follows from the ideal gas law, with $R_{\text{He}} = 2077$ J/(kg K) and $T = 293$ K. A 10 % mass margin is applied, yielding $m_{\text{He}} = 0.516$ kg [23]. The wall thickness is determined from the thin-wall hoop-stress criterion (Eq. 1), with $\sigma_{\text{des}} = 650$ MPa. Sizing results are presented in Tab. 14.

3.4 Feeding Strategy

During the VOI burn, constant feed pressure maintains a stable $O/F = 1.65$ and hence constant I_{sp} throughout the maneuver. A blow-down architecture is therefore precluded for the OME: in a blow-down system, ullage pressure decays as propellant is expelled, causing progressive O/F drift and I_{sp} degradation over the burn. [21]

A single GHe supply, regulated from $P_1 = 30$ MPa to $P_{\text{feed}} = 2.0$ MPa through dual redundant pressure regulators pressurizes both the N_2H_4 and MON-3 tanks independently. The RCS feed branches tap from the same regulated helium supply at the same set point, eliminating a dedicated secondary pressurant circuit and reducing system mass and complexity. [21, 3]

3.5 Thrusters Quantity and Configuration

Depending on mission requirements, the number of thrust units is planned. Thrusters shall [21, 24]:

- be able to generate long (> 10 s) steady-state burns for velocity control maneuvers, if needed;
- fire in short pulses of < 10 s each to control attitude and manage momentum;
- provide three-axis control, which requires a minimum of 6 attitude control thrusters.

In the design process, equal emphasis shall be put on both operating life and performance.

Component	Thrust & Configuration	Primary Roles
OME	1 × 500 N; aligned through CoM to minimize parasitic torque during long burn	Large orbit translational maneuvers
RCS	8 × 23 N (pitch/yaw maneuvers); 4 × 3 N (roll maneuvers)	23-N th.: handle reorientation and momentum unloading including the respin of RW; 3-N th.: fine corrections incompatible with RW.

Table 16: AKATSUKI Thrusters Configuration [22, 21].

As evidenced by the AKATSUKI architecture, RCS thrusters are clustered at vehicle extremities to maximize lever arms relative to the CoM, optimizing coupled rotational-translational control. The OME is isolated on the $-z$ plane, opposite to the HGA ($+z$) and perpendicular to the SAPs ($\pm y$), to eliminate plume impingement and molecular contamination on sensitive surfaces. This arrangement ensures effective control moments while shielding critical hardware from exhaust particulates. [2]

3.6 Propulsion System Schematics Analysis

The AKATSUKI propulsion schematics details the He pressure-fed chain for N_2H_4 and MON-3 and distinguishes between the bipropellant main engine and RCS clusters, reflecting a design that balances high-performance maneuvering with robust control via integrated regulators and valves. [3]

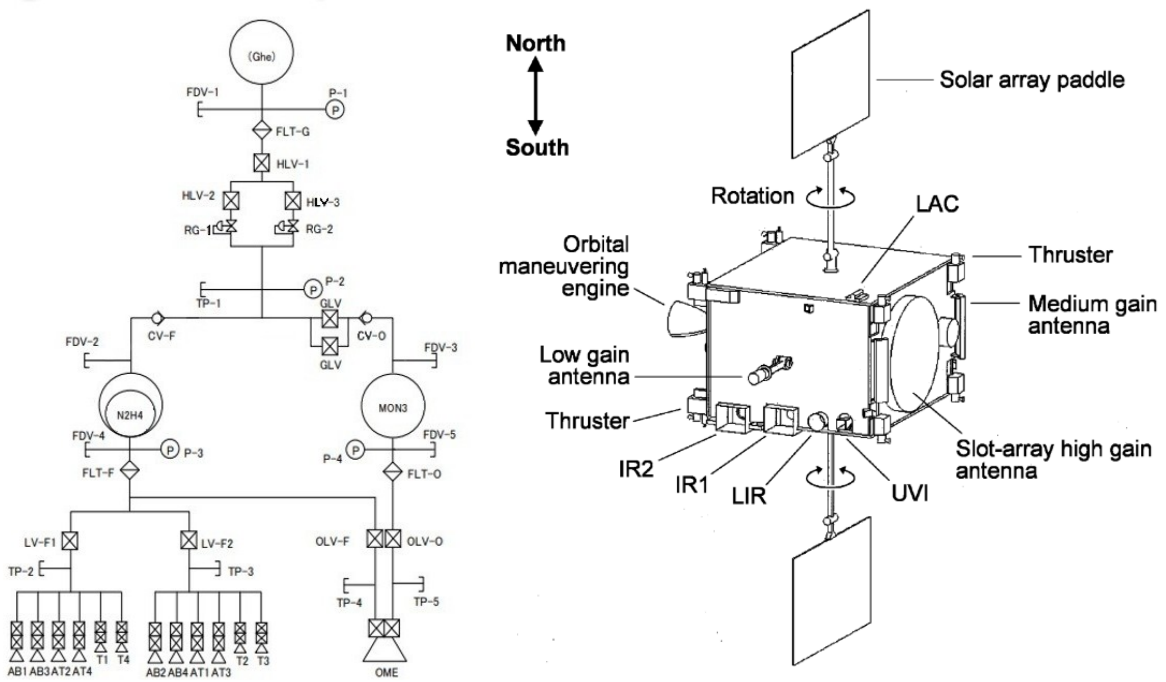

Figure 5: AKATSUKI Propulsion Subsystem Architecture & Position of RCS and OME [3, 25].

Component	Function and placement
Pressure transducers P-1–P-4	Monitor He tank, regulated line, N_2H_4 tank, MON-3 tank
Fill/drain valves FDV-1–FDV-5	Ground filling, draining, venting
Filters FLT-G/F/O	Downstream of particulate sources; upstream of regulators and thrusters
Hand latch valves HLV-1–HLV-3	Safety isolation barriers in propellant lines
Pressure regulators RG-1, RG-2	Dual-redundant He regulation from 30 MPa to 2.0 MPa
Check valves CV-F, CV-O	One-way flow; prevent backflow into He line
Latch valves LV-F1, LV-F2, OLV-F/O	Branch isolation; enable fault containment

Table 17: Key propulsion line components [26].

The tanks and propulsive lines configuration reflects a trade-off among mass constraints, geometric integration, attitude control, and bus compactness. The heaviest propulsive volumes and main lines are positioned as far inboard as possible, close to the CoM, since the allowable CoM offset constrains tank number and placement — minimizing CoM shifts during depletion and limiting distribution network length. The He tank is placed upstream in the pressurization circuit, while propellant tanks are arranged to support OME thrust. Concentrating all tanks in the central bus region, with short and hierarchically organized lines, maximizes both spatial occupancy and dynamic stability. Key line components (Tab. 6) follow standard practice: filters upstream of sensitive components, check valves between the He line and propellant tanks, and fill/drain valves accessible in the launch configuration.

3.7 Propulsion Subsystem Mass Budget

Tab. 18 summarises the propulsion subsystem dry and wet mass. Tank structural masses are computed values (§3.2). Thruster masses are taken from performance data for this thrust class in the available literature [21, 22]. Plumbing (lines, valves, regulators, transducers) is estimated at 15 % of tank dry mass, consistent with standard parametric allowances for pressure-fed storable-propellant systems [21].

Item	Mass [kg]	Note
	Dry mass	
He pressurant tank (Ti-6Al-4V, spherical)	2.917	«computed»
N_2H_4 tank (Ti-6Al-4V, spherical)	1.233	«computed»
MON-3 tank (Ti-6Al-4V, spherical)	1.014	«computed»
OME (500 N biprop., Si_3N_4 chamber)	3.0	«from literature» [22]
RCS (8×23 N + 4×3 N hydrazine)	4.0	«from literature» [21]
Plumbing, valves, lines (15 % of tank mass)	0.77	«estimated» [21]
PS dry mass	**12.93**	«computed»
	Pressurant	
GHe (+10 % margin)	0.52	«computed»
	Propellant	
MON-3 (OME oxidizer)	87.1	«computed»
N_2H_4 (shared OME + RCS)	73.4	«computed»
Total propellant	160.5	«computed»
Total propellant	196.7	«from literature» [12]
PS wet mass	**173.95**	«computed»
PS wet mass	**210.15**	«literature»

Table 18: Propulsion subsystem mass budget

3.8 Propulsion Subsystem Power Budget

The propulsion subsystem consumes electrical power primarily for catalyst bed preheating, pressure transducer excitation and OME valve/line preconditioning before the VOI burn [21, 4, 22]. Catalyst bed heater power per thruster class is taken from literature performance data; OME feeding line heating power is accordingly estimated [21]. Tab. 19 lists the propulsion power budget per mission mode.

Consumer	Unit power [W]	Active units	Mode
23 N bed heaters	10	4 (of 8)	Cruise (nominal)
3 N bed heaters	4	2 (of 4)	Cruise (nominal)
Pressure transducers	0.5	4	All modes
Cruise (nominal)		**50 W**	
23 N bed heaters	10	8 (all)	Pre-VOI / VOI
3 N bed heaters	4	4 (all)	Pre-VOI / VOI
OME preconditioning	20	1	Pre-VOI only
Pressure transducers	0.5	4	Pre-VOI / VOI
Pre-VOI / VOI (worst case)		**118 W**	
23 N bed heaters	10	2	Station keeping
Pressure transducers	0.5	4	Station keeping
Station keeping		**22 W**	

Table 19: Estimated propulsion subsystem power budget per mission mode [21, 22]

4 TMTC Architecture Overview

4.1 Architecture Selection and Rationale

AKATSUKI adopts a direct-link X-band architecture, with no relay satellites, compliant with Consultative Committee for Space Data Systems (CCSDS) standards and International Telecommunication Union (ITU) deep-space frequency allocations (7145–7235 MHz uplink, 8400–8500 MHz downlink) [27, 28]. The architecture is driven by four mission-level constraints:

- **Interplanetary deep-space mission**: X-band mandatory per ITU; no LEO relay applicable.
- **Venus–Earth distance 0.3–1.7 AU**: weak signal requires large ground antenna (Usuda Deep Space Center (UDSC) 64 m) and high-gain on-board Radio Frequency (RF) chain.
- **Multi-phase mission with autonomous VOI**: spacecraft must be self-sufficient during the critical burn; multiple antenna types are required to cover all attitude configurations.
- **Radio Science (RS)/Ultra-Stable Oscillator (USO) experiment**: ultra-stable one-way X-band downlink drives inclusion of the USO.

Space segment. The RF chain comprises: two redundant X-band digital transponders (X-TRP), one TWTA (primary), two SSPA (cruise and backup), one USO [29], two HGAs, two MGAs , and two LGAs [27].

Ground segment. Primary station: UDSC, Usuda, Japan [27]. Backup stations: Uchinoura Space Center (USC) 34 m and NASA's DSN (Goldstone, Madrid, Canberra) [4]. The DSN is used primarily during critical phases (launch, VOI) for global coverage continuity. ESA infrastructure supports additional Very Long Baseline Interferometry (VLBI)/Delta-DOR orbit determination [4].

Functional logic. The subsystem is structured around three operational levels, each trading link performance against robustness to attitude loss:

- **Nominal science (Ph-4/5)**: HGA + TWTA, three-axis stabilised, $+Z$ Earth-pointing. Maximum downlink up to 32 kbps.
- **Degraded/safe mode**: MGA (gimballed, $\pm Z$ coverage) or LGA. Reduced rates (32 bps MGA; 15.625 bps LGA minimum in Venus orbit).
- **Contingency**: LGA omnidirectional coverage (4π sr combined) guarantees command uplink at any attitude, including spin-stabilised safe mode.

The antennas are connected to transponders and amplifiers through a redundant RF switch matrix, enabling dynamic routing and fault containment. All critical components (X-TRP, SSPA, HGA, MGA, LGA) are present in dual redundant chains.

5 Operational Phases and TMTC Modes

Phase	Dist. [AU]	Antenna	Amp.	Primary function
Ph-1: Launch & Deploy	$0 \rightarrow 0.003$	LGA ($\pm X$)	SSPA 10 W	Checkout, ADCS init
Ph-2: Cruise (early)	$0.003 \rightarrow 0.3$	LGA→MGA→HGA	SSPA 10 W	TRM, HK & TT&C
Ph-2: Cruise (late)	$0.3 \rightarrow 0.6$	HGA	SSPA 10 W	TRM, science cruise
Ph-3: VOI (nominal)	~ 0.6	HGA pre/post; LGA contingency	SSPA 10 W	Post-burn confirm †
Ph-4: Science (OA to OD)	$0.3 \rightarrow 1.7$	HGA	TWTA 20 W	Science downlink
Ph-4: OE Eclipse	$0.3 \rightarrow 1.7$	HGA	TWTA 20 W	LAC data downlink
Ph-4: OF Radio Occultation	$0.3 \rightarrow 1.7$	HGA (USO-driven)	TWTA 20 W	RS downlink
Ph-5: Extension	$0.3 \rightarrow 1.7$	HGA	TWTA 20 W	As Ph-4

† Pre-VOI, the HGA is used for the final state uplink from UDSC. During the burn the LGA provides contingency command reception with no real-time ground control. Post-VOI, the HGA re-establishes the nominal link [27].

Table 20: Spacecraft operational phases and TMTC assets [27, 4].

6 Frequency Band Selection and Datarate

6.1 Frequency Band Justification

Two parameters govern the X-band selection:

$$\underbrace{L_{\text{space}} = 20\log_{10}\left(\frac{\lambda}{4\pi d}\right)}_{\text{free-space path loss}}, \qquad \underbrace{G_{\text{Tx}} = 10\log_{10}\left(\eta_{\text{Tx}}\left(\frac{\pi D_{\text{Tx}}}{\lambda}\right)^2\right)}_{\text{transmit antenna gain}} \tag{2}$$

Although L_{space} increases with frequency, G_{Tx} for a fixed aperture increases as $1/\lambda^2$, yielding a net link-budget advantage at higher frequencies. X-band therefore outperforms S-band: for the same physical aperture, the gain advantage ($\sim$11 dB) compensates the higher free-space loss, and additionally provides lower ionospheric noise and wider available bandwidth for higher datarates [21]. The selected frequencies are: uplink $f_{\text{UL}} = 7.15$ GHz, downlink $f_{\text{DL}} = 8.41$ GHz, coherent turnaround ratio 880:749, uplink bandwidth 2.0 MHz, downlink bandwidth 3.4 MHz [27].

6.2 Datarates by Phase and Antenna

Mode	Direction	Antenna	Datarate
TLM HGA nominal	DL	HGA	32 kbps at 0.7 AU; 16 kbps at 1.1 AU; 8 kbps at 1.5 AU
TLM MGA emergency	DL	MGA	32 bps
TLM LGA safe mode	DL	LGA	Not available (LGA is CMD-only)
CMD HGA	UL	HGA	1 kbps (constant, full mission)
CMD LGA (cruise)	UL	LGA	0.2–2 kbps (distance-dependent)
CMD LGA (minimum)	UL	LGA	15.625 bps (Venus orbit, worst case)

Table 21: Datarate by antenna and mode [27, 30].

7 Signal Manipulation: Encoding and Modulation

7.1 Encoding

AKATSUKI uses CCSDS concatenated coding with interleaving depth 2, a standard in deep space [27]:

- **Outer code** (RS): R_{RS}= 223/255 = 0.875, error correction capability $t = 16$ symbols [31].
- **Inner code** (convolutional): $R_{\text{C}} = 1/2$, constraint length $K = 7$, Viterbi decoding [31].

The combined concatenated code rate is $R_{c,\text{tot}} = R_{\text{RS}} \times R_c = 0.437$, yielding a coding gain of approximately 5.5 dB at BER $= 10^{-7}$ versus uncoded Binary Phase Shift Keying (BPSK) [21]. Target Bit Error Rate (BER): 10^{-7} downlink (TLM); 10^{-5} uplink (CMD) [31]. The downlink uses a tighter BER target (10^{-7}) because science telemetry requires high data integrity for image reconstruction; the uplink is less critical (10^{-5}) since commands are short, repeated, and verified by acknowledgement.

7.2 Modulation

Downlink and uplink: BPSK with residual carrier (PM), $m = 1$ bit/symbol [27, 31]. Residual carrier enables ranging and Doppler tracking simultaneously with data. Bit-error probability: $P_{e,\text{BPSK}} = \frac{1}{2}\,\text{erfc}(\sqrt{E_b/N_0})$ [21]. Symbol rate at maximum downlink $R_{\text{net}} = 32$ kbps:

$$R_s = \frac{R_{\text{net}}}{R_{c,\text{tot}} \cdot m} = \frac{32 \times 10^3}{0.437 \times 1} = 73.2 \text{ ksps} \tag{3}$$

Occupied bandwidth (roll-off $\alpha = 0.5$ [21]):

$$B = R_s(1+\alpha) = 73.2 \times 1.5 = 109.8 \text{ kHz} \ \ll\ 3.4 \text{ MHz (allocated)} \tag{4}$$

8 Transceiver and Amplifier Selection

8.1 X-TRP

- Type: in-house JAXA Field-Programmable Gate Array (FPGA)-based digital transponder [27]
- Quantity: 2 (cold redundancy, cross-strapped) [27]
- Key feature: regenerative ranging — 12 dB improvement over conventional ranging [27]. Doppler aiding and synchronous integration performed to recover weak signals directly in the FPGA [27].
- USO reference: 38.22567759 MHz, Allan deviation $< 10^{-12}$ at 1–1000 s integration [29]

8.2 Power Amplifier Trade-off and Selection

The amplifier selection was driven by two constraints [27, 30]:

- **Link requirement**: >8 kbps at 1.5 AU and 32 kbps at 0.7 AU [30]
- **Power limit**: total power budget 700 W; nominal TMTC power 93.2 W (TWTA active) [27, 30]

Unit	P_{out}	Phase	Rationale
TWTA (primary)	20 W = 13 dBW	Ph-4/5	Higher efficiency; 3 dB advantage over each SSPA; activated after 1-month post-launch
SSPA-A	10 W = 10 dBW	Ph-1/2/3; TWTA backup	Lower thermal load; suitable for cooler cruise phase, lower-rate links and early operations
SSPA-B	10 W = 10 dBW	Cold standby	Full chain redundancy

Table 22: Power amplifier selection and rationale [27, 30, 32]

The TWTA is selected as primary because it provides double the power efficiency of each SSPA, operating within the thermal envelope in Venus orbit. The SSPAs are retained as secondary units for phases where their lower thermal load is preferred and as backup to the TWTA [27, 32]. Typical PAE for X-band TWTAs of this class is 40–55%, versus 25–35% for SSPAs [21], confirming the TWTA efficiency advantage at the 20 W output level required to close the link at 1.7 AU.

9 Antenna Sizing, Configuration and Positioning

The antenna subsystem adopts a three-level hierarchy to guarantee continuous communication under varying attitudes and mission phases. Each level trades link performance for pointing robustness.

High-Gain Antenna (HGA). This is a flat slot-array antenna on quartz-honeycomb plate, copper-film etched slots [27]. Two separate dishes are required because the slot-array bandwidth cannot span both RX and TX simultaneously [27]. Both HGAs are mounted on the $+Z$ Earth-pointing panel, opposite to the OME to eliminate plume impingement [27]. Pointing losses are negligible for both HGAs, which confirms that the ADCS pointing accuracy of $\pm 0.1°$ [4] is adequate.

MGA and LGA. Also here the chosen geometry eliminates any interactions between OME and sensitive components. See Tab. 24 for further details.

Parameter	HGA-TX (DL)	HGA-RX (UL)	Reference
Frequency	8.41 GHz	7.15 GHz	[27]
Diameter D	0.92 m	0.34 m	[27]
Gain (from literature)	35.5 dBi	21.4 dBi	[27]
Gain (computed with $G = \eta(\pi D/\lambda)^2$)	35.6 dBi	22.9 dBi	[21]
Discrepancy	0.1 dB	1.5 dB (due to radome losses)	[27]
Efficiency η	0.55	0.30	[21]
Beamwidth $\theta_{3\text{dB}} = 70\lambda/D$	2.72°	8.64°	[21]
Pointing loss $L_{\text{mis}} = -12(e/\theta)^2$, $e = 0.1°$	−0.02 dB	≈0 dB	[4, 21]
Bandwidth	3.4 MHz	2.0 MHz	[27]

Table 23: HGA parameters and sizing verification [27].

Parameter	MGA-A / MGA-B	LGA-A / LGA-B
Type	Horn	Lens (polyimide CEPLA dielectric lens on horn)
Quantity	2, mounted on $+Y$ panel	2: LGA-A on $+X$, LGA-B on $-X$
Coverage	MGA-A: $+Z$ hemisphere; MGA-B: $-Z$ hemisphere	Combined coverage: full 4π sr; gain > -5 dBi at any attitude
Gain	~13 dBi [21]	$>$ 0 dBi at 60° from boresight; -4.9 dBi UL / -6.9 dBi DL at 90°
Pointing	1-axis gimbal	Omnidirectional; no pointing constraint
Height above body	—	340 mm (to avoid structural interference)
Link direction	Both UL and DL	CMD UL only (Venus orbit)
Min datarate	32 bps (emergency TLM)	15.625 bps (worst case, Venus orbit)
Usage	Emergency TLM, safe-mode backup for HGA, VOI transition	Ph-1 checkout, contingency CMD uplink at any attitude, safe-mode recovery

Table 24: MGA and LGA parameters, usage and gain [27, 21].

10 Subsystem Architecture

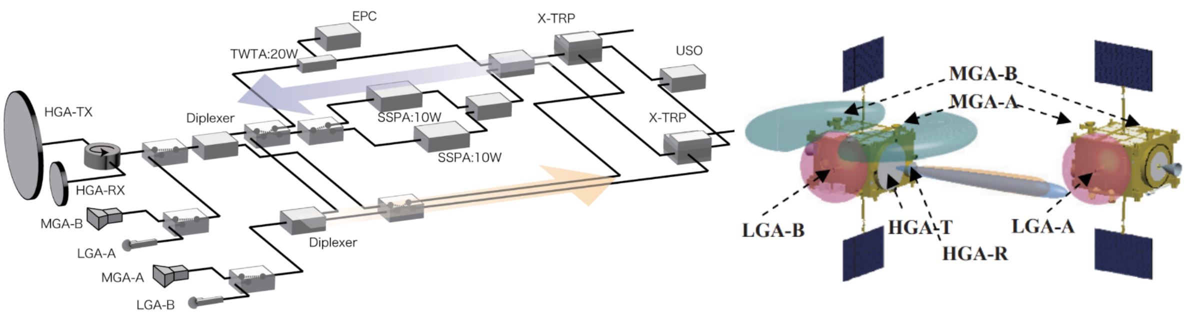

Figure 6: AKATSUKI telecommunication subsystem and its schematic antenna coverage.

11 Ground Station Selection

The UDSC was selected as primary because its aperture provides the gain required to close the downlink at 1.7 AU. Japan geographic visibility limits contacts to 6–7 h/day; the DSN global distribution ensures spacecraft visibility maintained during launch and VOI regardless of Earth rotation [4].

Station(s)	Diameter	G_{RX} @ 8.41 GHz	T_{sys}	Additional notes
UDSC	64 m	72.5 dBi; $G/T = 52.7$ dB/K	96 K	Primary. T_{sys} with 5 mm/h rain, 15°
USC	34 m	66.9 dBi	—	Backup; main station for first 3 months
DSN	34/70 m	$G/T \approx 47$ dB/K	—	Backup; launch and VOI coverage
ESA	—	—	—	VLBI/Delta-DOR support

Table 25: Ground station parameters [27, 4, 33, 34]. DSN & ESA values depending on the specific plant.

UDSC uplink transmit gain (7.15 GHz) and USC receive gain (8.41 GHz) with $\eta = 0.55$ yields [21]:

$$G_{\mathrm{UDSC,TX}} = 0.55\left(\frac{\pi \times 64}{0.04196}\right)^2 = 0.55 \times (4786)^2 = 1.26 \times 10^7 = 71.0 \text{ dBi} \tag{5}$$

$$G_{\mathrm{USC,RX}} = 0.55\left(\frac{\pi \times 34}{0.03564}\right)^2 = 0.55 \times (2997)^2 = 4.94 \times 10^6 = 66.9 \text{ dBi} \tag{6}$$

12 Contact Strategy

Contact window duration. During nominal Phase-4, the spacecraft is in contact with UDSC for 6–7 h per day [4, 2]. This is set by UDSC geographic visibility and the orbit: near apoapsis, the HGA maintains Earth-pointing for 8 h/orbit; UDSC elevation > 5° leads to a conservative $T_{\text{contact}} = 6$ h/orbit estimate. During the remaining non-visibility, science data are stored onboard in the DE's 512 Mb SSD [2]. During solar conjunction blackouts (~20 days/conj.) the spacecraft is autonomous.

Data volume per contact. Downlink rate varies with Earth–Venus distance [27, 30]:

- **Best Case (0.3 AU):** 32 kbps → 691.2 Mbit (≈ 86.4 MB) per 6 h contact.
- **Nominal Case (0.85 AU):** 16 kbps → 345.6 Mbit (≈ 43.2 MB) per 6 h contact.
- **Worst Case (1.7 AU):** 8 kbps → 172.8 Mbit (≈ 21.6 MB) per 6 h contact.

Mitigation strategy. The DE unit reduces transmitted data volume before downlink: JPEG2000 lossless compression during favourable links; lossy compression, pixel binning, data slicing, and partial cancellation during low-rate periods, with observation intervals extended to 4+ h [2].

13 Science Data Budget

Instrument	Mode	Rate/image	Active/orbit	Raw/orbit
UVI	OA (2 h cadence)	5 Mbit	2 h	60 Mbit
LIR	OA continuous	0.5 Mbit	10 h	50 Mbit
IR1	OA + OB	10 Mbit	3 h	120 Mbit
IR2	OA + OB (nightside)	10 Mbit	3 h	120 Mbit
LAC	OE eclipse (≤90 min)	5 Mbit/pass	1.5 h	5 Mbit
DE housekeeping	All modes	0.1 kbps	30 h	10.8 Mbit
Total raw/orbit				**≈365.8 Mbit**

Table 26: Estimated payload data generation per Ph-4 orbital period. Per-instrument volumes assumed according to available literature [2, 4]; compression factor from [21].

After onboard compression (by a factor of 3 [21]), $V_{\text{compressed}}$/orbit ≈ 365.8/3 + 10.8 = 132.7 Mbit. The required average downlink rate to complete one orbit dump in one 6 h contact window is therefore $R_{\text{req}} = (132.7 \times 10^6)/(6 \times 3600) = 6.15$ kbps, which is within the allowed 4–32 kbps range. Even at worst-case (1.7 AU), the orbit's data volume is transferred in the 6-h window with margin. This is robust to ±50% variations in the assumed data volumes.

14 Link Budget

Equations and Parameters. The link budget follows the standard expression for E_b/N_0 [21]:

$$\left.\frac{E_b}{N_0}\right|_{\text{dB}} = \underbrace{P_{\text{tx}} + L_l + G_{\text{tx}}}_{\text{EIRP}} + L_s + L_a + L_{\text{mis}} + G_{\text{rx}} - k - 10\log_{10}(T_s) - 10\log_{10}(R) \tag{7}$$

where $k = -228.6$ dBW/K/Hz (Boltzmann), T_s is the specific system noise temperature considered, and R is the datarate. The free-space path loss for the downlink and the uplink is (with r in AU):

$$L_s^{\text{DL}}(r_{\text{AU}}) = -275.4 - 20\log_{10}(r_{\text{AU}})\ \text{[dB]}, \quad f = 8.41\ \text{GHz} \tag{8}$$

$$L_s^{\text{UL}}(r_{\text{AU}}) = -272.0 - 20\log_{10}(r_{\text{AU}})\ \text{[dB]}, \quad f = 7.15\ \text{GHz} \tag{9}$$

Required $E_b/N_{0_{\text{req}}} = E_b/N_{0_{\text{min}}} + 3$ dB [21]:

- $E_b/N_{0_{\text{min,DL}}} = 5$ dB at BER $= 10^{-7}$ (concatenated CCSDS code) [21] ⇒ $E_b/N_{0_{\text{req,DL}}} = 8$ dB
- $E_b/N_{0_{\text{min,UL}}} = 4.5$ dB at BER $= 10^{-5}$ [21] ⇒ $E_b/N_{0_{\text{req,UL}}} = 7.5$ dB

Parameter	Value	Type	Parameter	Value	Type	Parameter	Value	Type
$G_{\text{HGA-TX}}$	35.5 dBi	[27]	P_{SSPA}	10.0 dBW	[27]	$T_{\text{sys, spacecraft}}$	500 K = 27.0 dBK	[21]
$G_{\text{HGA-RX}}$	21.4 dBi	[27]	k	−228.6 dBW/K/Hz	[27]	$P_{\text{UDSC,TX}}$	43.0 dBW	[21]
G_{LGA}	−5 dBi (worst)	[27]	$G_{\text{UDSC,RX}}$	72.5 dBi	[33]	L_l (S/C TX)	−1.0 dB	[21]
G_{MGA}	13 dBi	[21]	$G_{\text{UDSC,TX}}$	71.0 dBi	[21]	L_a (X-band, 15°)	−0.3 dB	[21]
P_{TWTA}	13.0 dBW	[27]	$T_{\text{sys,UDSC}}$	96 K = 19.8 dBK	[33]			

Table 27: Common link budget parameters.

Downlink Budget (HGA-TX, TWTA → UDSC). The EIRP for downlink, TWTA, can be computed as $\text{EIRP}_{\text{DL}} = 13.0 + (-1.0) + 35.5 = 47.5\,\text{dBW}$. Collecting constant terms in Eq. (7) with UDSC parameters ($G_{\text{UDSC,RX}} = 72.5\,\text{dBi}$, $T_{\text{sys}} = 96\,\text{K}$):

$$\left.\frac{E_b}{N_0}\right|_{\text{DL}} = 53.0 - 20\log_{10}(r_{\text{AU}}) - 10\log_{10}(R) \tag{10}$$

Case	r [AU]	R [bps]	$20\log r$	$10\log R$	E_b/N_0 [dB]	Margin [dB]
Ph-1 (SSPA 10 W)	0.003	1 000	−50.5	30.0	70.5	+62.5
Ph-2 late / Ph-3 pre-VOI	0.60	32 000	−4.4	45.1	12.3	+4.3
Ph-3 post-VOI (CMD)	0.60	1 000	−4.4	30.0	27.4	+19.4
Ph-4 best (0.3 AU)	0.30	32 000	−10.5	45.1	18.4	+10.4
Ph-4 nominal	0.85	32 000	−1.4	45.1	9.3	+1.3
Ph-4 nominal	0.85	16 000	−1.4	42.0	12.4	+4.4
Ph-4 worst (1.7 AU)	1.70	32 000	+4.6	45.1	3.3	-4.7
Ph-4 worst (1.7 AU)	1.70	8 000	+4.6	39.1	9.3	+1.3
Ph-4 worst (1.7 AU)	1.70	4 000	+4.6	36.0	12.4	+4.4

Table 28: Downlink budget. All E_b/N_0 values computed via Eq. (10). $(E_b/N_0)_{\text{req}} = 8\,\text{dB}$.

At 1.7 AU, 32 kbps does not give a positive margin. Reducing to 8 kbps yields +1.3 dB, consistent with [30]. Since the downlink is data-rate limited, it is the primary driver of the TMTC sizing, and:

- Nominal Ph-4, 0.85 AU, 32 kbps, $B = 109.8\,\text{kHz} \implies \text{SNR} = 9.3 + 45.1 - 50.4 = 4.0\,\text{dB}$.
- Worst-case Ph-4, 1.7 AU, 4 kbps, $B = 13.7\,\text{kHz} \implies \text{SNR} = 12.4 + 36.0 - 41.4 = 7.0\,\text{dB}$.

Uplink Budget (UDSC → HGA-RX) and LGA Contingency. Collecting constants with spacecraft receiver parameters ($G_{\text{HGA-RX}} = 21.4\,\text{dBi}$, $T_{\text{sys, spacecraft}} = 500\,\text{K}$):

$$\left.\frac{E_b}{N_0}\right|_{\text{UL}} = 64.2 - 20\log_{10}(r_{\text{AU}}) - 10\log_{10}(R_{\text{UL}}) \tag{11}$$

Since public sources do not provide the UDSC uplink EIRP or the exact onboard receiver noise figure, the uplink is verified using regenerative ranging test data [32]: the uplink C/N_0 was measured at 13 dB better than the downlink C/N_0, giving $(C/N_0)_{\text{UL}} \approx 47.86 + 13 = 60.86\,\text{dBHz}$ at 1.5 AU [32, 33].

Case	r [AU]	R [bps]	$20\log r$	$10\log R$	E_b/N_0 [dB]	Margin [dB]
Ph-4 best	0.30	1 000	−10.5	30.0	44.7	+37.2
Ph-4 nom.	0.85	1 000	−1.4	30.0	35.6	+28.1
Ph-4 worst	1.70	1 000	+4.6	30.0	29.6	+22.1
Ph-4 worst, LGA	1.70	15.625	+4.6	11.9	20.2	+12.7

Table 29: Uplink budget (UDSC 64 m → HGA-RX). $(E_b/N_0)_{\text{req}} = 7.5\,\text{dB}$. All values computed [21].

The uplink closes with large margin (>22 dB via HGA) at all distances. Even the worst-case LGA contingency at 1.7 AU ($G_{\text{LGA}} = -5\,\text{dBi}$) closes at +12.7 dB, so it does not drive the TMTC sizing.

Assignment # 4 Change log	
Paragraph	*Description of the change applied*
§15, §16	pp. 23–24: selected paragraphs revised for clarity and accuracy; 7 changed; citations added to Tables 30 and 31
§17	pp. 24–25: gravity-gradient torque re-derived from the maximum principal-inertia difference $\lvert I_x - I_y \rvert$, rather than the (vanishing) $\lvert I_z - I_x \rvert$; disturbance budget and dominant-term discussion updated accordingly.
§17.3, §17.4	pp. 25: supporting citations added to the paragraphs.
§18, §19	pp. 25–27: sensor and actuator suite re-identified against the AOCS hardware list of [35]; masses, power, torque and momentum figures replaced with the corresponding supplier data where reported, and with a justified commercial-equivalent assumption otherwise; Table 32 values of assumptions revised.
§19.1	pp. 26–27: slew torque and time reverse-sized from the selected wheel's real torque limit instead of an assumed reorientation time; tetrahedral envelope sized on its minimum (worst-axis), not maximum, projection.
§19.2	p. 27: desaturation-pulse attitude perturbation extended to include the post-firing coasting/braking phase, and the pulse duration re-derived so that the resulting excursion stays within the mission's own pointing budgets.
§20.2	p. 28: desaturation pulse duration and re-acquisition timing updated for consistency with the above; Table 33 minor text changes.
§21	pp. 28–29: mass and power budgets rebuilt bottom-up from the identified hardware, with explicit margins; consistency checks updated to the new figures; Tables 34, 35 revised to contain updated ADCS subsystem mass breakdown and fix formatting
§21.1	p. 29: minor revisions to the text; Table 36 values revised for CSS.

15 AOCS Architecture and Design Rationale

AKATSUKI is a three-axis stabilised Venus orbiter whose Attitude and Orbit Control Subsystem (AOCS) provides attitude determination and control while supporting orbit-control maneuvers throughout all mission phases [4, 35]. The functional chain encompasses attitude and orbit sensors, estimation, guidance and control algorithms, and actuators, all coordinated by the Attitude and Orbit Control Unit (AOCU) which translates computed torque commands into drive signals via the Driving Unit (DRV) [35, 36].

Architecture selection. A three-axis, bias-momentum configuration was selected, combining RWs for fine continuous control with a RCS for large maneuvers and momentum unloading. The rationale is driven by mission-level constraints [2, 35]:

- **Pointing accuracy:** the science payload requires Absolute Performance Error (APE) $\leq 0.05°$, attainable only with RW-based fine control.
- **Multiple pointing targets:** the HGA must point toward Earth while scientific targets are observed, demanding continuous re-targeting incompatible with spin stabilization.
- **Slew agility:** large-angle reorientations (up to 90°) must be executed during the science orbit; thrusters provide the torque authority required for the largest of these.
- **Power:** the deployed Solar Array Paddle (SAP) requires Sun-pointing to maximize power generation, making three-axis stabilization the preferred architecture.

The RW+RCS hybrid solution balances pointing precision, control authority, and propellant consumption across the full mission lifetime, as summarised in Tab. 30 and Fig. 7.

Category	Component	Primary function
Sensors	Star Trackers (STTs) (×2)	High-accuracy absolute attitude
	Coarse Sun Sensors (CSSs) (×5)	Approximate Sun-vector acquisition
	Fine Sun Sensors (FSSs) (×2)	Precise Sun-vector acquisition
	Inertial Reference Units (IRUs) (×3)	Continuous angular-rate integration
	Accelerometer (ACM) (×1)	ΔV measurement during burns
	Sun Presence Sensors (SPSs) (×2)	Binary Sun presence for safe mode
Actuators	Reaction Wheels (RWs) (×4)	Fine three-axis attitude control
	RCS thrusters (×12)	Slew maneuvres and desaturation
Processing	Attitude and Orbit Control Unit (AOCU)	Estimation, guidance and control
	Driving Unit (DRV)	From AOCU to hardware drive signals

Table 30: AOCS hardware components [4, 35].

On-board processing and control modes. The AOCU executes three sequential functions: (i) *Navigation*: combines IRU-propagated attitude with periodic STT absolute updates to produce a continuous attitude state estimate; (ii) *Guidance*: selects the target reference frame (target-of-interest-pointing for science, Earth-pointing for communication, Sun-pointing for safe mode); (iii) *Control*: computes torque commands via a three-axis Proportional-Derivative (PD) regulator and routes them through the DRV to the RWs and the RCS thrusters. Mode transitions are primarily ground-commanded or timeline-driven (for critical maneuvers, like VOI); an autonomous Fault Detection, Isolation, and Recovery (FDIR) overrides the nominal control logic and forces Sun-pointing safe mode upon anomaly detection (loss of STT lock, power drop, or communication blackout) [35, 36].

16 Pointing Budget per Control Mode

The pointing requirements are derived from each subsystem's operational needs following the methodology of [21, 37]. Tab. 31 synthesizes the APE/AKE budgets per control mode. Key drivers are:

- **Science (all modes [4]):** cloud tracking with UVI/IR1 at apoapsis requires resolving ~50 km cloud features, giving an angular resolution ≈ 0.036°; APE budget is set at ≤ 0.05° (3σ) [35].
- **Telecom (HGA-TX):** The HGA's beamwidth ($\theta_{3\text{dB}}$) limits the allowable pointing error to ≤ 0.5°dB, corresponding to a pointing loss < 0.1 dB.
- **Power (SAP tracking):** body attitude set within ≤ 5° maintains a positive power margin in safe hold; the SAP gimbal provides $\pm Y$-axis fine tracking independently of the main body [35].
- **Propulsion (VOI-related):** thrust-vector misalignment generates a lateral ΔV error; ≤ 0.5° APE at ignition bounds the lateral component below 0.9% of the nominal burn magnitude.

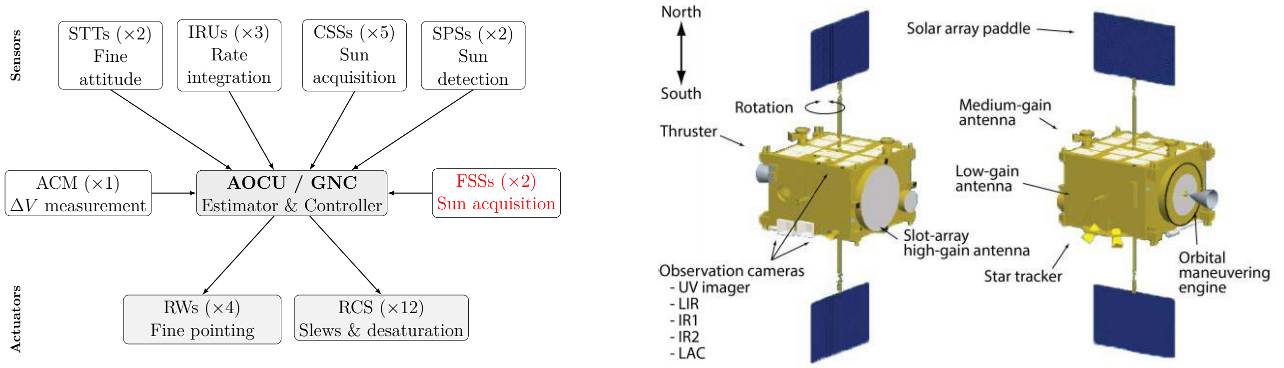

Figure 7: Functional AOCS architecture (left) and external configuration of the spacecraft [38] (right).

Control Mode	**APE** [°]	**AKE** [°]	**Driver**	**Ref.**
Safe Hold (Sun acquisition)	≤ 5	≤ 2	Accuracy from [39]	
Interplanetary Cruise	≤ 0.5	≤ 0.1	HGA Earth pointing	[4]
VOI (pre/post burn)	≤ 0.5	≤ 0.1	Thrust-vector alignment	[35]
Science (OA–OF)	≤ 0.05	≤ 0.01	Cloud-tracking pixel resolution	[35]
Eclipse (OE)	≤ 0.5	≤ 0.5	Power hold (payload off)	[36]

Table 31: Pointing budget per control mode (3σ, temporal interpretation) [21, 35].

The science AKE is readily achievable. The selected STT provides an absolute attitude accuracy of ≈ 6 arcsec (3σ, Sec. 18), while IRU propagation over the maximum update interval (~1 min) contributes only 0.7 arcsec. Combining these independent error sources using the root-sum-square (RSS) method yields an overall attitude knowledge error of ≈ 6 arcsec, well below the allocated 36 arcsec budget [21].

17 Spacecraft Moments of Inertia and Disturbance Torques

The principal moments of inertia are estimated since [21], so that $I_{\text{base}} \approx 0.01\, M^{5/3}$, which applied to the dry mass $M = 321$ kg [12] and corrected for the asymmetric contribution of the two SAPs (assumed 15 kg each with span 0.9 m from bus CoM):

$$\Delta I_x = \Delta I_z \approx 2 \times 15 \times 0.9^2 = 24.3\ \text{kg m}^2 \qquad \textbf{[computed]} \qquad (12)$$

$$I_{\text{base}} = 0.01 \times 321^{5/3} \approx 150.5\ \text{kg m}^2$$

$$I_x \approx 175\ \text{kg m}^2, \quad I_y \approx 151\ \text{kg m}^2, \quad I_z \approx 175\ \text{kg m}^2 \qquad \textbf{[computed]} \qquad (13)$$

The worst-case (maximum) inertia $I_v = 175$ kg m^2 is used conservatively for all actuator sizing.

17.1 Gravity Gradient Torque

The maximum gravity-gradient torque depends on the largest principal-moment difference [21]:

$$(T_{\text{GG}})_{\max} = \frac{3\,\mu_{\text{Venus}}}{2\,(R_{\text{Venus}} + H_p)^3}\,|I_{\max} - I_{\min}|\sin(2\theta)$$

The bus and SAPs are symmetric about the $\pm Y$ axis, so $I_x = I_z$ by construction. The largest difference between the principal moments of inertia is $|I_{\max} - I_{\min}| = |I_x - I_y| = |175 - 151| = 24$ kg m^2, which yields $(T_{\mathrm{GG}})_{\max} \approx 4.1 \times 10^{-5}$ N m at the nominal periapsis of the science-orbit ($H_p = 550$ km, $i = 172°$, Sec. 5) and for the worst-case attitude offset $\theta = 45°$ from the local vertical.

17.2 Solar Radiation Pressure (SRP) Torque

The SRP acceleration was established in the station-keeping analysis, using $F_s = 2649$ W/m^2 at Venus (0.71 AU), reflectivity $C_r = 1.5$, and area-to-mass ratio $A/m = 6.31 \times 10^{-3}$ m^2/kg, so that $a_{\mathrm{SRP}} = 8.25 \times 10^{-11}$ km/s^2. The corresponding disturbance force on the spacecraft and torque (assuming lever arm $\ell \approx 0.5$ m from CoM to SRP center) are:

$$F_{\mathrm{SRP}} = a_{\mathrm{SRP}} \cdot M = 2.65 \times 10^{-5}\ \mathrm{N} \implies T_{\mathrm{SRP}} = F_{\mathrm{SRP}} \times \ell = 1.33 \times 10^{-5}\ \mathrm{N\,m} \quad \textbf{[computed]}$$

17.3 Three-Body Gravity Gradient Torque

During science operations, the gravitational field of the Sun pulls the bus, too. In the Circular Restricted Three-Body Problem (CR3BP), the gravity gradient torque from the Sun can be estimated via the standard single-body formula, using $\mu_\odot$ and the mean Sun–spacecraft distance at Venus orbit $R_\odot = 1.08 \times 10^{11}$ m [40, 41, 42]. The worst-case magnitude (assuming a principal axis misalignment $\theta = 45°$ and using the maximum moment difference $|I_{\max} - I_{\min}| = |I_x - I_y| = 24$ kg m^2) is:

$$(T_{\mathrm{GG},\odot})_{\max} = \frac{3\mu_\odot}{2R_\odot^3} |I_{\max} - I_{\min}| \sin(2\theta) \approx 3.8 \times 10^{-12}\ \mathrm{N\,m} \ll T_{\mathrm{GG}} \qquad \textbf{[computed]}$$

The GG from the Sun is therefore irrelevant for ADCS sizing and control design for AKATSUKI.

17.4 Aerodynamic and Magnetic Torques

At 550 km altitude, Venusian atmospheric density $\rho \approx 10^{-14}$ kg/m^3, giving $T_{\mathrm{DRAG}} < 10^{-8}$ N m, negligible [15]. Venus has no global magnetic dipole, therefore T_{MAG} is negligible too [18].

17.5 Total Disturbance Torque

It is the sum of the torques from the previous sections, and is used for the actuator sizing in Sec. 19.

$$T_d = T_{\mathrm{GG}} + T_{\mathrm{SRP}} + T_{\mathrm{DRAG}} + T_{\mathrm{MAG}} + T_{\mathrm{GG},\odot} \approx 5.5 \times 10^{-5}\ \mathrm{N\,m} \qquad \textbf{[computed]}$$

T_{GG} is therefore the dominant disturbance torque (≈75% of T_d, about 3× larger than T_{SRP}).

18 Sensor Selection, Sizing and Redundancy

The AOCS sensor suite is identified directly from the component architecture reported in [35], which provides the supplier, type and heritage of each flight unit. Where power values are not legibly reported in that source, a value from the manufacturer's published data for the same product line is used and flagged as such. Tab. 32 lists type, accuracy, power and redundancy rationale.

Selection rationale per mode [21]:

- **Science:** dual STT voting → AKE ≤ 0.01°; IRU propagates attitude between STT updates.
- **Cruise and VOI:** single STT + IRU → 0.1° AKE; keeping the second STT in cold standby reduces power consumption.
- **Safe hold:** CSS + SPS ensure Sun acquisition from any attitude without STT initialisation.
- **Eclipse:** attitude propagation relies on the IRU only; accumulated drift $< 0.01°/\mathrm{h} \times 1.5\,\mathrm{h} \approx 0.015° \ll 0.5°$ OE APE budget.

Sensor	Accuracy (3σ)	Power (W)	Redundancy rationale
STT (Sodern SED-36 class, heritage SELENE SED-16L) [35]	≤ 6 arcsec	3.0 each	Cold standby
CSS (Adcole Model 48330 class, heritage COTS) [35]	$\leq 2°$	≈ 0 each	Full 4π sr coverage; safe-mode Sun targeting
FSS (Adcole Model 48280 class, heritage OICETS/JEM) [35]	$\leq 0.05°$	0.3 each	Fine Sun-vector for SAP pointing
IRU (NG LN-200S) [35]	$< 0.01°$/h drift	12 each	Attitude propagation during eclipses
ACM (JAE, heritage MUSES-C) [35]	± 500 mG	1.1	ΔV monitoring during VOI
SPS [35]	Binary	≈ 0 each	Sun presence flag; triggers safe-mode

Table 32: Attitude sensor selection: performance and redundancy summary.

Sensor power budget. The computed value according to Tab. 32 is:

$$P_{\text{sens}} = 2 \times 3 + 0 + 2 \times 0.3 + 3 \times 12 + 1.1 + 0 = 43.7 \text{ W} \qquad \textbf{[computed]}$$

One STT in cold standby draws no power in the nominal cruise/science configuration; the sensor power figure above reflects that operating point, consistent with Tab. 35.

19 Actuator Selection and Sizing

19.1 Reaction Wheels

AKATSUKI carries four Ithaco/Goodrich Type-A reaction wheels (RW-A through RW-D), heritage MUSES-C (Hayabusa), in a tetrahedral (skewed) configuration: one per face of a regular tetrahedron, maintaining full three-axis control following any single-wheel failure [35]. Manufacturer-class data for this product line reports a maximum torque $T_w = 0.02$ N m and maximum momentum $H_w = 4$ N m s per wheel at up to 5100 rpm [35].

Tetrahedral envelope. For a regular tetrahedral array with wheel spin axes at the standard skew angle $\beta = \arccos(1/\sqrt{3}) \approx 54.74°$ from the nearest body axis [43, 44], the along-axis torque and momentum capacity vary between a maximum (all wheels contributing constructively) and a minimum (worst-case single-axis projection):

$$H_{\text{env,max}} = 4H_w \cos\beta \approx 9.2 \text{ N m s}, \qquad H_{\text{env,min}} = 2H_w \sin\beta \approx 6.5 \text{ N m s} \qquad \textbf{[computed]} \tag{14}$$

$$T_{\text{env,min}} = 2T_w \sin\beta \approx 0.033 \text{ N m} \qquad \textbf{[computed]} \tag{15}$$

Sizing on $H_{\text{env,max}}$ would assume that disturbances are always aligned with the most favorable wheel axis; the worst-axis quantities $H_{\text{env,min}}$ and $T_{\text{env,min}}$ are used throughout this section instead.

Slew torque sizing. Rather than assuming a reorientation time, the achievable slew time is reverse-sized from the wheels' own worst-axis torque capability, for the mission-derived 90° science-to-comms reorientation identified in Sec. 15: $\theta_m = 90° = 1.571$ rad. According to [21], the minimum slew time and the corresponding maximum slew rate and stored momentum are:

$$t_{\text{slew,min}} = \sqrt{\frac{4\, I_v\, \theta_m}{T_{\text{env,min}}}} \approx 183 \text{ s}, \quad \omega_{\max} = \frac{2\,\theta_m}{t_{\text{slew,min}}} \approx 1.72 \times 10^{-2} \text{ rad/s}, \quad H_{\text{slew}} = I_v\, \omega_{\max} \approx 3.0 \text{ N m s}$$

This is the mission's actual minimum reorientation time given the selected wheels' real torque authority: it is a direct, dimensioning output of the hardware choice.

Momentum saturation sizing. To avoid saturation over one full orbit ($T_{\text{orb}} = 30.5$ h $= 109\,800$ s) under the disturbances, the governing requirement is $H_{\text{req}} = \max(H_{\text{sat}}, H_{\text{slew}})$. The required wheel momentum storage per slew is $H_{\text{slew}} \approx 3.0$ N m s and $H_{\text{sat}} = T_d \times T_{\text{orb}} \approx 6.0$ N m s, so that H_{sat} governs: $H_{\text{req}} \approx 6.0$ N m s [21, 43, 45]. Against this requirement, the worst-axis envelope $H_{\text{env,min}} \approx 6.5$ N m s derived provides a margin of only $\approx 1.09\times$. The limited margin suggests that either a larger reaction wheel or a more frequent desaturation cadence should be considered in a future design iteration (Sec. 19.2).

Mass and power. For the selected Ithaco/Goodrich Type-A wheel: $m_w \approx 3.3$ kg, $P_w \approx 20$ W at rated torquex. With four: $m_{\text{RW}} = 4 \times 3.3 = 13.2$ kg, $P_{\text{RW}} = 4 \times 20 = 80$ W. During science operations only two wheels are active at full speed; realistic operational power is ≈ 40 W [35].

19.2 RCS Thrusters

Hydrazine monopropellant thrusters: 8×23 N (pitch/yaw, large maneuvers and desaturation) and 4×3 N (roll, fine corrections) [35]. The effective lever arm is assumed $L = 0.70$ m from CoM.

Desaturation fuel sizing. The propellant required for one momentum unloading event, assuming a wheel momentum storage of $H_w = 4$ N m s and $I_{\text{sp}} = 220$ s, is $m_{\text{desat}} = H_w/(L\, I_{\text{sp}}\, g_0) = 2.65 \times 10^{-3}$ kg/event, and the time to saturate a wheel under dominant GG+SRP is $t_{\text{sat}} = H_w/T_d \approx 20.2$ h. The wheels saturate in under a single orbit. Adopting a conservative operational desaturation cadence of once every 10 h $\ll t_{\text{sat}}$ to avoid approaching wheel saturation: $m_{\text{desat,total}} = N_{\text{desat. events}} \times m_{\text{desat}} = 1753 \times 2.65 \times 10^{-3} \approx 4.6$ kg over the full 2-year nominal mission. This is well within the 73.4 kg N_2H_4 tank budget (Tab. 15).

Perturbation from desaturation. A single 23 N thruster acting at the 0.70 m lever arm generates a reference torque of $M_{23\text{N}} = FL \approx 16.1$ N m. During a firing pulse of unknown duration t_p, the spacecraft first undergoes an acceleration phase and then, after the thruster is switched off, coasts at the residual angular rate until the reaction wheels, limited by their worst-axis control torque $T_{\text{env,min}} \approx 0.033$ N m (Sec. 19.1), bring the spacecraft back to rest. The angular excursions accumulated during these two phases are

$$\Delta\theta_{\text{acc}} = \frac{M_{23\text{N}} t_p^2}{2I_v}, \qquad \Delta\theta_{\text{brake}} = \frac{\omega_{\text{res}} t_{\text{brake}}}{2}.$$

Substituting $\omega_{\text{res}} = M_{23\text{N}} t_p / I_v$, $t_{\text{brake}} = I_v \omega_{\text{res}} / T_{\text{env,min}}$, gives the total pointing excursion as a function of the pulse duration

$$\Delta\theta_{\text{tot}} = \Delta\theta_{\text{acc}} + \Delta\theta_{\text{brake}} = \frac{M_{23\text{N}} t_p^2}{2I_v} + \frac{M_{23\text{N}}^2 t_p^2}{2I_v T_{\text{env,min}}}.$$

Imposing the conservative requirement $\Delta\theta_{\text{tot}} \leq 1^\circ$ (the interplanetary-cruise/VOI APE pointing budget, since desaturation is performed outside science windows) yields the maximum allowable pulse duration $t_p \leq 28$ ms, for which $\Delta\theta_{\text{acc}} \approx 0.002^\circ$, $\omega_{\text{res}} \approx 0.15^\circ/\text{s}$, $t_{\text{brake}} \approx 13.3$ s, and $\Delta\theta_{\text{brake}} \approx 1.0^\circ$. Therefore, the 8×23 N thrusters should be commanded using short ($\lesssim 30$ ms) pulses during momentum unloading.

20 Configuration and Activation Logic

20.1 Physical Placement

The physical placement of the ADCS components, reconstructed from the spacecraft configuration reported in [2, 35] and complemented where necessary by standard spacecraft layout practices [21], is the following:

- **RCS:** 8×23 N-class thrusters at bus corners (maximizing lever arm for pitch/yaw); 4×3 N-class thrusters on $\pm X$ faces (roll).
- **RWs:** tetrahedral configuration inside bus, near the CoM, minimizing mass-moment imbalance.

- **STTs:** $+Z$ panel, spaced $\sim 90°$ apart in the XZ-plane to avoid mutual FoV obstruction.
- **IRU:** near the CoM to minimize lever-arm errors in angular-rate measurement.
- **CSS:** distributed on the external surface to achieve full 4π sr coverage.

20.2 Activation Logic per Control Mode & Simultaneous Activation Constraints

Tab. 33 summarises the sensor/actuator combinations and enabling conditions per mode, inferred from the mission phase descriptions and control requirements of Sec. 2. Moreover:

- RCS thrusters are inhibited during nominal RW fine-pointing operations, since simultaneous wheel torque compensation and thruster actuation would result in unnecessary propellant expenditure and degraded pointing efficiency [46, 47].
- STTs are disabled for slew rates $> 0.5°/\mathrm{s}$ to prevent CCD image smear and loss of stellar centroid accuracy during attitude maneuvers [21].
- RW desaturation maneuvers are executed using short ($\lesssim 30\,\mathrm{ms}$) RCS pulses (Sec. 19.2), limiting the transient attitude excursion to $\approx 1°$, after which star-tracker attitude determination can resume.

Mode	Sensors	Actuators	Activation Logic
Safe Hold	CSS + SPS + IRU	RCS 23 N	Autonomous Sun search; 0.1 s control cycle; if Sun lost $\rightarrow$ all-CSS spin search pattern.
Cruise	1 $\times$ STT + IRU	RWs	3-axis stabilized; one STT in cold standby.
Science (OA–OD)	2 $\times$ STT + IRU	RWs	Dual STT voting; fine Venus-pointing; desaturation triggered on wheel-speed threshold.
VOI	IRU + ACM	OME + RCS	IRU-based attitude propagation; open-loop OME burn; RCS ready for contingency; ACM monitors ΔV.
Desaturation	1 $\times$ STT + IRU	RCS 23 N (in pairs)	RWs-speed threshold exceeded $\rightarrow$ opposing 23 N pairs fire in $\lesssim 30\,\mathrm{ms}$ pulses.
Eclipse (OE)	IRU	RWs	IRU attitude propagation only (STTs/CSS off due to shadow).

Table 33: Simultaneous activation of sensors and actuators per control mode [35, 36].

21 Subsystem Budgets

The mass, power and data budgets follow bottom-up from the hardware identified in Sections 18 and 19.

Mass Budget. The total ADCS dry mass represents $\approx 16\%$ of the spacecraft dry mass from literature, at the lower end of the range reported for similar interplanetary spacecraft with heritage, flight-proven AOCS hardware [21].

Component	Mass (kg)	Ref.
STT (Sodern SED-36 class) $\times$2	18.00	[35]
CSS (Adcole 48330 class) $\times$5	0.20	[35]
FSS (Adcole 48280 class) $\times$2	2.60	[35]
IRU (LN-200S) $\times$3	2.15	[35]
ACM (JAE)	0.09	[35]
SPS $\times$2	0.16	[35]
RWs (Ithaco/Goodrich Type-A) $\times$4	13.20	[35]
AOCU + DRV	17.80	[35]
Total ADCS dry mass	**54.20**	

Table 34: ADCS dry mass budget (propellant excluded).

Power Budget per Operational Mode. The following assumptions are adopted, upon [21, 35]:

- During nominal science and cruise operations, only two RWs are assumed to operate continuously at high speed, while the remaining wheels provide redundancy and momentum balancing.
- RCS electrical consumption is dominated by valve and line heaters rather than pulse firing duration, whose duty cycle is negligible in the average orbital budget.
- In OE and VOI configurations, STTs are disabled and attitude propagation relies on the IRUs.
- Safe mode disables fine-pointing hardware, operating on CSS/SPS only and survival heaters.

Mode	**Active RWs**	**RW Power (W)**	**RCS Power (W)**	**Sensor Power (W)**	**Total (W)**	**Main hardware**
Safe Hold	0	0	20	10	30	CSS, SPS, survival heaters
Interplanetary Cruise	2	40	0	38.5	78.5	1 STT + IRU
VOI (pre-burn)	0	0	50	14	64	IRU, ACM
Science (OA-OB-OC-OD)	2	40	0	38.5	78.5	Dual STT + IRU
Eclipse (OE)	2	40	0	14	54	IRU

Table 35: Estimated ADCS operational power budget reconstruction [21, 35].

The peak operational ADCS power demand is ≈ 79 W during science and cruise phases (each RW draws up to 20 W at rated torque per [35]; two wheels active nominally). Compared against available literature (more than 480 W at 1.0781 AU and more than 660 W on the Venus orbit [38]), the ADCS accounts for roughly 11–16% of the total platform power depending on the assumed total (500–700 W, [35]). These values are consistent with typical deep-space three-axis stabilized spacecraft and compatible with the remaining allocations, including the science payload and the TTMTC [21].

21.1 Data Budget

ADCS data handling is composed of low-rate housekeeping TLM transmitted to ground, and higher-rate internal data exchanges for real-time attitude estimation and control. The housekeeping TLM stream primarily consists of STT/IRU attitude quaternions at 10 Hz (≈ 100 B/s), RWs tachometer data at 2 Hz (≈ 20 B/s), and mode/status flags at 1 Hz (≈ 10 B/s). The resulting total telemetry rate is ≈ 130 B/s (≈ 1 kbps), negligible compared to the nominal 32 kbps DL capacity (Sec. 14). The dominant contribution instead arises from the internal ADCS data traffic exchanged between sensors, actuators, and the onboard computer, summarized in Tab. 36.

Data source & No. units N_i	**Assumed update rate f_i**	**Assumed packet size S_i**	**Internal data rate $D_i = N_i\ f_i\ S_i$**	**Ref.**
STT (× 1)	8 Hz	64 bytes	4.10 kbps	[35]
CSS (× 5)	10 Hz	16 bytes	6.40 kbps	[35]
IRU (× 1)	100 Hz	32 bytes	25.6 kbps	[48]
ACM (× 1)	10 Hz	16 bytes	1.28 kbps	[21]
RW telemetry (× 4)	10 Hz	16 bytes	5.12 kbps	[35]
Total ADCS data rate	–	–	42.5 kbps	–

Table 36: Internal ADCS data rate budget.

Given the number of units N_i, the update rate f_i, and the packet size S_i, the total internal ADCS data rate, as split in Tab. 36, is computed as the sum of the single internal data rates:

$$D_{\mathrm{ADCS}} = \sum_i N_i f_i S_i = 4.10 + 25.6 + 6.40 + 1.28 + 5.12 = 42.5 \text{ kbps} \tag{16}$$

This value represents the internal bus sizing requirement rather than a continuous DL demand. Only a small subset of the ADCS data is included in the housekeeping TLM stream (∼ 1 kbps), which remains negligible compared to the science-driven 32 kbps DL budget (Sec. 14).

22 EPS Architecture Overview and Rationale

AKATSUKI's Electrical Power Subsystem (EPS) was designed to guarantee continuous power availability throughout all the mission phases. The adopted architecture consists of three main elements:

- Two deployable Solar Array Paddles (SAPs) as primary Photovoltaic (PV) source;
- Two lithium-ion (Li-ion) batteries as secondary source;
- A Power Control Unit (PCU) for conditioning, regulation, charge control, and distribution.

The bus voltage is regulated at 50 V by a Series-Switching Regulator (SSR) [38]. Compared to a conventional 28 V bus, the higher-voltage architecture reduces current levels for a given power demand, thereby decreasing conductor mass and resistive losses within the spacecraft harness. [21]. The architecture is driven by the intense Venus solar flux (≈1.9× Earth value), a peak payload demand up to 500 W requiring deployable PV panels, and eclipse durations requiring battery support [49, 50] (see Sec. 1); RTGs and fuel cells are excluded on mass and maintenance grounds.

22.1 Design Rationale for Key EPS Choices

Triple-junction InGaP/GaAs/Ge cells. Compared to silicon cells, these cells provide higher conversion efficiency, improved radiation tolerance, and better high-temperature performance — critical for Venus proximity, where solar irradiance and proton fluence both significantly exceed Earth-orbit's.

Optical Solar Reflectors (OSRs). The rear face of each SAP is fully covered with OSRs to minimize albedo and IR input from Venus [49].

Lithium-ion batteries. Li-ion was chosen for its specific energy density ($\varepsilon \approx 107$ Wh/kg [50] vs. ∼35 Wh/kg for NiCd [21]), directly reducing EPS mass (see Sec. 5.3).

Series-Switching Regulator. Since solar-array output varies with temperature and illumination conditions, an active bus-voltage regulation is required to ensure stable operations. Compared to pure dissipative shunt-regulation architectures, SSR improves overall conversion efficiency [38].

Solar Array Drive Assembly (SADA). These drive each SAP, and rotate about the bus Y-axis, decoupling Sun tracking from ADCS and enabling off-pointing for thermal management [38, 49].

23 Power Budget as Requirement

The power budget constitutes the input requirement for the EPS. Public literature does not provide a complete official equipment-level matrix; therefore the reconstruction distinguishes between values from literature (directly traceable to mission papers), computed values (derived from instrument/subsystem data) and assumed values (coming from analogy with similar missions and marked as $\doteq$). The seven EPS modes cover the most energy-relevant operational conditions, as shown in Tab. 37.

EPS mode	Role in the power budget
Safe Hold	Survival and attitude recovery; minimum continuity verification.
Cruise	HKT, TMTC LP, heaters, ltd. science.
VOI	Critical phase: PS preparation, ADCS, monitoring; autonomous logic.
Science (OA, OB, OC, OD)	Multi-camera imaging; representative PV-powered case.
Science (UVI FW peak)	Peak verification during UVI filter wheel motion.
Science (OE)	Battery-driving case.
Science (OF)	Radio-science with RS/USO and HGA.
TMTC Peak	DL to Earth, driven by TMTC HP.

Table 37: EPS modes selected for the power budget reconstruction, according to previous parts [4].

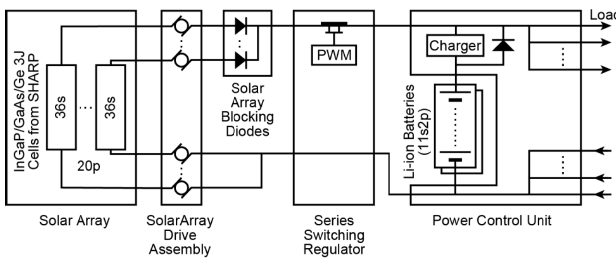

Figure 8: Block diagram of the AKATSUKI Electrical Power Subsystem (EPS) [38].

23.1 Traceable Loads and Scientific Payload

The load for the science modes is reconstructed from instrument-level data. IR2 already includes the cryo-cooler (Sec. 1); therefore it is not added separately. Nominal multi-camera load: 192.2 W [4]; during UVI filter wheel motion, UVI increases 19 W → 34 W and the payload rises to 207.2 W [4, 5].

Element	Power [W]	Use in the matrix
IR1	9.4	Included in science acquisition modes.
IR2	114.8	Includes the 50 W Stirling cryo-cooler.
UVI	19 nominal / 34 FW	19 W during observation; 34 W during filter wheel motion.
LIR	29	Included in the multi-camera payload.
DE	20	Shared electronics and data recorder.
LAC	n.a.	Included in the Eclipse OE residual.
RS/USO	n.a.	Associated with OF mode; specific loads not disaggregated.

Table 38: Traceable scientific powers and treatment of unavailable loads [4, 5] (Sec. 1).

23.2 Residual Allocation

The residual covers TCS, OBDH, EPS PCDU [51] and TMTC LP (100–130 W by analogy [21]); for OE, 750 Wh/90 min requirement [38] implies 500 W average, giving $P_{\mathrm{res,OE}} = 500 - 54.0 - 93.2 = 352.8$ W.

23.3 EPS Power Budget Reconstruction

The EPS power budget is reconstructed according to ESA system engineering practice [20]. Each operational mode combines active subsystems, including PL, ADCS, PS and TMTC. Nominal consumption P_{nom} is computed as the sum of active loads, while required power P_{req} includes a uniform 20% system-level margin to cover subsystem simultaneity uncertainties, degradation, and operational contingencies. This provides a conservative estimate of EPS design-driving conditions without a fully time-resolved mission simulation. Table 39 reports the reconstructed power budget for each mode.

EPS mode	Payload [W] [4]	ADCS [W] [P. 14]	PS [W] [P. 7]	TMTC [W] [P. 3.8]	Residual [W] [21]	P_{nom} [W]	P_{req} [W]
Safe Hold	0	30.0	0	0	$\doteq$ 130.0	160.0	192.0
Interplanetary Cruise	20.0	78.5	50.0	0	$\doteq$ 100.0	248.5	298.2
VOI	0	64.0	118.0	0	$\doteq$ 110.0	292.0	350.4
Science (OA, OB, OC, OD)	192.2	78.5	0	0	$\doteq$ 130.0	400.7	480.8
Science peak (UVI FW)	207.2	78.5	0	0	$\doteq$ 130.0	415.7	498.8
Eclipse OE	incl. resid.	54.0	0	93.2	352.8	500.0	600.0
Radio Occultation OF	incl.	78.5	0	93.2	$\doteq$ 120.0	291.7	350.0
Communication / DL	0	78.5	0	93.2	$\doteq$ 110.0	281.7	338.0

Table 39: Reconstructed EPS power matrix with 20% ESA margin. TMTC refers to power peaks.

23.4 Mode Durations and Associated Energies

Based on Table 39, Table 40 translates power profiles into energy consumption over representative mission durations, highlighting the modes that drive long-term energy balance and battery sizing.

Mode	P_{nom}	P_{req}	Duration	E_{nom}–E_{req}	EPS role
VOI burn	292.0 W	350.4 W	715.5 s (see Sec. 5.3)	58–70 Wh	Continuity & reliability.
VOI eng. window	292.0 W	350.4 W	$\doteq$ 1 h	$\doteq$ 292–350 Wh	†
Science OA–OD	400.7 W	480.8 W	20 h/orbit [4]	8.0–9.6 kWh	Drives PV sizing.
Science OE	500.0 W	600.0 W	1.5 h [38]	750–900 Wh	Battery-driving case.
Science OF	291.7 W	350.0 W	$\doteq$ 1–2 h/event	$\doteq$ 0.29–0.58 kWh	For radio-science.
Communication	281.7 W	338.0 W	6 h/contact (see Sec. 3.8)	1.69–2.03 kWh	Illumination constraint.

† *Note:* Eng. window stands for engineering window and includes conservative pre/post-burn verifications.

Table 40: Energy associated with the main EPS modes. VOI is not a battery-sizing case.

23.5 Derived EPS Requirements

Table 41 synthesizes the key EPS design requirements derived from the previous analyses, linking subsystem-level assumptions to system-level constraints.

Requirement	Reconstructed value	EPS implication
Envelope spacecraft-level	<500 W nominal	Global consistency limit.
Max battery-side load	600 W in Eclipse OE	Demanding battery case.
Battery energy	750 Wh nominal; 900 Wh with margin	Driver of secondary source.
Science payload	192.2 W nominal; 207.2 W peak (UVI FW)	Driver of illuminated modes.
Solar array capability	>660 W at Venus orbit [49]	Must cover loads + recharge.
TMTC high-power	93.2 W (Sec. 3.8)	Included in OF, DL, OE.

Table 41: EPS requirements derived from the power budget.

24 Primary Source: Solar Array Sizing and Configuration

24.1 Cell Technology and Material Selection

AKATSUKI uses SHARP Corp. InGaP/GaAs/Ge triple-junction cells (JAXA-QTS-2130/502), 10 strings × 36 cells per panel [49]; a short technology comparison is available in Tab. 42.

Solar cell type	η_{BOL} [%]	Advantage for AKATSUKI
InGaP/GaAs/Ge triple-junction	28–30	High efficiency, radiation tolerance, thermal performance
GaAs single-junction	18–22	Better than Si but lower than triple-junction
Silicon	12–18	Mass-penalising; poor high-T performance

Table 42: Comparison of battery technologies considered for AKATSUKI [50, 21].

Given BOL conversion efficiency $\eta_{\mathrm{BOL}} = 0.283$ [49] and annual degradation rate for this cell class in the Venus proton environment $D = 1.5\%/\mathrm{yr}$ [21], the EOL efficiency after $n = 2$ yr is:

$$\eta_{\mathrm{EOL}} = \eta_{\mathrm{BOL}} (1 - D)^n = 0.283 \times (0.985)^2 = 0.274$$

24.2 Solar Flux at Venus and Array Area Sizing

Solar irradiance at Venus is $G_{\mathrm{V}} = 2649\ \mathrm{Wm}^{-2}$. SAPs rotate about the spacecraft Y-axis to track the Sun; taking the worst-case incidence angle $\alpha = 10°$ [49] (Sec. 14) (since any residual incidence angles arise from the out-of-plane solar declination and from intentional thermal off-pointing, thanks to the SADA), with distribution efficiency $\eta_{\mathrm{dist}} \doteq 0.90$ and design power $P_{\mathrm{design}} = 490$ W (according to OA with no margins), yields the required active cell area:

$$P_{\mathrm{arr,req}} = \frac{P_{\mathrm{design}}}{\eta_{\mathrm{dist}}} = \frac{490}{0.90} = 544\ \mathrm{W} \implies A_{\mathrm{req}} = \frac{P_{\mathrm{arr,req}}}{G_{\mathrm{V}}\, \eta_{\mathrm{EOL}}\, \cos\alpha} = \frac{544}{2649 \times 0.274 \times 0.985} = 0.760\ \mathrm{m}^2$$

Adding a 15% packing-factor loss (busbars, bypass diodes, cell gaps [21]) leads to $A_{\mathrm{panel,req}} = 0.894\ \mathrm{m}^2$.

24.3 Reverse Sizing Check: Eclipse Recharge

The solar arrays must supply enough power to simultaneously run the spacecraft in sunlight and recharge the batteries after eclipse. Given the eclipse load (with 20% margin) $P_e = 600$ W, eclipse time $T_e = 1.5$ h, sunlit time $T_s = 28.5$ h and line efficiencies $X_e \doteq 0.65$, $X_s \doteq 0.85$, standard sizing yields:

$$P_{\mathrm{sa}} = \frac{P_e\, T_e}{X_e\, T_s} + \frac{P_s}{X_s} = \frac{600 \times 1.5}{0.65 \times 28.5} + \frac{500}{0.85} = 637\ \mathrm{W}$$

Maximum specific power at Beginning Of Life (BOL) (inherent degradation $I_d \doteq 0.77$ [21]) is therefore:

$$P_{\mathrm{BOL,sp}} = \eta_{\mathrm{BOL}}\, G_{\mathrm{V}}\, I_d = 577\ \mathrm{W/m}^2 \implies P_{\mathrm{EOL,sp}} = 577 \times (0.985)^2 = 560\ \mathrm{W/m}^2$$

Finally, the minimum required geometric area is $A_{\mathrm{SA,req}} = P_{\mathrm{sa}}/P_{\mathrm{EOL,sp}} = 1.14\ \mathrm{m}^2$.

24.4 Actual Array Configuration and Oversizing Rationale

AKATSUKI carries two SAPs, each 1.430 m × 1.036 m, with a boom of 0.9 m and a mass of 7.64 kg per paddle (including boom) [49]. The total deployed cell area is $A_{\text{total}} = 2.964 \text{ m}^2$, which is ∼3× the required minimum since the minimum per panel is 0.894 m^2 and array power generation at EOL is:

$$P_{\text{EOL}} = A_{\text{total}}\, G_{\text{V}}\, \eta_{\text{EOL}}\, \eta_{\text{dist}} \cos\alpha = 2.964 \times 2649 \times 0.274 \times 0.90 \times 0.985 = 1911 \text{ W}$$

The 3× margin covers OSR packing fraction loss, high-temperature current degradation, and single-paddle failure redundancy [38, 49]. The regulated bus capacity is 700 W [4]; the SSR continuously dissipates the excess (1178 W at EOL) via shunt elements, according to literature [38]. Reported generated power is higher than 480 W at 1.08 AU and more than 660 W at Venus orbit [49].

25 Secondary Source: Battery Sizing

25.1 Cell Technology and Architecture

Li-ion was selected for its specific energy density ($\varepsilon \geq 107$ Wh/kg [50]) over NiH_2 and NiCd (which are historically robust but mass-penalising, given that they are in the 40–75 and 30–50 specific energy ranges, respectively); two 23.5 Ah packs in parallel, 11 cells in series each [38].

25.2 Eclipse Energy Requirement and Capacity Check

Since the maximum eclipse duration is $T_e = 1.5$ h [38], OE demand with 20% margin is 600 W, yielding $E_{\text{ecl,req}} = 600 \times 1.5 = 900$ Wh required eclipse energy. For Li-ion at ≈576 cycles (Sec. 14), $\text{DOD}_{\max} \doteq 30\%$ maintains EOL capacity above requirement [21, 50]. Therefore:

$$\text{Round-trip efficiency } \eta_{\text{bat}} := 0.95 \Rightarrow C_{\text{bat,req}} = \frac{E_{\text{ecl,req}}}{\text{DOD}_{\max}\, \eta_{\text{bat}}} = \frac{900}{0.30 \times 0.95} = 3158 \text{ Wh} \gg 2350 \text{ Wh [50]}$$

The higher $C_{\text{bat,req}}$ reflects a conservative 30% DOD design rule (see Sec. 30); AKATSUKI instead operates at the documented 41%–85% State of Charge (SoC) window (44% usable DOD) [38], yielding $C_{\text{installed}} = 1034$ Wh, meeting the 750 Wh nominal requirement (38% DOD with margin), within Li-ion capabilities [38].

25.3 Battery Management Strategy and Battery Mass

Rather than oversizing the battery, a mitigation strategy is adopted against Li-ion degradation, maintaining low operational temperatures and low SoC (10% during storage; 41% during cruise, see Fig. 9). Using the cell stack upper bound of 22 cells × 785 g and $\varepsilon = 107$ Wh/kg [50], nominal OE yields:

$$m_{\text{bat}} = \frac{E_{\text{ecl,nom}}}{\varepsilon} = \frac{750}{107} = 7.0 \text{ kg (lower bound)} \quad \Longrightarrow \quad m_{\text{bat,stack}} = 22 \times 0.785 = 17.3 \text{ kg}$$

The actual masses are consistent with values reported in mission data [50].

Parameter	Value	Source
Number of SAPs	2	literature [49]
Dimensions per SAP	1.430 m × 1.036 m	literature [49]
Total deployed area	2.964 m^2	computed
Cell type	InGaP/GaAs/Ge 3J	literature [49]
Topology per panel	10 strings × 36 cells	literature [49]
η_{BOL} (AM0, 28°C)	28.3%	literature [49]
G_{V} at 0.71 AU	2649 W/m^2	computed
η_{EOL} (2 yr)	27.4%	computed
Min. required area	0.894 m^2	computed
Venus-orbit output	>660 W per panel	literature [49]
P_{EOL} (both panels)	1911 W	computed
Mass per paddle	7.64 kg (incl. boom)	literature [49]
Total SAP mass	15.28 kg	computed

Table 43: Solar array sizing summary.

Parameter	Value	Source
Battery type	Li-ion, 2 packs in parallel	literature [50]
Topology	2 × 11 cells in series	literature [38]
Cell capacity	23.5 Ah	literature [50]
Total capacity	47 Ah	computed
Specific energy	≥107 Wh/kg	literature [50]
Cell mass (max)	785 g	literature [50]
Mission DOD	44% (SoC 41%→85%)	literature [38]
Design DOD	≐ 30%	assumed [21]
Installed energy	2350 Wh (at 50 V, 47 Ah)	computed
Usable energy	1034 Wh (at 44% DOD)	computed
Eclipse req.	750 Wh (nom.)	literature [38]
Eclipse req.	900 Wh (+20%)	computed
Capacity loss	≤20% over mission	literature [50]

Table 44: Secondary source sizing summary.

26 Power Budget as Performance

Tab. 45 cross-checks EPS capability against the demand of Tab. 39 for each mode. The most constrained sunlit mode is OA: the 700 W regulated bus leaves only a 219 W margin above the demand. The most constrained eclipse condition is OE: 900 Wh required drawn from 1034 Wh usable — which also confirms that the architecture can sustain orbit eclipses up to 1600 Wh [38].

Mode	Demand [W]	Array supply [W]	Battery availability [Wh]	Margin
Safe Hold	192	1911	—	+1719 W
Cruise (0.71 AU)	298	$\geq$ 962 ($P \approx$ 962 W @ 1 AU)	—	+664 W
VOI	350	1911	—	+1561 W
Science OA	481	700 (regulated)	—	+219 W (bus)
Eclipse OE	600	0	1034 (usable)	+434 Wh

Table 45: Power budget as performance (EOL, 20% margin in demand).

27 Bus Architecture and Regulation

The solar arrays output is routed SAPs $\rightarrow$ SBDs $\rightarrow$ SSR (50 V regulated) $\rightarrow$ PCU [38]. The SSR (buck topology) reduces losses vs. dissipative shunts; Solar Array Blocking Diodes (SBDs) prevent reverse current; excess power beyond the 700 W bus is shunt-dissipated. The PCU manages battery charge/discharge, fault-isolation relays, and 5/12 V DC/DC rails [38]. See Tab. 46 for more details.

Element	Function	Main constraint
SBD	Keeps string outputs independent and prevents reverse charging from the batteries to the SAPs.	Introduces conduction losses and additional complexity in the strings.
SSR	Conditions the raw panel power to supply the regulated bus.	Step-down conversion and possible electromagnetic disturbances associated with switching.
SADA	Transfers power and orients the panels toward the Sun.	Presence of moving parts and reliability of mechanisms/slip rings.
PCU	Manages battery charge and bus distribution.	Thermal limits and maximum throughput.

Table 46: Main elements for regulation, control, and distribution.

28 Subsystem Budgets

Component	Mass	Label	Source
Solar array paddles	15.28 kg	literature	[49]
2 × SADAs assemblies	$\doteq$ 2.0 kg	estimated	[21]
2 × Battery packs	~13.6 kg	computed	
PCU (overall)	$\doteq$ 5.0 kg	estimated	
Harness (10% of above)	3.6 kg	estimated	[21]
Total EPS dry mass	≈39.5	computed	

Table 47: EPS mass budget.

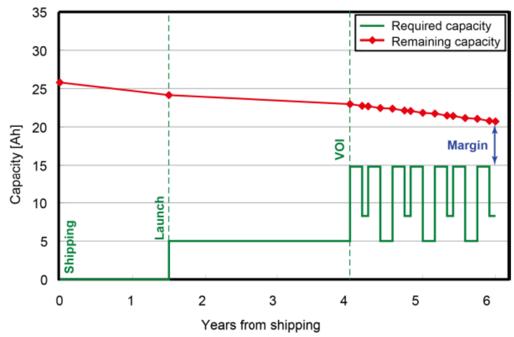

Figure 9: Original battery operation plan [38].

According to Tab. 47, EPS dry mass fraction is consistent with the typical 8–12% range for interplanetary PV/battery systems [21]. The EPS internal power consumption (SSR losses, PCU control, relay drivers) is folded into the residual in Tab. 39. The total solar array output at Venus EOL is 1911 W, of which at most 700 W is delivered to the regulated bus [4]. Battery volume $V_{\text{bat}} = 13.6/2.4 \approx 5.7$ L (using $\rho_{\text{bat}} = 2.4$ kg/L for packaged Li-ion [21]) fits inside the central bus structure with an additional PCU/SSR volume $\doteq$ 3 L. EPS telemetry (bus voltages, battery SoCs, cell temperatures, shunt status) at 1 Hz with 20 channels of 16-bit data $\Rightarrow \dot{D}_{\text{EPS}} \approx 20 \times 1 \times 16 \approx 0.3$ kbps ($\ll$ DL capacity, see Part 3.8).

29 Component Positioning and Pointing Requirements

29.1 Physical Placement

Both SAPs are symmetrically mounted on the $\pm Y$ faces of the spacecraft bus [49], with rotation axes aligned along the Y-axis and SPS near each paddle outer edge for Sun acquisition [49]. This configuration ensures full ±180° Sun tracking without shadowing the instrument-bearing $+Z$ face, avoids interference with the OME plume ($-Z$) and HGA ($+Z$) layouts from (Sec. 1) (Sec. 3.8), minimises SRP torque imbalance and related ADCS desaturation demand (Sec. 14), while the $\pm Y$ faces also provide radiative cooling surfaces [49] (Sec. 14). The battery packs are inside the central bus near the CoM to reduce dynamic balance shifts during charge/discharge cycles and benefit from structural thermal insulation [50, 4]. The PCU/SSR are mounted on a cold plate inside the bus to reject dissipated heat toward the radiators.

Component	Location and rationale	Source
SAPs	External, $\pm Y$ body faces; 1-axis SADA rotation about Y; SPS at outer edge.	[49]
Battery packs	Internal, near CoM; minimises harness length and thermal gradients.	[50]
PCU / SSR	Internal EPS bay on cold plate; waste heat rejected to radiators.	[38]
RTGs/Fuel cells	Not adopted; photovoltaic/battery architecture.	[38]

Table 48: EPS component positioning.

29.2 Pointing Requirements and Implemented Solutions

AKATSUKI's pointing architecture represents a split between main-body pointing and solar-array pointing [4, 38]. The ADCS controls the main body, which is three-axis stabilized, to direct the cameras toward their targets and the HGA toward Earth. The EPS pointing requirement is fundamentally different: the SAPs must remain favourably oriented toward the Sun independently of the main body attitude. This conflict is resolved by the single-axis SADA per wing (although it is not used merely to maximize power generation). The intense Venusian solar flux makes cell overheating a primary design constraint. Intentional panel off-pointing is therefore a critical thermal management strategy to balance electrical generation against heat loading while maintaining spacecraft attitude [38, 4].

Pointing need	Implemented solution	Source
SAP Sun tracking	1-axis SADA rotation about Y-axis; SPS	[49]
PL (Venus)	3-axis body attitude control (through ADCS (Sec. 14))	[38]
HGA (Earth)	Spacecraft body attitude control	[38]
Thermal off-pointing	SADA intentional off-pointing; OSRs on rear face	[49]

Table 49: Pointing needs and implemented EPS solutions.

30 Consistency Verification

- **PV array:** ×1.6 margin explained by OSR packing, high-temperature current loss, radiation degradation, and single-paddle-failure redundancy [38]. Moreover, for a InGaP/GaAs/Ge cell with $V_{\mathrm{MPP}} \approx 2.33$ V, 36 cells in series yield $V_{\mathrm{string}} \approx 84$ V > 50 V. For this reason, each physical string needs to be sub-divided into two 18-cell sub-strings connected through blocking diodes, or the cells to operate at a lower $V_{\mathrm{MPP}} \approx 1.39$ V in Venus high-irradiance environment [21].
- **Battery capacity & DOD:** usable 1034 Wh @ 44% DOD covers nominal eclipse with 38% margin [38]. Operational window 41%–85% SoC (44% DOD) consistent with standards from [21]. The conservative 30% DOD design rule exceeds the installed 2350 Wh, since this is a sizing guideline for worst-case cycle life. JAXA verified through life testing that the selected cell sustains ≥576 cycles at 44% DOD with ≤20% capacity loss [50], so the mission design deliberately operates at 44% DOD rather than the more conservative 30% threshold.
- **Bus power:** arrays generate > 660 W at Venus [49], regulated to 700 W [4]; peak science demand 481 W gives 31% positive bus margin.

31 TCS Architecture Overview and Design Rationale

The Thermal Control Subsystem (TCS) of AKATSUKI is responsible for maintaining spacecraft equipment and scientific instruments within allowable temperature limits throughout all mission phases [52]. Operations near Venus expose the spacecraft to a severe thermal environment characterized by intense solar irradiance (Sec. 21.1), planetary Infrared (IR) and albedo flux, and eclipse transitions (Sec. 1). Under these conditions, the TCS must manage both excess heat and heat losses, preventing overheating during sunlit operations while ensuring that critical subsystems remain above their minimum allowable temperatures during cold-case conditions. In addition it must provide the thermal stability required by temperature-sensitive payloads and limit thermal gradients across the bus.

Based on available mission documentation, TCS adopts a predominantly Passive Thermal-Control (PTC) architecture complemented by localized Active Thermal-Control (ATC) elements (see Secs. 34–35). This is inferred from the use of Multi-Layer Insulation (MLI) blankets, OSRs and other thermal-optical surface treatments, as well as Reversible Thermal Panels (RTPs), as primary heat management tools [49]; the limited spacecraft power budget (see Sec. 21.1); the extensive thermal-vacuum and thermal-cycling qualification campaigns indicating a design philosophy based on material robustness and passive thermal-management; the absence in literature of large dedicated ATC assemblies such as pumped-fluid loops. A predominantly passive architecture also limits subsystem complexity and operational risk, improving reliability [52]. Tab. 50 summarizes the temperature constraints and associated thermal drivers governing the design of the principal spacecraft hardware elements.

Component	Op. Range	Survival Range	Thermal Driver	TCS Solution	Ref.
Bus (system)	$< +20\,^\circ$C	—	Spacecraft-level thermal stability under Venus hot-case conditions.	RTP-based radiative control, MLI, OSRs and thermal-optical coatings.	[53]
DPU / OBC	$-20 \to +50\,^\circ$C	$-40 \to +70\,^\circ$C	Performance degradation caused by solar flux and internal dissipation.	Thermal coupling to the controlled spacecraft bus.	[21]
PCDU	$-30 \to +60\,^\circ$C	$-40 \to +70\,^\circ$C	High internal dissipation and reliability of power electronics.	Conductive coupling to bus; localized heaters during cold-case.	[54]
Batteries	$+10 \to +25\,^\circ$C	$0 \to +40\,^\circ$C	Temperature-dependent lifetime, charge efficiency and capacity.	Dedicated heaters, MLI insulation and thermal coupling to bus.	[38]
Tanks + Lines	$+5 \to +40\,^\circ$C	$> +2\,^\circ$C (N_2H_4); $> -15\,^\circ$C (MON-3)	Propellant freezing limits drive heater sizing.	Pre-heating, dedicated heaters, thermal doublers and MLI.	[21, 55, 56]
IMU	$-54 \to +71\,^\circ$C	$-62 \to +85\,^\circ$C	Lower temperature bound set by gyro-bearing lubrication.	Thermal coupling to spacecraft bus + survival heaters.	[48]
RW	$-20 \to +60\,^\circ$C	$-30 \to +70\,^\circ$C	Not critical for thermal design.	PTC through bus environment.	[57]
SPSs	$-10 \to +50\,^\circ$C	$-30 \to +60\,^\circ$C	Measurement accuracy and thermal stability.	Thermal isolation, MLI protection and controlled conductive coupling.	[58]
Antennas	$-120 \to +120\,^\circ$C	$-150 \to +150\,^\circ$C	No critical thermal requirement.	No dedicated heaters required.	[59]
SAPs	$-170 \to +184\,^\circ$C	$-180 \to +200\,^\circ$C	Elevated temperatures reduce efficiency and accelerate degradation.	OSRs on rear faces, thermal-optical coatings and SADA off-pointing.	[49, 21]
IR1 detector	Nominal: $\sim -13\,^\circ$C	—	Reduced detector noise and improved SNR for NIR imaging.	Thermal isolation from bus + Dedicated radiative cooling path.	[60]
IR2 detector	$-213 \to -203\,^\circ$C	—	Cryogenic operation minimizes dark current and thermal noise.	50 W Stirling cryocooler, dedicated cold plate and thermal isolation.	[60]
LIR detector	$40 \pm 0.01\,^\circ$C	—	Radiometric accuracy requires highly stable detector temperature.	Active thermoelectric (Peltier) closed-loop temperature control.	[60]

Table 50: Thermal constraints and thermal-control approach for key AKATSUKI subsystems.

32 Mission Thermal Environment

Tab. 51 summarizes the external and internal thermal loads encountered during the mission. The dominant external heat loads are the direct solar flux $q_\odot$, the planetary albedo flux q_{alb}, and the planetary IR flux q_{IR} [59], while deep space ($T_{\text{space}} \approx 3\,\text{K}$) acts as the primary thermal sink [21]. Internal heat generation, Q_{int}, is the thermal power dissipated by onboard equipment. The documented maximum internal dissipation of 500 W is adopted as the upper bound, while lower values are inferred from the expected electrical activity during each mission phase. In addition, the TCS provides up to $\approx$

300 W of supplemental heating power through onboard heaters [53].

Mission Phase	$q_\odot$ [W/m^2]	q_{alb} / q_{IR} [W/m^2]	Q_{int} [W]	Dominant TCS Driver / Mitigation
Launch (1 AU)	1368	410 / 230	200–300	Risk of N_2H_4 freezing before full SAP deployment and thermal stabilization. MLI, heaters and thermal doublers reduce thermal transients and maintain propulsion components above survival temperature.
Cruise (1.0 → 0.71 AU)	1368 →2649	∼0 / ∼0	250–400	Full exposure to deep space → strong radiative losses. MLI limits heat loss. Localized heaters keep critical hardware within operational limits.
VOI (∼0.71 AU)	2649	668 / 415	450–500	**S**olar + albedo + planetary IR + peak internal dissipation → maximum thermal load. OSRs minimize solar absorption, thermal doublers spread localized heating, radiators reject excess heat.
Venus Orbit	2649	668 / 415	450–500	Payload and cryocooler operation requires continuous heat rejection. Radiators, OSRs, MLI and SADA off-pointing maintain thermal equilibrium and reduce absorbed solar power.
Venus Eclipse (OE only)	0	0 / 415	300–500	Solar input disappears while radiative cooling remains significant. MLI minimizes heat losses; heaters maintain batteries, electronics and propulsion lines within allowable temperatures.

Table 51: TCS thermal drivers and mitigation strategies for each mission phase [53, 61]. Albedo and planetary IR fluxes are computed at $h = 550\,\mathrm{km}$.

Despite MLI coverage, the intense Venus solar environment still results in an estimated parasitic heat leakage ≈ 140 W into the spacecraft bus.[53].

33 Hot and Cold Case Selection and Mono-Nodal Sizing

The spacecraft is modelled as a thermally equivalent sphere. For the mono-nodal sizing, operational temperatures from Tab. 50 are adopted to avoid overly conservative sizing [59, 62]: $T_{sc}^{min} = 298$ K (tank lower operational limit) and $T_{sc}^{max} = 313$ K (tank upper operational limit). A narrow bus-level constraint is intentionally not used, since it rises the chance to result in unrealistic requirements [59]; the actual constraints are enforced as deepened in Sec. 34. The equivalent sphere radius R_{eq} is derived from the bus outer surface area $A_{tot} = 10.00$ m^2 ⇒ $R_{eq} = 0.892$ m ⇒ $A_{cross} = \pi R_{eq}^2 = 2.50$ m^2 [12].

The spacecraft is coated with aluminized Kapton 5 mil [12], giving $\alpha_{sc} \doteq 0.46$ and $\varepsilon_{sc} \doteq 0.88$ [63]. The nominal internal power dissipation bounds are taken from the EPS power budget (Sec. 21.1): $Q_{int}^{min} = 160\,\mathrm{W}$ (Safe Hold mode) and $Q_{int}^{max} = 500\,\mathrm{W}$, retained as a conservative bounding envelope (see Sec. 33).

Taking planetary albedo $a = 0.30$ [59] and nominal periapsis orbit radius $r_{orb} = R_{Venus} + h = 6051.8 + 550 = 6601.8\,\mathrm{km}$ (Sec. 1), the external radiative heat fluxes are computed following ECSS [59], with $(R_{Venus}/r_{orb})^2$ factor accounting for geometric attenuation from the planetary surface to the orbit:
$q_{alb} = q_\odot \cdot a\,(R_{Venus}/r_{orb})^2 = 667.8\ \mathrm{W\,m^{-2}}, \quad q_{IR} = \sigma\,\varepsilon_{Venus}\,T_{Venus,space}^4\,(R_{Venus}/r_{orb})^2 = 414.9\ \mathrm{W\,m^{-2}}$

These values are computed by modelling Venus as a diffuse graybody emitter characterized by an emissivity $\varepsilon_{Venus} = 0.80$ and an average effective radiating temperature $T_{Venus,space} = 323\,\mathrm{K}$ [21, 59]. These are heat flux densities; the corresponding absorbed powers [W] are obtained in Sec. 33 multiplying by the appropriate effective areas.

Hot Case. This corresponds to the sunlit periapsis passage around Venus during OA/OD mode, when all three external fluxes are simultaneously at their peak. The value $Q_{int}^{max} = 500\,\mathrm{W}$ is also considered for a conservative analysis, even though the physically consistent hot case is the UVI FW peak (≈ 416 W (Sec. 21.1)). Keeping $h = 550\,\mathrm{km}$, the view factor from the equivalent sphere to the planet is $F_{PL} = 0.30$. The absorbed heat powers are then computed using $A_{cross}^{PL} = A_{tot} \times F_{PL} = 3.00\,\mathrm{m}^2$, as [59]:

$$Q_{\odot} = A_{\text{cross}}\, \alpha_{\text{sc}}\, q_{\odot} = 3046.4\,\text{W}, \quad Q_{\text{alb}} = A^{\text{PL}}_{\text{cross}}\, \alpha_{\text{sc}}\, q_{\text{alb}} = 921.6\ \text{W}, \quad Q_{\text{IR}} = A^{\text{PL}}_{\text{cross}}\, \varepsilon_{\text{sc}}\, q_{\text{IR}} = 1095.3\ \text{W}$$

The radiative area facing space is $A_{\text{space}} = A_{\text{tot}} - A^{\text{PL}}_{\text{cross}} = 7.00\ \text{m}^2$. The cosmic microwave background sets the deep-space sink at $T_{\text{space}} = 3\,\text{K}$ [21]. The hot equilibrium temperature without radiators is:

$$T^{\text{hot}}_{\text{sc}} = \left(\frac{Q_{\odot} + Q_{\text{alb}} + Q_{\text{IR}} + Q^{\text{max}}_{\text{int}}}{\sigma\, \varepsilon_{\text{sc}}\, A_{\text{space}}} + T^4_{\text{space}} \right)^{1/4} \approx 355\ \text{K}\ (82\ ^{\circ}\text{C})$$

This significantly exceeds $T^{\text{max}}_{\text{sc}} = 313\,\text{K}$, confirming that radiators are mandatory. Using $\varepsilon_{\text{rad}} = 0.85$, $\alpha_{\text{rad}} < 0.20$ (OSR-coated surface) [21], and targeting $T_{\text{design}} = T^{\text{max}}_{\text{sc}} - 15\ \text{K} = 298\ \text{K}$:

$$Q_{\text{tot}} = Q_{\odot} + Q_{\text{alb}} + Q_{\text{IR}} + Q^{\text{max}}_{\text{int}} = \sigma\, \varepsilon_{\text{sc}}\, A_{\text{space}}\, (T^4_{\text{design}} - T^4_{\text{space}}) + \sigma\, \varepsilon_{\text{rad}}\, A^{\text{min}}_{\text{rad}}\, (T^4_{\text{design}} - T^4_{\text{space}})$$

From which $A^{\text{min}}_{\text{rad}} = 7.4\ \text{m}^2$. This exceeds the available radiator surface of 5 m^2 [53]. This shortfall is mitigated through SADA off-pointing and MLI zonal insulation, consistent with analogous missions (e.g., Venus Express [63]).

Cold Case. For the cold-case assessment, the RTPs are assumed to remain in their stowed configuration, thereby minimizing the effective radiative rejection area. The contribution of secondary radiative surfaces (e.g., OSR-coated SAP rear faces) is neglected, and only the spacecraft bus external surface is considered in the radiative loss term, yielding a conservative first-order estimate.
For the cold-case analysis, a conservative scenario is assumed in which the spacecraft operates in Safe Hold mode while experiencing a Venus eclipse. In this reduced-power contingency configuration, non-essential subsystems are disabled and only critical thermal-control and housekeeping functions remain active, resulting in a minimal internal dissipation of approximately $Q^{\text{min}}_{\text{int}} = 160\,\text{W}$ (Sec. 21.1). Under these assumptions:

$$Q_{\text{IR}} + Q^{\text{min}}_{\text{int}} + Q_{\text{heat}} = \sigma\, \varepsilon_{\text{sc}}\, A_{\text{space}}\, (T^4_{\text{cold}} - T^4_{\text{space}})$$

With $Q_{\text{IR}} = 1095.3\,\text{W}$ (from Sec. 33) and neglecting heaters input, the resulting equilibrium temperature is $T^{\text{cold,op}}_{\text{sc}} \approx 244\ \text{K}$, well below the minimum allowable spacecraft temperature considered $T^{\text{min}}_{\text{sc}}$. Therefore, imposing the design cold-case temperature $T_{\text{design,cold}} = T^{\text{min}}_{\text{sc}} + 15\ \text{K} = 293\ \text{K}$, the requested heaters power can be computed as:

$$Q_{\text{heat}} = \sigma(\varepsilon_{\text{sc}}\, A_{\text{space}})(T^4_{\text{design,cold}} - T^4_{\text{space}}) - Q_{\text{IR}} - Q^{\text{min}}_{\text{int}} \approx 1319\ \text{W}$$

Applying ECSS 25 % margin: $Q^{\text{design}}_{\text{heat,op}} = 1.25 \times 1319 \approx 1648\ \text{W}$. Such a heaters demand is clearly incompatible with the available EPS budget, indicating that the global mono-nodal model is overly conservative for cold-case heater sizing. In practice, AKATSUKI adopts a zonal strategy wherein the most thermally sensitive components are individually insulated from the bus via MLI blankets, resulting in a significantly lower per-zone heater power requirement. Using $\varepsilon_{\text{eff}} \approx 0.03$ for 10-layer MLI and $\sim 0.1\ \text{m}^2$ zone areas [64], the per-zone heater power is $< 10\,\text{W}$, consistent with the EPS power budget (Sec. 21.1) (Sec. 1).

34 Adopted TCS Architecture: Passive and Active Control

Coatings and Surface Finishes. To maintain nominal Venus orbit bus temperature, the outer surfaces are covered with aluminized Kapton 5 mil [53]. The front face of each SAP has Anti-Reflection (AR) coatings and coverglass optical treatment to enhance PV efficiency and reduce solar absorptance [49]. Each SAP rear face is covered with OSRs, reducing the net heat absorbed from Venus and mitigating solar heating on the arrays and bus [38, 4]. Reversible radiator panels combined with OSR coatings enhance radiative heat rejection under varying thermal conditions.

Multi-Layer Insulation. MLI blankets are applied on internal components and instrument cavities to limit radiative exchange with the environment and to attenuate temperature transients during eclipse transitions [53]. Each blanket is composed of aluminized polyimide (e.g. Kapton®) films separated by Dacron®-net spacers; for a 10-layer 7361-Mystic Aluminized Kapton assembly the effective emittance is $\varepsilon_{\text{eff}} \approx 0.03$ [64]. MLI is applied on external bus surfaces, the IR2 housing, batteries, tank enclosures and propellant lines.

Radiators. Thermal rejection is achieved through RTPs, developed to accommodate the large thermal variation encountered throughout the mission [65, 66]. Unlike fixed radiators, which would either cause excessive heat losses in cold phases or insufficient heat rejection in hot conditions, RTPs passively adapt their radiative behavior according to temperature. In cold conditions the panel remains stowed, exposing a high-absorptivity / low-emissivity surface that limits radiative heat losses; at elevated temperatures the panel deploys, exposing a low-absorptivity / high-emissivity radiator surface to increase heat rejection across a total area of $\approx 5\,\text{m}^2$ [53]. Panel motion is driven by a Shape Memory Alloy (SMA)-based Reversible Rotary Actuator (RRA) and requires no dedicated electrical power. The RTPs provide radiative heat-rejection capability on the order of 100 W while significantly reducing the heater power that would otherwise be required by conventional fixed-radiators.

Electric Heaters. Electric heaters are the sole ATC elements required at the bus level. Three functional zones are individually controlled:

- **PS tanks & lines:** heaters prevent N_2H_4 and MON-3 freezing in all phases. 50 W during cruise; 118 W pre-VOI/VOI (all heaters + 20 W OME preconditioning); 22 W for station-keeping [P. 7].
- **Battery zone:** heaters maintain Li-ion packs above +10 °C during eclipse, since charging is inhibited below +10 °C. The zone is MLI-insulated; node-level heater power ~ 5 W [38].
- **Bus electronics:** ≈ 20.5 W distributed heaters on electronics units during during cold-case conditions [67].

35 Component-Level Thermal Control

35.1 IR2 Cryogenic Thermal Control

The IR2 detector requires active cryogenic cooling to remain $\leq 70\,\text{K}$[60]. This function is provided by a single-stage Stirling cryocooler consisting of a compressor, a cold head with a cold tip attached to the detector mount. The cold tip removes heat conductively from the detector and the extracted heat is rejected to space through a dedicated radiator plate on which the cryocooler assembly is mounted [60]. The heat-rejection path therefore is:

IR2 detector mount → cold head → compressor hot end → radiator plate → deep space

Assuming as a first-order sizing assumption the compressor hot-end temperature to be equal to the spacecraft hot-side design limit, $T_{\text{hot}} = T_{\text{sc}}^{\max} = 313$ K, the required radiator area can be estimated as:

$$A_{\text{cryo,rad,nom}} = \frac{Q_{\text{cooler}}}{\varepsilon_{\text{rad}}\,\sigma\,(T_{\text{hot}}^4 - T_{\text{space}}^4)} = \frac{50}{0.85 \times 5.67\times10^{-8} \times (313^4 - 3^4)} \approx 0.108\ \text{m}^2$$

35.2 Battery Thermal Control

The battery packs are wrapped in MLI to minimize heat exchange. The operational SoC imposes a constraint on temperature, due to charge inhibition below +10 °C [50]. Electric heaters (~ 5 W) maintain this temperature during OE. Modelling the battery zone as an MLI-isolated node of area $A_{\text{bat}} \approx 0.15\,\text{m}^2$ at $T_{\text{bat,min}} = +10\,°\text{C}$ ($= 283\,\text{K}$), with $\varepsilon_{\text{eff}} \approx 0.03$ [21, 64], the radiative loss to deep space is:

$$Q_{\text{loss,bat}} = \varepsilon_{\text{eff}}\,\sigma\,A_{\text{bat}}\,(T_{\text{bat}}^4 - T_{\text{space}}^4) = 0.03 \times 5.67\times10^{-8} \times 0.15 \times (283^4 - 3^4) \approx 1.64\ \text{W}$$

Adding a 25 % ECSS margin and accounting for battery self-discharge heat during eclipse (≈ 1 W [P. 21.1]), the required heater power is $Q_{\text{heat,bat}} \approx 1.8 \times 1.25 - 1.0 \approx 1.3\,\text{W}$, rounded conservatively to

$\sim 5\,\mathrm{W}$ to account for structural conduction losses. This value is well within the residual allocation [P. 21.1].

35.3 Propellant Tank and Thruster Line Thermal Control

As previously stated, temperature of tanks must be such to prevent propellant freezing. Catalyst-bed preheating of the RCS thrusters draws 10 W per 23-N thruster and 4 W per 3-N thruster (Sec. 1). The heater power budget per mission mode is directly traceable according to (Sec. 1):

- **Cruise (nominal):** 4×23-N at 10 W + 2×3-N at 4 W + 4 transducers at 0.5 W ≈ 50 W.
- **VOI:** all 8×23-N + all 4×3-N + OME preconditioning (20 W) + transducers ≈ 118 W.
- **Station-keeping:** 2×23-N + transducers ≈ 22 W.
- **Eclipse OE:** tank survival heaters only (≈ 22 W).

Tank heaters are thermostatically controlled via thermistor feedback loops, and are composed of Kapton-sandwiched flexible resistance elements bonded to tank and line walls (≈ 0.05 kg each) [21].

36 Electric Power for Active Control

AKATSUKI relies on dedicated active thermal-control devices for components whose temperature requirements cannot be satisfied through passive means alone [53].
Active thermal control is primarily applied to: [49, 5] (Sec. 1)

- **Scientific Payload**: Temperature stabilization and cooling of thermally sensitive detectors.
- **Propulsion Subsystem**: Catalyst-bed preheating and freeze protection of propellant tanks, lines and valves. Pressure transducer thermal regulation to maintain operational accuracy across all modes.
- **Batteries**: Temperature maintenance during cold-case conditions to preserve charging capability and battery performance.
- **Spacecraft Electronics**: Localized heating of avionics and power-conditioning units during low-temperature mission phases.

The principal active thermal-control devices and their associated power consumption are summarized in the following table. Note that IR2 cryocooler and LIR Peltier are active only during Science OA/OD modes, consistent with the ConOps defined in H1 (Sec. 1).

Component	Power [W]	Ref.
Scientific Payload		
IR2 Stirling cooler	50 W	[60]
LIR Peltier cooler	∼7 W (part of 29 W total for LIR)	[60]
Propulsion System *(assumption)*		
23-N RCS thruster heater (8)	10 W per heater	(Sec. 1)
3-N RCS thruster heater (4)	4 W per heater	(Sec. 1)
OME pre-heater	20 W	(Sec. 1)
Pressure transducer heater (4)	0.5 W per heater	(Sec. 1)
Spacecraft Bus		
Battery heaters	Included in 30 W safe-hold heater budget	[49] (Sec. 21.1)
Electronics heaters	∼20 W distributed heater power	(Sec. 1)

Table 52: Active thermal-control devices and associated power consumption adopted for AKATSUKI.

37 Physical Placement of TCS Elements

The placement of thermal-control elements is designed to maximize heat rejection toward deep space through minimized solar exposure of radiator surfaces and providing dedicated thermal regulation for critical components, while remaining compatible with spacecraft pointing constraints (see Tab. 53).

TCS Element	Location / Configuration	Thermal Function	Ref.
RTPs	$\pm Y$ faces, oriented toward deep space and away from direct solar illumination	Adaptive radiative heat rejection to deep space	[4, 35] [P. 21.1]
Optical Solar Reflectors (OSRs)	Rear side of the SAPs and radiator surfaces	Reduce net heat absorption from the environment	[49, 38]
Multi-Layer Insulation (MLI)	External spacecraft bus surfaces, batteries, propellant tanks and lines, and RTP internal interfaces	Reduce parasitic radiative heat transfer and attenuate thermal transients	[53] [P. 21.1]
SADA Thermal Off-Pointing	Solar-array orientation adjusted away from direct Sun incidence during Venus operations	Reduce solar heating with limited power-generation loss	[4] [P. 21.1)
IR2 Cryocooler	Mounted externally on the -Y face, with compressor and cold head elevated from the bus surface	Maintain detector operating temperature near -213 °C	[6]
LIR Thermoelectric Cooler	Integrated within the LIR detector assembly	Maintain detector temperature at $40 \pm 0.01°$C	[6]
Internal Heaters	Distributed throughout batteries, propulsion lines, tanks and selected electronics	Maintain minimum operational temperatures during cold cases	[38] [P.7.21.1]

Table 53: Physical placement and configuration of the principal thermal-control elements

38 Subsystem Budgets

The mass budget, defined in Tab. 54, considers a 20% design margin to account for thermal harnesses and miscellaneous integration hardware, treating them as Product Category D [20]. The difference in TCS mass is primarily due to a lack of literature on specific internal components. Specifically, the electric heater mass is significantly underestimated since it does not account for every heated element across the spacecraft. Passive element masses—such as MLI, OSRs, and radiators—are estimated by multiplying their assumed surface areas by typical areal densities. The MLI area was estimated from spacecraft imagery and external dimensions, assuming only a fraction of the total external area is insulated and including a margin to consider the coverage of sensitive internal elements [60].
Regarding the data budget, assuming ≈ 30 thermistor channels at 1 Hz with 16-bit resolution, the TCS data rate is $\dot{D}_{\text{TCS}} = 30 \times 1\text{ Hz} \times 16\text{ bit} = 480\text{ bps} \approx 0.5\text{ kbps}$, which is negligible with respect to the 32 kbps nominal downlink capacity (Sec. 3.8).
Finally, Tab. 55 presents the power budget per-mode throughout the report.

Component	Calculation	Mass [kg]	Source	Note
MLI blankets	$\rho_{\text{MLI}} \times S_{\text{lateral}} = 0.16\text{kg/m}^2 \times 9\text{m}^2$	1.44	[68]	«computed»
OSR panels on SAP rear faces	$\rho_{\text{OSR}} \times S_{\text{faces}} = 0.380\text{kg/m}^2 \times 2.96\text{m}^2$	1.12	[69]	«computed»
Radiators	–	0.69	[66]	«from literature»
IR2 Stirling cryocooler	–	10.4	[5]	«from literature»
Electric heaters	(assumption)	0.06	[70]	«from literature»
Harness and miscellaneous	MAR-MAS-020 (20 % of above)	2.74	[20]	«from literature»
Total TCS dry mass		**16.5**		«computed»
		18.0	[53]	«from literature»

Table 54: TCS mass budget.

Consumer	Safe Hold [W]	Cruise [W]	Pre-VOI [W]	Science OA/OD [W]	Source
IR2 Stirling cryocooler	0	0	0	50	[60]
LIR Peltier cooler	0	0	0	7	[60]
Tank/thruster heaters	22	50	118	22	(Sec. 1)
Battery-zone heaters	5	0	0	∼5	«computed»
Thermistor channels	0.3	0.3	0.3	0.3	[71]
TCS total	**27.3**	**50.3**	**118.3**	**84.3**	–

Table 55: TCS active power budget by mission mode «computed».

39 Configuration (CONF) and Structure Overview and Rationale

The spacecraft configuration is defined to accommodate the Payload (PL) and subsystems while satisfying mission and launch requirements. The Structure (STR) and Mechanism (MECH) subsystem must provide the physical interfaces and support required to realize the selected configuration [21] (Sec. 1). Due to the absence of detailed data, this report also relies on engineering assumptions drawn from authoritative sources. The architecture is selected according to the drivers summarized in Tab. 56.

Driver Description	Solution	Ref.
Fairing envelope compliance.	Foldable appendages for stowed launch configuration.	[8, 72]
Radiator needs: high solar flux.	Use of dedicated radiators.	[P. 30]
Ensure PL FoV correct alignment.	Payload (PL) located on the Venus-facing panel.	[72]
CoM control during propellant depletion.	Centrally located propellant tanks.	[8] [P. 7]

Table 56: Drivers for architectural shape selection

A box-and-panels CONF is chosen to maximize area for instruments and radiators [72] [P. 30], since the overall dry mass does not require a dedicated cylindrical shell to transfer the axial launch loads from the LV [53]. Finally, a truss architecture has an open skeletal framework, which is not the ideal because of the severe thermal environment at which the spacecraft is exposed near Venus [P. 30]. Tab. 57 outlines the spacecraft's architecture, defining three primary configuration levels.

Level	Components	Sizing Environment	Ref.
Primary structure	Bus sandwich panels; spacecraft interface ring; tank supporting enclosure.	Launch loads transfer (quasi-static, sine vibration); primary load path integrity.	[8, 73]
Secondary structure	Deployable SAPs; MLI support brackets; HGA mounting structure	Packaging & integration; random vibration and acoustic loads during ascent.	[21] [P. 3.8, 21.1, 30]
Tertiary structure	Camera hoods; harness routing clips	Dynamic behavior; resonance.	[P. 1-30]

Table 57: Primary configuration levels

Tab. 58 describes the main environmental drivers of the STR to consider during key mission operations.

Phase	Drivers and relative solutions	Ref.
Launch	Venting: prevent excess pressure and reduce time to evacuate the structure → fairing venting analysis to prevent overpressure damage; long./lat. accelerations and transients → high stiffness box-and-panels structure for LV loads.	[8, 74]
Operations	In-orbit operations. Severe thermal environment → thermal protections, low expansion materials for stability and precision mounts; micro-vibrations require structural stability of pointing PL → define maximum distortions and LOS pointing errors.	[75] [P. 14]
	Pointing requirements. Disturbance torques → symmetric bus design minimizes GG.	[75] [P. 14]

Table 58: Environmental drivers per mission phase

The selected launcher interface is the 1194M payload adapter, a standardized clamp-band ring mounted at the base of the bus [8]. The adapter transfers launch loads from the H-IIA to the primary structure and is released through a pyrotechnic clamp-band mechanism, generating a separation shock that represents a sizing driver for shock-sensitive components [8]. The interface ring is below the propellant tanks, ensuring that the spacecraft CoM remains within the axial boundary required by the launcher. The dynamic envelope accounts for structural deflections during ascent vibrations and constitutes the main constraint for external appendages. The SAPs must be stowed during launch to remain within this envelope, requiring dedicated hold-down and release mechanisms. A stay-out zone is imposed around the adapter to constrain the lower bus portion and prevent structural elements from occupying that region [76]. Tab. 59 summarizes the main structural loads associated with the launch environment.

Type	Value	Impact	Ref.
Quasi-static	6g-long./5g-lat.	Strength sizing of primary structure: panels must withstand peak accelerations with no permanent deformation.	[77]
Sinusoidal vibration	30–40 Hz 24.5 ms^{-2} long. 5–18 Hz 6.9 ms^{-2} lat.	Stiffness sizing of primary structure: bus first natural frequency must exceed a min. threshold to avoid resonance coupling with the LV.	[8]
Random vibration	0.032 g^2/Hz PSD peak	Fatigue sizing of secondary structure: vibrations are generated by first stage engines, boosters and pressure vibration, caused by buffeting and boundary layer noise during transonic flight and Max-Q.	[77]
Acoustic	141.5 dB OASPL	Sound reflects off the pad and excites the vehicle's structural panels; a second excitation occurs where aerodynamic boundary layer noise induces vibration and sound transmission to internal components.	[77]
Shock	4.1 g SRS peak	Separation: brittle failure/shock isolation for tertiary structure.	[8]

Table 59: H-IIA launch load environments and impact on AKATSUKI's structure [8]

40 Material selection for structural and configuration elements

The material selection is driven by the Venusian environment and the mass constraints of interplanetary launch. Rather than relying on heavy ATC, the architecture leverages passive heat rejection, while keeping high-specific-stiffness materials. Tab. 60 synthesizes these choices, illustrating how the subsystems were optimized to ensure dimensional stability, efficient load transfer, and survivability.

Element	Material / Technology	CONF/STR Function	Rationale	Ref.
Primary structure and load path	Central thrust/load path with Al honeycomb core and CFRP skins; Al honeycomb box panels.	Transfers launch and OME loads to the interface accommodates PL and subsystems.	High stiffness-to-mass ratio, low mass and dimensional stability.	[73] [35] [52]
External bus surfaces	Aluminized MLI, radiative coatings, OSRs, and RTPs.	Thermal insulation, and radiative heat rejection from selected faces.	Controls thermal loads in-orbit without requiring ATC.	[53][38] [4]
SAPs	0.15 mm 3J InGaP/GaAs/Ge cells, with CMG cover glass, AR coating, and OSR on the rear side.	Primary electrical power source and contribution to thermal-load control on the panels.	High conversion efficiency, radiation tolerance, and better high-temperature performance than Si.	[38]
SAPs substrate	Sandwich substrate with 10 mm Al honeycomb core, CFRP face sheets, and Kapton films.	Structural support for SAPs; maintains solar-cell alignment during all mission phases.	High specific stiffness; substrate thermal conduction toward the OSRs supports heat rejection.	[49]
HGAs	Flat slot-array antennas on quartz honeycomb plate, laminated with Cu films; Ti-alloy brackets.	Provides high-gain X-band UL/DL capability.	The flat geometry avoids focal-point solar heating associated, reducing mass and thermal risk.	[27] [32]
Propellant tanks	Spherical Ti-6Al-4V tanks for N_2H_4, MON-3, and GHe.	Stores and pressurizes propellants and pressurant inside the PS.	High strength-to-density ratio and pressure-efficient geometry.	(Sec. 1)
OME chamber	Monolithic Si_3N_4 ceramic (SN282, gas-pressure-sintered).	Acts as the high-temperature OME combustion chamber.	High thermal and oxidation resistance; requires less film cooling than coated metallic chambers.	[35] [78]

Table 60: Material selection for structural and configuration elements

41 Mechanism utilization and positioning

The design limits moving parts to functions for which mechanical articulation is strictly required, reducing mass, complexity, and potential failure points. Mechanically decoupling selected appendages from the bus provides operational flexibility by meeting subsystem-specific pointing requirements without constraining the attitude. Tab. 61 enlists function and rationale for the mechanisms utilization.

Mechanism	Function	CONF rationale	Ref.
SAP hold-down/release	Locking in stowed configuration and release after separation	Reduces the number of holding devices: a single system locks both folded paddles.	[49]
SADA	1-dof Sun tracking + off-pointing	Decouples bus pointing from panel pointing.	[4]
RWs	Nominal attitude control	4×RWs to maintain three-axis control and redundancy.	[53, 4]
MGA on single-axis turntable	TLM and telecommand when the HGA is not aligned	Increases robustness in safe/degraded mode with lower complexity than an HGA mechanism.	[53]

Table 61: Mechanism CONF × Function × Rationale summary.

42 External elements positioning

SAPs. SAP1 and SAP2 on the ±Y faces and can rotate about the Y axis through dedicated SADAs. The lateral placement of the SAPs prevents interference with the PL FoV and allows independent Sun tracking, enabling simultaneous power generation and Venus observations. The symmetric placement reduces SRP induced torques and dynamic imbalance during spacecraft rotations [72, 79].

HGA & LGA. XHGA-T/R and XLGA-A/B rigidly on the spacecraft $+Z$ face, providing an unobstructed FoV and creating a communication deck separated from both the PL and PS. This reduces geometric conflicts between different functions and minimizes risk of plume impingement during OME firings. XLGA-A and XLGA-B on the $+X$ and $-X$ faces, respectively. Their opposite-side placement reduces the probability of simultaneous visibility loss due to spacecraft orientation [72, 79].

MGA. The XMGA-A/B on the spacecraft $+Y$ face on single-axis gimbals aligned with the $+Y$ axis. The $0° \div 180°$ gimbal angle provides pointing flexibility without requiring attitude maneuvers. At zero gimbal angle, the boresight of XMGA-A and XMGA-B are aligned with $-X$ and $+X$, respectively. This mirrored configuration allows the communication coverage provided by one antenna to complement that of the other, extending the overall Earth-pointing capability [79].

PL instruments. IR1, IR2, UVI and LIR on the $-X$ panel, whereas LAC on the $+Y$ panel, close to the interface with the $-X$ side, due to accommodation constraints. This arrangement establishes the $-X$ face as the observation deck, preventing conflicts between science observations and other spacecraft activities. This also simplifies harness routing and PL integration, since power and data connections can be grouped within the same spacecraft region. Scientific instruments boresights are aligned with $-X$ direction. Co-aligned optical axes enable simultaneous observations of the same atmospheric region and allow a single attitude-control solution to satisfy the pointing requirements of the entire PL, eliminating the need for dedicated payload-pointing mechanisms [79].

OME. The OME nozzle on the $-Z$ face, with its longitudinal axis passing through the spacecraft CoM in order to minimize parasitic torques during burns [72].

RCS. The thrusters are mounted at the bus corners. This arrangement maximizes the lever arm relative to the CoM, improving attitude-control authority and momentum unloading efficiency while limiting plume interaction with the spacecraft structure [72].

Attitude Determination Sensors. SPS-A and SPS-B on the outer edges of SAP-1 and SAP-2, respectively. CSAS-A and CSAS-D on the $+Z$ face, while CSAS-E on the $+X$ face. FSS-Y and FSS-Z on the $+X$ panel, oriented to measure the Sun direction relatively to the Y- and Z-axes, respectively. STT-A and STT-B on the $-Y$-facing side of a dedicated external support structure extending from the bus edge between the $+Y$ and $-Y$ faces. The sensor layout is driven by FoV availability and redundancy requirements. The STTs are positioned to ensure an unobstructed view of deep space and minimize stray-light contamination. The distributed placement of CSAS, FSS and SPS units guarantees Sun observability over a wide angular range, preventing simultaneous blinding of all Sun sensors [79].

43 Internal Elements Distribution

The internal layout is driven by CoM control, thermal management, and subsystem integration considerations, ensuring efficient interfaces between structural, propulsion, power, and thermal elements.

43.1 Center-of-Mass Balancing

The payload adapter constrains the CoM within a ± 25 mm radial offset from the LV axis [8]. Given the large propellant fraction ($\approx 38\%$ of wet mass), CoM migration is controlled through tank placement.

Propellant tank placement. All tanks are located near the spacecraft $\pm Z$ symmetry axis, ensuring that propellant depletion mainly produces axial rather than radial CoM shifts. Spherical tanks allow compact packing in a central column consistent with the box-and-panels structural envelope [73] [P. 7].

OME thrust vector alignment. The thrust vector passes through the CoM. To keep an angular misalignment at ignition $\leq 0.5°$ Absolute Performance Error (APE), the engine is fixed to the primary structure, accepting the associated minor cosine loss in exchange for reduced mechanical complexity.

RWs symmetry. The RWs are arranged symmetrically within the bus, close to the CoM. This configuration minimizes inertia asymmetry and supports attitude-control performance (Sec. 14).

43.2 Internal Thermal Dissipation

The internal layout must support efficient heat transport from dissipative equipment to radiating surfaces, while maintaining temperature-sensitive components within their allowable temperatures.

Primary thermal bus. The primary structure is the main conductive path [73, 52]. Internal electronics panels are bolted to it, allowing waste heat to be conducted efficiently toward the radiators. This passive architecture requires no heat pipes for the DE, reducing mass and failure risk.

IR2 Stirling cryocooler. IR2 requires cryogenic operation at 65 K. This is achieved through a Stirling cryocooler, whose compressor and cold head are accommodated on a cold plate exposed to space. This arrangement enables direct heat rejection minimizing internal heat transfer [5] (Sec. 30).

LIR cooler. The LIR bolometer must be stabilized at 313 K (Sec. 30). This is achieved with a Peltier cooler, embedded within the sensor head. The low power demand makes it the simplest solution [21].

Battery thermal management. The battery pack is mounted on an internal structural panel adjacent to the PCDU, to simplify power distribution and thermal control.

Heater network. Kapton heaters are mounted near the bus temperature-sensitive components [P. 30].

44 Structure Subsystem Mass

This section estimates the core structural mass (i.e. primary load path, structural panels, launcher interface, and supports), excluding items allocated to other subsystems. A two-step approach is used: (i) sizing an equivalent primary load path; (ii) comparing it to a parametric dry-mass estimate [21, 80].

Input data and mass convention. Launch loads are evaluated using the wet mass; the parametric subsystem fractions are referred to the dry mass. The required inputs are summarized in Tab. 62 [5].

Quantity	Value	Purpose	Ref.
m_{wet}	517.9 kg	Wet mass used for launch load evaluation; includes propellant	[12]
m_{prop}	196.7 kg	Propellant mass subtracted to derive dry mass	[12]
L	1.40 m	Equivalent height along the launcher/OME axis	[72]
R	0.89 m	Radius of circumscribed cylinder to the 1.04×1.45 m cross-section	«computed»
$f_{\mathrm{lat}},\ f_{\mathrm{ax}}$	≥ 10 Hz, ≥ 30 Hz	H-IIA minimum frequency requirements to avoid dynamic coupling	[8]
$LF_{\mathrm{ax}},\ LF_{\mathrm{lat}}$	$6g,\ 5g$	Quasi-static envelope for axial compression and bending at launch	[8]

Table 62: Input parameters for the structural mass estimate.

Equivalent monocoque sizing of the primary load path. The primary load path is modeled as a thin-walled cylinder aligned with the LV axis. Preliminary sizing assumes equivalent lightweight CFRP/Al properties: $E = 70\,\mathrm{GPa}$, $\rho = 1600\,\mathrm{kg\,m^{-3}}$, $\sigma_u = 600\,\mathrm{MPa}$, $FS_{\mathrm{ult}} = 1.25$. These values are representative assumptions used for preliminary sizing.

Stiffness. Natural frequencies estimated via beam-like coefficients, for the H-IIA LV ($f_{\mathrm{ax}} \geq 30\,\mathrm{Hz}$, $f_{\mathrm{lat}} \geq 10\,\mathrm{Hz}$) require $A_{\mathrm{req}} = 1.49 \times 10^{-4}\,\mathrm{m^2}$ and $I_{\mathrm{req}} = 6.47 \times 10^{-6}\,\mathrm{m^4}$. Stiffness is therefore not the sizing driver, since $t_{\mathrm{ax}} = 0.027\,\mathrm{mm}, t_{\mathrm{lat}} = 0.003\,\mathrm{mm}$ for a thin circular shell [21].

Loads, strength and buckling. Assuming the lateral resultant applied at $L/2$, the maximum axial load and base bending moment are $L_{\mathrm{ax}} = m_{\mathrm{wet}}\, g\, LF_{\mathrm{ax}} = 30.5\,\mathrm{kN}$ and $M_B = 0.5 m_{\mathrm{wet}}\, g\, L^2 F_{\mathrm{lat}} = 17.8\,\mathrm{kN\,m}$. Consequently, the equivalent axial and the ultimate design loads are $L_{\mathrm{eq}} = L_{\mathrm{ax}} + (2M_B)/R = 70.3\,\mathrm{kN}$ and $L_U = L_{\mathrm{eq}}\, FS_{\mathrm{ult}} = 87.9\,\mathrm{kN}$. The average compressive stress check, $\sigma = \frac{L_U}{2\pi R t} \leq \sigma_u$, gives $t_\sigma = 0.026\,\mathrm{mm}$. The governing condition is global shell buckling. Following the tabulated procedure [21], the critical buckling stress and load are $\sigma_{\mathrm{cr}} = 0.6\,\gamma\, E\, t R^{-1}$ and $L_{\mathrm{cr}} = 2\pi R\, t\, \sigma_{\mathrm{cr}} \geq L_U$. Iterating on t yields $t_{\mathrm{buckling}} = 1.14\,\mathrm{mm}$ (knockdown factor $\gamma = 0.3$); $t = 1.20\,\mathrm{mm}$ is adopted, providing a positive margin. The mass of the equivalent load-bearing shell is $m_{\mathrm{shell}} = \rho \cdot 2\pi R\, t\, L \approx 15\,\mathrm{kg}$. This represents the equivalent primary load path only; it should be regarded as a lower bound for the complete STR.

Complete structural mass and adopted value. A parametric estimate based on dry mass fractions yields a nominal structural mass of approximately 67 kg. The difference with respect to the monocoque result reflects the broader scope of the parametric model, which includes the complete STR subsystem rather than only the primary load path.

45 On-Board Data Handling (OBDH) Architecture

45.1 Architecture classification

Based on the available AKATSUKI documentation, the OBDH subsystem architecture can be reasonably inferred to consist of a On-Board Computer (OBC) complemented by local PL controllers [4]. The main OBC acts as the master node, centrally managing HK acquisition, telecommand execution, Fault Detection, Isolation, and Recovery (FDIR) functions, and scientific-data management [81]. Each PL incorporates dedicated DE units responsible for local image acquisition, processing, compression, buffering, and packetization [4]. However, these units do not possess autonomous spacecraft-control authority; all mission-management and decision-making functions remain centralized within the OBC. The resulting OBDH architecture can therefore be classified as a centralized system enhanced by local PL controllers rather than a fully distributed or federated architecture. The key elements of the OBDH are described in Tab. 63.

Element	**Primary function**	**Ref.**
Main OBC	Spacecraft supervision, FDIR, telecommand execution, TLM formatting.	[81]
Sensor DE	Image acquisition, onboard compression (HIREW), data packetization for PL bus	[4]
ADCS Electronics	Local AOCS loop (STT, IRU, RW); outputs attitude state to OBC	[82]
TT&C Unit	RF telecommand decoding, TLM encoding, transponder control	[83, 84]

Table 63: Processing distribution within the OBDH

45.2 Redundancy

Based on JAXA's previous missions and the interplanetary mission profile, a cold-redundant configuration is a plausible assumption: a primary and a backup OBC that remains de-powered during nominal operations and is activated by ground command or watchdog upon primary failure [21, 85, 86]. The advantages are full backup capability, and the reduction of power draw and component aging. Hardware redundancy is extended to memories and TT&C interfaces; software redundancy is implemented through watchdog timers and FDIR procedures [21, 86].

46 OBDH Components and Performance

46.1 On-Board Computer

Based on the development period of AKATSUKI (2001–2008) and the processor technologies commonly adopted in contemporary deep-space missions, a RAD750 processor is assumed as a plausible OBC solution for sizing purposes [87, 88, 89]. The estimated characteristics are summarized in Tab. 64.

Parameter	**Assumed value**	**Ref.**
Processor architecture	32-bit	[88]
Clock frequency	33 MHz	[88]
Computing performance	300 MIPS	[88]
Radiation tolerance	200 krad	[87, 88]

Table 64: Characteristics of the RAD750 processor

46.2 Memory architecture

The memory architecture follows the standard three-level configuration:

- **Non-volatile boot memory (EEPROM/PROM, ≈ 8 MB):** stores boot software, safe-mode contingency routines, and mission parameters [90].
- **Working RAM (SDRAM, ≈ 8 MB):** used for software execution, telemetry buffers, and temporary attitude-control variables [63].
- **Mass memory – 512 MB Solid State Recorder (SSR):** integrated in the sensor DE; stores science images and platform HK before DL [60, 91].

47 Selected Buses According to Data Management Needs

OBDH architecture avoids burdening the platform processor with high-volume science data and ensures that instrument management does not contend with safety-critical buses operations [21].

Platform HK bus (DH unit ↔ subsystems). The platform bus carries HK telemetry from all platform subsystems to the DH and distributes telecommands in return. The total platform HK data rate established in the data budget is ≈ 2820 bps, broken down as: ADCS 1296 bps, TCS 480 bps, EPS 739.2 bps, PS 152 bps, TMTC 56.8 bps, and OBDH/DE 96 bps (Secs. Sections 2, 3.8, 14, 21.1 and 30). This aggregate rate is negligible compared to a standard MIL-STD-1553B platform bus (1 Mbps), confirming that a single shared bus is sufficient to service all platform subsystems without bandwidth contention [21].

Science data path (PL → OBC). Science data flow from the instruments to the DE, which performs onboard arithmetic processing, lossless compression, and packetization before writing to the solid-state recorder [4, 92]. For one nominal 30-hour science revolution, the raw science volume (226 MB, 130 images) is reduced to 55 MB after compression and the observation-time factor, yielding $V_{\text{science}} = 440$ Mbit stored per revolution [4, 93]. Instruments are commanded and read by the DE sequentially in ~2 h observation cycles [4]; IR1 produces images of ~2 MB at 14-bit resolution [60], and the resulting per-instrument data transfer rate is low relative to the DE's internal bandwidth [94].

OBC → TT&C downlink path. The DH unit formats CCSDS-compliant TLM packets, mixing science and HK data, and transfers them to the X-TRP for DL. The achievable DL rate over the X-band HGA is 8–32 kbps, adaptive to the Venus–Earth distance, and UL command rate via the HGA is 1 kbps . The interface between the DH unit and the X-TRP is a low-rate serial line, since even the maximum 32 kbps science DL is orders of magnitude below the internal bus bandwidth [2, 35].

The architecture confirms that no bus is capacity-constrained in the nominal science phase. The binding constraint is due to the ground DL rate, which makes onboard compression and selective data prioritization a necessary design features [4] (Sec. 3.8).

47.1 Intra-Satellite Data Management Rationale

The OBDH architecture can be reconstructed by analyzing the data exchanged among subsystems and the corresponding communication requirements. The objective is to identify the most demanding internal data flows and the communication buses capable of supporting the required data rates while ensuring reliable operations.

Scientific observations dominate the onboard data budget and constitute the primary driver for the data-handling architecture. Conversely, platform subsystems such as ADCS, EPS, TCS, PS and TT&C mainly exchange HK telemetry, status information and commands, generating significantly lower data volumes. Table 65 summarizes the main internal data flows and their communication requirements.

Communication Path	Data Type	Main Requirement
Payload → OBC	Scientific images and measurements	Throughput
AOCS ↔ OBC	Attitude telemetry and control commands	Determinism + Reliability
EPS ↔ OBC	Power subsystem telemetry and commands	Reliability
TCS ↔ OBC	Thermal telemetry and heater commands	Reliability
PS ↔ OBC	Propulsion telemetry and actuator commands	Reliability + Determinism
TT&C ↔ OBC	Telecommands and telemetry packets	Reliability

Table 65: Main internal spacecraft data flows and communication requirements.

Throughput refers to the amount of data transferred per unit time. High-throughput interfaces are required to prevent bottlenecks in the transfer of science data from the instruments to the OBC, as it becomes the dominant requirement when large datasets are exchanged [95].

Reliability refers to the ability of a communication link to transfer data correctly, minimizing the probability of errors or data loss, that may compromise spacecraft operations [96].

Determinism refers to the predictability of communication timing. A deterministic bus guarantees

that messages are delivered within known and bounded time intervals. This requirement is especially important for attitude-control functions, where control algorithms rely on timely and predictable exchanges of sensor measurements and actuator commands [97].
The table highlights the existence of two distinct classes of onboard traffic: **PL traffic**, characterized by large data volumes and throughput-driven requirements; and **platform traffic**, characterized by low data volume but requiring highly reliable and deterministic communication.

47.2 Bus Selection Rationale

Considering the PL-to-OBC high-demand internal communication paths, the assumed OBDH architecture is coherent with the use of dedicated PL controllers (See Sec. 45). Separating PL traffic from platform traffic prevents image transfers from saturating the spacecraft command-and-control network and allows science operations to be performed independently from HK activities.
Conversely, the links connecting the subsystems to the OBC exchange relatively small amounts of data. For these subsystems, communication reliability and deterministic behaviour are more important than throughput. A redundant command-and-response bus such as MIL-STD-1553B therefore represents a suitable solution. Its throughput is largely sufficient for HK telemetry and telecommands while providing the robustness and fault tolerance typically required by interplanetary missions [98].

47.3 OBC-TT&C Interface

The OBC/TT&C interface represents the path through which stored scientific data are transmitted to Earth. Since scientific observations are acquired continuously throughout the orbit whereas DL opportunities are limited to dedicated communication windows, direct real-time transmission of all acquired data is generally not feasible. Consequently, the OBDH subsystem must temporarily store PL data before transmission, adopting a store-and-forward data-management approach.
The reconstructed onboard memory capacity provides a useful consistency check for this architecture. Comparing the available 512 MB solid-state memory with the estimated compressed science-data volume per orbit yields a storage margin of about 457 MB [60, 91]. Such a margin can accommodate HK telemetry, communication outages (e.g. loss of a scheduled downlink session) and operational contingencies (e.g. safe-mode operations or additional diagnostic TLM following an anomaly).

48 Data Budget and Storage Sizing

48.1 Approach and interval

The analysis covers a 30-hour nominal science revolution, storing processed science and continuous platform HK data before DL. Event-based parameters are excluded. The data rate per parameter is $D_i = n_i\, b_i\, f_i$ (bps), yielding a per-revolution volume of $V_i = D_i \times 108\,000/10^6$ (Mbit).

48.2 Science payload volume

For one nominal 30-hour revolution, the AKATSUKI observation planning estimates 226 MB of raw science data, reduced to 75 MB after onboard compression; applying an observation-time factor of 3/4 to account for non-imaging periods yields a net science data volume of 55 MB per revolution [93].

48.3 Platform housekeeping data budget

Lacking a public AKATSUKI telemetry list, the HK budget is estimated at the subsystem level using only essential health and status parameters. Analogue values are modeled as 16-bit words and discrete states as 8-bit words. Sampling frequencies match physical behavior: 0.1 to 1 Hz for slow variables and 1 to 10 Hz for fast attitude data. This yields a system-level volume estimate without requiring detailed packet formats.
Storage conclusion: Even applying a conservative +400% margin, the required 3722.85 Mbit (465.36 MB) fits within the 512 MB (4096 Mbit) DE recorder capacity [60], utilizing 90.9% of the solid-state recorder. The binding operational constraint is therefore DL, not storage: at 32 kbps over a 6-hour window, the dumpable volume is 691 Mbit (86 MB), which is lower than the total volume generated during a science revolution. Consequently, data prioritization is an essential operational feature.

B Data Budget Breakdown – Nominal 30-hour Science Revolution

Method: $D_i = n_i \times b_i \times f_i$ *bps;* $V_i = D_i \times 108\,000/10^6$ *Mbit. Interval:* $t = 30\,h = 108\,000\,s$ *[93]. Margin:* +400%.

Subs.	Parameter	n	Type	bits	f [Hz]	R [bps]	V [Mbit]	Ref.
EPS	PCDU temperature	2	sint16	16	0.5	16	1.73	«computed»
	Battery temperature	2	sint16	16	0.5	16	1.73	«computed»
	Battery current	1	sint16	16	1.0	16	1.73	«computed»
	Battery voltage	2	sint16	16	1.0	32	3.46	«computed»
	Bus voltage	1	sint16	16	1.0	16	1.73	«computed»
	Solar-array current	20	sint16	16	1.0	320	34.56	[49]
	MPPT voltage	20	sint16	16	1.0	320	34.56	«computed»
	SADA angle	2	sint16	16	0.1	3.2	0.35	«computed»
EPS subtotal							**79.85**	
TCS	Thermistor channels (30)	30	sint16	16	1.0	480	51.84	[60] (Sec. 30)
TCS subtotal							**51.84**	
ADCS	RW tachometer data	4	sint16	16	2	128	13.82	«computed»
	RW motor current	4	sint16	16	1	64	6.91	«computed»
	STT quaternion	4	float32	32	5	640	69.12	«computed»
	Gyro output	3	float32	32	2	192	20.74	[99]
	Sun sensors output	7	sint16	16	2	224	24.19	«computed»
	IMU current	1	sint16	16	1	16	1.73	«computed»
	IMU voltage	1	sint16	16	1	16	1.73	«computed»
	IMU temperature	1	sint16	16	1	16	1.73	«computed»
	Mode / status flags	–	–	–	ev.	–	event-based	–
ADCS subtotal							**139.97**	
PS	Tank pressure sensors	3	sint16	16	0.5	24	2.59	[35]
	Tank temperature sensors	3	sint16	16	0.5	24	2.59	[35]
	Thruster temperatures	13	sint16	16	0.5	104	11.23	[35]
	Valve / thruster status	–	–	–	ev.	–	event-based	–
PS subtotal							**16.41**	
OBDH	OBC health (T, V, I, packet count)	4	sint16	16	1.0	64	6.91	«computed»
	Boot cause, watchdog, mode flags	4	uint8	8	1.0	32	3.46	«computed»
OBDH subtotal							**10.37**	
TMTC	Transponder temperature	1	sint16	16	0.5	8	0.86	«computed»
	Packet counters	2	sint16	16	1	32	3.46	«computed»
	RF output power	1	sint16	16	0.5	8	0.86	«computed»
	Lock flags	1	uint8	8	1	8	0.86	«computed»
	Active antenna ID	1	uint8	8	0.1	0.8	0.09	«computed»
TMTC subtotal							**6.13**	
Platform HK total							**304.57**	
Science payload						—	**440**	[93]
Grand total (nominal, no margin)							**744.57** (93.07 MB)	
With +100% margin (×2)							**1489.14** (186.14 MB)	«computed»
With +400% margin (×5)							**3722.85** (465.36 MB)	«computed»
Installed SSR capacity							**4096.00** (512 MB)	[60]
Filling – nominal							744.57/4096 = 18.2%	
Filling – with +400% margin							3722.85/4096 = 90.9%	

Table 66: OBDH data budget – nominal 30-hour science revolution.

3 Mass Budget

Two subsystem mass breakdowns are reported below: Tab. 67 compiles masses found in the literature for AKATSUKI, while Tab. 68 compiles the masses obtained from this team's own sizing activity across Assignments #1–#8. Design-maturity margins follow the ESA CDF Standard Margin Philosophy [20].

Subsystem	**Mass [kg]**	Ref.
Payload (PL)		
Ultraviolet Imager (UVI)	3.40	[60]
Longwave Infrared Camera (LIR)	3.70	[60]
1-µm Camera (IR1)	6.00	[60]
2-µm Camera (IR2)	9.00	[60]
Lightning and Airglow Camera (LAC)	1.50	[60]
Subtotal	23.60	
Propulsion System (PS)		
Orbital Maneuvering Engine (OME)	–	
Reaction Control System (RCS)	–	
MON-3 tank	–	
N_2H_4 tank	–	
He pressurant tank	–	
Plumbing, valves, lines	–	
Subtotal	64.00	[53]
Telemetry, Tracking, and Telecommand (TTMTC)		
High-Gain Antenna (HGA)	4.00	[100]
Medium-Gain Antenna (MGA)	–	
Low-Gain Antenna (LGA)	–	
X-band Digital Transponder (X-TRP)	–	
Travelling-Wave Tube Amplifier (TWTA)	–	
Solid-State Power Amplifier (SSPA)	–	
Ultra-Stable Oscillator (USO)	1.90	[33]
Subtotal	27.30	[27]
Attitude Determination and Control System (ADCS)		
Star Tracker (STT)	18.00	[35]
Fine Sun Sensor (FSS)	2.60	[35]
Inertial Reference Unit (IRU)	2.15	[35]
Coarse Sun Sensor (CSS)	0.20	[35]
Sun Presence Sensor (SPS)	0.16	[35]
Accelerometer (ACM)	0.09	[35]
Reaction Wheels (RWs)	13.20	[35]
Attitude and Orbit Control Unit (AOCU)	10.80	[35]
Driving Unit (DRV)	7.00	[35]
Subtotal	54.20	
Electrical Power Subsystem (EPS)		
Solar Array Paddle (SAP)	15.28	[49]
Solar Array Drive Assembly (SADA)	–	
Battery packs	–	
Power Control Unit (PCU)	–	

Continued on next page

Table 67 – continued from previous page

Subsystem	**Mass [kg]**	Ref.
Harness	–	
Subtotal	42.00	[53]
Thermal Control Subsystem (TCS)		
MLI blankets	–	
OSR panels	–	
Radiators	–	
IR2 Stirling cryocooler	10.40	[5]
Electric heaters	–	
Harness and miscellaneous	–	
Subtotal	18.00	[53]
Structure (STR)	88.00	[53]
On-Board Data Handling (OBDH)	10.00	[53]
Total dry mass (w/o adapter)	**327.10**	
System margin (w/o adapter)	20	[20]
Total dry mass w/ margin (w/o adapter)	**392.52**	
Propellant	196.70	[12]
Total wet mass (w/o adapter)	**589.22**	
Adapter mass	100.00	[8]
Total launch mass (w/ adapter)	**689.22**	
Maximum launchable mass margin	10	[101]
Maximum launchable mass	**758.14**	

Table 67: Subsystem mass breakdown of AKATSUKI from literature data

Subsystem (Dry mass contribution)	**Mass w/o margin [kg]**	**Margin [%]**	**Mass w/ margin [kg]**	Ref.
Payload (PL)				
Ultraviolet Imager (UVI)	3.40	20.00	4.08	[60]
Longwave Infrared Camera (LIR)	3.70	20.00	4.44	[60]
1-μm Camera (IR1)	6.00	20.00	7.20	[60]
2-μm Camera (IR2)	9.00	20.00	10.80	[60]
Lightning and Airglow Camera (LAC)	1.50	20.00	1.80	[60]
Subtotal	**23.60**		**28.32**	
Propulsion System (PS)				
Orbital Maneuvering Engine (OME)	3.00	10.00	3.30	[22]
Reaction Control System (RCS)	48.00	5.00	50.40	[21]
MON-3 tank	1.01	5.00	1.06	«computed»
N_2H_4 tank	1.23	5.00	1.29	«computed»
He pressurant tank	2.92	5.00	3.07	«computed»
Plumbing, valves, lines (15.00% of tank masses)	0.77		0.81	[21]
Subtotal	**56.93**		**59.93**	

Continued on next page

Table 68 – continued from previous page

Subsystem (Dry mass contribution)	**Mass w/o margin [kg]**	**Margin [%]**	**Mass w/ margin [kg]**	Ref.
Telemetry, Tracking, and Telecommand (TTMTC)				
High-Gain Antenna (HGA)	4.00	20.00	4.80	[100]
Medium-Gain Antenna (MGA)	–	–	–	
Low-Gain Antenna (LGA)	–	–	–	
X-band Digital Transponder (X-TRP)	–	–	–	
Travelling-Wave Tube Amplifier (TWTA)	–	–	–	
Solid-State Power Amplifier (SSPA)	–	–	–	
Ultra-Stable Oscillator (USO)	1.90	5.00	2.00	[33]
Subtotal	**27.30**	10.00	**30.03**	[27]
Attitude Determination and Control System (ADCS)				
Star Tracker (STT)	18.00	5.00	18.90	[35]
Fine Sun Sensor (FSS)	2.60	5.00	2.73	[35]
Inertial Reference Unit (IRU)	2.15	5.00	2.26	[35]
Coarse Sun Sensor (CSS)	0.20	5.00	0.21	[35]
Sun Presence Sensor (SPS)	0.16	10.00	0.18	[35]
Accelerometer (ACM)	0.09	10.00	0.10	[35]
Reaction Wheels (RWs)	13.20	5.00	13.86	[35]
Attitude and Orbit Control Unit (AOCU)	10.80	20.00	12.96	[35]
Driving Unit (DRV)	7.00	20.00	8.40	[35]
Subtotal	**54.20**		**59.60**	
Electrical Power Subsystem (EPS)				
Solar Array Paddle (SAP)	15.28	20.00	18.34	[49]
Solar Array Drive Assembly (SADA)	2.00	5.00	2.10	[21]
Battery packs	13.60	20.00	16.32	«computed»
Power Control Unit (PCU)	5.00	5.00	5.25	«estimated»
Harness (10.00% of above)	3.59		4.20	[21]
Subtotal	**39.47**		**46.21**	
Thermal Control Subsystem (TCS)				
MLI blankets	1.44	5.00	1.51	[68]
OSR panels	1.12	5.00	1.18	[69]
Radiators	0.69	5.00	0.72	[66]
IR2 Stirling cryocooler	10.40	5.00	10.92	[5]
Electric heaters	0.06	10.00	0.07	[70]
Harness and miscellaneous (20.00 % of above)	2.74		2.88	[20]
Subtotal	**16.45**		**17.28**	
Structure (STR)	88.00	5.00	92.40	[53]
On-Board Data Handling (OBDH)	10.00	5.00	10.50	[53]
Total dry mass (w/o adapter)	**315.95**		**344.27**	
System margin (w/o adapter)		20.00		[20]
Total dry mass w/ margin (w/o adapter)			**413.12**	

Continued on next page

Table 68 – continued from previous page

Subsystem (Dry mass contribution)	**Mass w/o margin [kg]**	**Margin [%]**	**Mass w/ margin [kg]**	Ref.
Propellant	196.70	2.00	200.63	[12]
Total wet mass (w/o adapter)			**613.75**	
Adapter mass	100.00	0.00	100.00	[8]
Total launch mass (w/ adapter)	**713.75**	5.00	**749.44**	
Maximum launchable mass margin		10		[101]
Maximum launchable mass			**824.38**	

Table 68: Subsystem mass breakdown from the team's own sizing activity

The two reconstructed mass budgets exhibit a substantial discrepancy with respect to the actual flight mass of approximately 500 kg [102]. The literature-based budget (Tab. 67) yields a total launch mass of 689.22 kg, while the own-sizing budget (Tab. 68) results in 713.75 kg before the launch margin and 749.44 kg after it — both values exceeding the real spacecraft mass by a wide margin. This overestimation is attributable to three compounding factors rather than modelling errors.

Firstly, several subsystem masses could not be reconstructed from the available literature, as reflected in the incomplete entries of both tables. In these cases, only aggregate subsystem masses were available from reference documents that do not provide a component-level breakdown [27, 53]. Such values tend to be more conservative than a bottom-up, component-by-component estimate. An additional similar source of uncertainty affects the own-sizing budget: where neither specific data nor an original sizing calculation were available, component masses were estimated from representative values reported in the broader technical and engineering literature — including comparable subsystems from other missions and standard references — deemed appropriate for the expected mass range for this class of spacecraft. While necessary to complete the breakdown, this introduces an additional layer of approximation with respect to the AKATSUKI-specific published values, thereby contributing to the overall conservative bias of the reconstructed mass budget. For the TTMTC subsystem, where component-level masses for several units could not be inferred through the reverse-sizing process, the corresponding aggregate value reported in the reference documents was retained as the most reliable available estimate, consistent with the conservative approach adopted throughout this mass budget.
Secondly, the design-maturity margins applied at component, subsystem, and system levels are cumulative: a component already carrying a 5–20% margin is further inflated by the 20% system-level margin on dry mass and subsequently by the propellant and launch margins, resulting in an overall multiplicative effect rather than a simple additive one.
Thirdly, since AKATSUKI was an operational, flight-proven spacecraft, its actual flight mass reflects the efficiencies achieved during the mature design phase (structural optimization, harness routing, integration savings) that a Phase 0/A reverse-engineering exercise cannot capture, as these margins are intentionally conservative and are intended to account for the uncertainties inherent in early-phase design [103].

Since the actual design maturity and heritage of each item could not be independently verified, component-level Design Maturity Margins were assigned by analogy, following the standard ECSS Phase 0/A categorization of 5% for off-the-shelf items, 10% for modified off-the-shelf items, and 20% for newly developed or highly uncertain components [20]. Where the heritage could not be established with confidence, the higher end of the range was preferred, consistent with the ECSS principle that Design Maturity Margins are intended to cover "known unknowns". The 20% system-level margin applied on top of the nominal dry mass follows the same rationale at the spacecraft level, accounting for the "unknown unknowns" associated with reconstructing a flight-proven design from incomplete external sources rather than from an original, fully traceable engineering process [20].
Finally, no tabulated Earth-escape launch-capability value could be retrieved. For this reason, the maximum launchable mass reported in the tables was estimated as the total launch mass increased by a 10% margin, consistent with the launcher margin recommended by ECSS-E-TM-10-25A [101]. This value should therefore be read as a self-imposed conservative design threshold rather than a confirmed launcher capability value.

Overall, the gap between the reconstructed and the real launch mass is consistent with the ECSS Phase 0/A margin philosophy: the budget is not meant to reproduce the flight mass exactly, but to bound it conservatively given the level of design definition achieved in this reverse-engineering study.

References

[1] Masato Nakamura et al. "Akatsuki returns to Venus". In: *Earth, Planets and Space* 68 (2016), p. 75. DOI: 10.1186/s40623-016-0457-6.

[2] Masato Nakamura et al. "Planet-C: Venus Climate Orbiter mission of Japan". In: *Planetary and Space Science* 55.12 (2007), pp. 1831–1842. DOI: 10.1016/j.pss.2007.01.013.

[3] Masato Nakamura et al. "Return to Venus of the Japanese Venus Climate Orbiter Akatsuki". In: *Acta Astronautica* 93 (2014), pp. 384–389. DOI: 10.1016/j.actaastro.2013.07.027.

[4] Masato Nakamura et al. "Overview of Venus orbiter, Akatsuki". In: *Earth, Planets and Space* 63.5 (2011), pp. 443–457. DOI: 10.5047/eps.2011.02.009.

[5] Takehiko Satoh et al. "Development and in-flight calibration of IR2 2-μm camera onboard Japan's Venus orbiter, Akatsuki". In: *Earth, Planets and Space* 68 (2016), p. 74. DOI: 10.1186/s40623-016-0451-z.

[6] Takehiko Satoh et al. "Performance of IR2 in Venus orbit the first year". In: *Earth, Planets and Space* 69 (2017), p. 154. DOI: 10.1186/s40623-017-0736-x.

[7] European Cooperation for Space Standardization. *Space Engineering: Technical Requirements Specification*. Version Rev. 1. Third issue, Revision 1. European Cooperation for Space Standardization, June 2020.

[8] Mitsubishi Heavy Industries, Ltd. *H-IIA User's Manual*. Ver. 4.0. YET04001. Integrated Defense & Space Systems, Space Systems Business Development Department. Mitsubishi Heavy Industries, Ltd. Tokyo, Japan, Feb. 2015. URL: https://www.mhi.com/jp/products/pdf/manual.pdf.

[9] European Cooperation for Space Standardization. *Space Engineering: Verification*. ECSS-E-ST-10-02C Rev.1. Second issue, Revision 1. Establishes requirements for verification of space system products, including verification planning, execution, control, and close-out. ECSS. Noordwijk, The Netherlands, Feb. 2018. URL: https://ecss.nl/wp-content/uploads/2018/02/ECSS-E-ST-10-02C-Rev.1(1February2018).pdf.

[10] European Space Agency. *Space Debris Mitigation*. ECSS Training Program (ECSS-U-AS-10C, Part 2). ECSS-U-AS-10C training on space debris mitigation standards and requirements, including ISO 24113, ESA/ADMIN/IPOL(2014)2, and French Space Law (LOS). ESTEC, Noordwijk, The Netherlands, June 2016. URL: https://ecss.nl/wp-content/uploads/2016/09/ECSS-Training-L2-U10-Space-Debris-mitigation-Part22016-06-27.pdf.

[11] Chikako Hirose et al. "The Trajectory Design Strategies for Akatsuki Mission". In: *Transactions of the Japan Society for Aeronautical and Space Sciences, Aerospace Technology Japan* 10 (2012), To_3_1–To_3_5. DOI: 10.2322/tastj.10.To_3_1.

[12] Mark S. Ryne et al. "Navigation Support at JPL for the JAXA Akatsuki (Planet-C) Venus Orbiter Mission". In: *AAS/AIAA Astrodynamics Specialist Conference*. AAS 11-521. Girdwood, Alaska, USA, 2011. eprint: 20150006797. URL: https://ntrs.nasa.gov/citations/20150006797.

[13] Howard D. Curtis. *Orbital Mechanics for Engineering Students (Third Edition)*. Third Edition. Boston: Butterworth-Heinemann, 2014. ISBN: 978-0-08-097747-8. DOI: https://doi.org/10.1016/C2011-0-69685-1.

[14] A. S. Konopliv, W. B. Banerdt, and W. L. Sjogren. "Venus Gravity: 180th Degree and Order Model". In: *Icarus* 139.1 (1999), pp. 3–18. DOI: 10.1006/icar.1999.6086.

[15] A. Seiff et al. "Models of the Structure of the Atmosphere of Venus from the Surface to 100 km Altitude". In: *Advances in Space Research* 5.11 (1985), pp. 3–58. DOI: 10.1016/0273-1177(85)90197-8.

[16] David A. Vallado. *Fundamentals of Astrodynamics and Applications*. 4th. Hawthorne, CA: Microcosm Press, 2013. ISBN: 9781881883180.

[17] T. M. Donahue and C. T. Russell. "The Venus Atmosphere and Ionosphere and Their Interaction with the Solar Wind: An Overview". In: *Venus II: Geology, Geophysics, Atmosphere, and Solar Wind Environment*. Ed. by S. W. Bougher, D. M. Hunten, and R. J. Phillips. Tucson: University of Arizona Press, 1997, pp. 3–31.

[18] C. T. Russell, J. G. Luhmann, and R. J. Strangeway. "The Induced Magnetosphere of Venus". In: *Advances in Space Research* 38.4 (2006), pp. 741–748. DOI: `10.1016/j.asr.2005.03.018`.

[19] European Space Agency. *Venus Express: Mission Definition Report*. Tech. rep. ESA, 2003. URL: `https://sci.esa.int/documents/34571/36233/1567255504981-VenusExpressDefStudyRep.pdf`.

[20] European Space Agency. *Concurrent Design Facility Studies Standard Margin Philosophy Description*. Technical Note ESA-TECSYE-RS-006510. Issue 1, Rev. 2, 14/08/2017. ESA, 2017.

[21] Wiley J. Larson and James R. Wertz. *Space Mission Analysis and Design*. 3rd. Microcosm Press and Springer, 2005. ISBN: 978-1881883104.

[22] George P. Sutton and Oscar Biblarz. *Rocket Propulsion Elements*. 9th. Wiley, 2017.

[23] NASA. *Pressurization Systems for Liquid Rockets*. Tech. rep. SP-8112. NASA, 1975.

[24] James R. Wertz. *Spacecraft Attitude Determination and Control*. Dordrecht, Holland: D. Reidel Publishing Company, 1978. ISBN: 978-90-277-0959-2.

[25] Masato Nakamura and AKATSUKI Project Team. *Return to Venus of AKATSUKI*. Presentation at the 9th Venus Exploration Analysis Group (VEXAG) meeting. 2011. URL: `https://www.lpi.usra.edu/vexag/meetings/archive/vexag_9th/augSept11/presentations/Akatsuki.pdf`.

[26] Space Propulsion Website. *Space Propulsion Systems and Schematics*. Online resource. Used for propulsion system schematics analysis. Accessed: 2026-04-07. URL: `https://www.space-propulsion.com/`.

[27] Tomoaki Toda et al. "Flight Model Development of PLANET-C Telecommunication Subsystem". In: *Transactions of the Japan Society for Aeronautical and Space Sciences, Aerospace Technology Japan* 8.ists27 (2010). DOI: `10.2322/tastj.8.Tj_17`.

[28] International Telecommunication Union. *Radio Regulations*. Article 5, Deep-Space Research frequency allocations. 2020.

[29] Pasquale Cappuccio et al. "Probing solar wind velocity from simultaneous superior solar conjunction radio science experiments of BepiColombo and Akatsuki missions". In: *Monthly Notices of the Royal Astronomical Society* 533.2 (2024), pp. 1560–1567. DOI: `10.1093/mnras/stae1929`.

[30] Satoshi Narita et al. "Development of the AKATSUKI Telecommunications Subsystem for the Venus Climate Orbiter". In: *Proceedings of the 28th International Symposium on Space Technology and Science (ISTS)*. ISTS paper; no DOI available. 2011.

[31] Consultative Committee for Space Data Systems. *Telemetry Channel Coding*. Blue Book 101.0-B-6. CCSDS, 2002.

[32] Tomoaki Toda and Nobuaki Ishii. "In-Flight Validation of Akatsuki X-Band Deep Space Telecommunication Technologies". In: *Transactions of the Japan Society for Aeronautical and Space Sciences, Aerospace Technology Japan* 10.ists28 (2012). DOI: `10.2322/tastj.10.To_3_7`.

[33] Takeshi Imamura et al. "Radio occultation experiment of the Venus atmosphere and ionosphere with the Venus orbiter Akatsuki". In: *Earth, Planets and Space* 63 (2011), pp. 493–501. DOI: `10.5047/eps.2011.03.009`.

[34] Takeshi Imamura et al. "Initial performance of the radio occultation experiment in the Venus orbiter mission Akatsuki". In: *Earth, Planets and Space* 69 (2017), p. 154. DOI: `10.1186/s40623-017-0722-3`.

[35] Shinichiro Narita et al. "Operation scenario of PLANET-C: Venus Climate Orbiter (AKATSUKI)". In: *Proceedings of SICE Annual Conference 2010*. 2010, pp. 822–828. URL: https://ieeexplore.ieee.org/document/5603186.

[36] Japan Aerospace Exploration Agency (JAXA). *Spacecraft Attitude Control System Design Standard*. Tech. rep. JERG-2-510A. JAXA, 2007. URL: https://sma.jaxa.jp/TechDoc/Docs/E_JAXA-JERG-2-510A.pdf.

[37] European Cooperation for Space Standardization (ECSS). *Space Engineering: Spacecraft Attitude and Orbit Control*. Tech. rep. ECSS-E-ST-60-30C. ECSS, 2013. URL: https://ecss.nl/standard/ecss-e-st-60-30c-space-engineering-spacecraft-attitude-and-orbit-control/.

[38] Hiroyuki Toyota et al. "On-Orbit Operations of a Power System for Japan's Venus Explorer Akatsuki". In: *E3S Web of Conferences* 16 (2017), p. 18004. DOI: 10.1051/e3sconf/20171618004.

[39] Redwire Space. *Coarse Sun Sensor Pyramid Flysheet*. Product datasheet. 2021. URL: https://rdw.com/wp-content/uploads/2023/06/redwire-coarse-sun-sensor-pyramid-flysheet.pdf.

[40] A. Colagrossi and M. Lavagna. "Preliminary results on the dynamics of large and flexible space structures in Halo orbits". In: *Acta Astronautica* 134 (2017), pp. 355–367. DOI: 10.1016/j.actaastro.2017.02.020.

[41] D. Guzzetti and K. C. Howell. "Attitude dynamics in the circular restricted three-body problem". In: *Astrodynamics* 2.2 (2018), pp. 87–119. DOI: 10.1007/s42064-017-0012-7.

[42] F. Colombi, A. Colagrossi, and M. Lavagna. "Floquet modes and stability analysis of periodic orbit-attitude solutions along Earth–Moon halo orbits". In: *Celestial Mechanics and Dynamical Astronomy* 133.34 (2021). DOI: 10.1007/s10569-021-10030-y.

[43] NASA. *Maximum Torque and Momentum Envelopes for Reaction Wheel Arrays*. https://ntrs.nasa.gov/citations/20010084983. NASA Technical Reports Server. 2001.

[44] NASA. *Maximum Torque and Momentum Envelopes for Reaction Wheel Arrays*. https://ntrs.nasa.gov/citations/20090010227. NASA Technical Reports Server. 2009.

[45] NASA. *Sizing Spacecraft Momentum Storage Devices*. https://ntrs.nasa.gov/citations/19930015506. NASA Technical Reports Server. 1993.

[46] Glenn A. Macala. "Design of the Reaction Wheel Attitude Control System for the Cassini Spacecraft". In: *AAS/AIAA Space Flight Mechanics Meeting*. Paper AAS 02-121. San Antonio, Texas, USA, Jan. 2002. URL: https://ntrs.nasa.gov/citations/20210002002.

[47] Carson O. Mittelsteadt. "Cassini Attitude Control Operations – Guidelines Levied on Science to Extend Reaction Wheel Life". In: *AIAA Guidance, Navigation, and Control Conference*. NASA Technical Report 20150006920. Portland, Oregon, USA: American Institute of Aeronautics and Astronautics, Aug. 2011. URL: https://ntrs.nasa.gov/citations/20150006920.

[48] Northrop Grumman. *LN-200S / LN-200HPS Inertial Measurement Unit Datasheet*. IMU datasheet. 2024. URL: https://cdn.northropgrumman.com/-/media/Project/Northrop-Grumman/ngc/what-we-do/mission-solutions/assured-navigation/ln-200s-ln-200hps-imu/LN-200S-LN-200HPS-inertial-measurement-unit-imu-datasheet.pdf.

[49] H. Toyota et al. "Venus Climate Orbiter PLANET-C Solar Array Development". In: *8th European Space Power Conference*. Vol. 661. ESA Special Publication. ESA-SP-661. 2008, p. 36.

[50] H. Ooto et al. "Development of Lithium-Ion Battery for the Venus Climate Orbiter "PLANET-C"". In: *Proceedings of the 8th European Space Power Conference*. Ed. by H. Lacoste and L. Ouwehand. Vol. 661. ESA-SP. Paper ID 103. Constance, Germany, 2008. ISBN: 978-92-9221-225-4.

[51] Mitsubishi Electric Corporation. *Electrical Power Subsystem (EPS) Components*. Technical overview of DS2000 satellite platform EPS components. Mitsubishi Electric Space Systems.

URL: https://www.mitsubishielectric.com/bu/space/satellite_components/eps_components/index.html.

[52] Japan Aerospace Exploration Agency (JAXA). *JERG-2-310 Design Standard: Spacecraft Thermal Control System.* 2009. URL: https://sma.jaxa.jp/TechDoc/Docs/E_JAXA-JERG-2-310.pdf.

[53] N. Ishii et al. "Current status of the PLANET-C Venus orbiter design". In: *Advances in Space Research* 34.8 (2004), pp. 1668–1672. DOI: 10.1016/j.asr.2004.07.006.

[54] Bradford Space. *SuperNova PCDU.* satsearch. Aug. 19, 2025. URL: https://satsearch.co/products/bradford-supernova-pcdu.

[55] International Programme on Chemical Safety. *ICSC 0281 – Hydrazine.* WHO/ILO/UNEP. 2009. URL: https://www.inchem.org/documents/icsc/icsc/eics0281.htm (visited on 05/27/2026).

[56] Robert A. Braeunig. *Rocket Propulsion.* Rocket and Space Technology website. URL: http://www.braeunig.us/space/propel.htm (visited on 05/27/2026).

[57] Blue Canyon Technologies. *Reaction Wheel Data Sheet.* Product datasheet. 2023. URL: https://storage.googleapis.com/blue-canyon-tech-news/1/2023/02/BCT_RW_Data_Sheet.pdf.

[58] Japan Aerospace Exploration Agency (JAXA). *Inertial Reference Unit (IRU) Type III-C Environmental Resistance.* URL: https://www.ard.jaxa.jp/eng/library/database/pdf/e-gha001-2.pdf.

[59] *Space Engineering – Thermal Control General Requirements.* European Cooperation for Space Standardization (ECSS), 2020.

[60] PLANET-C Team. *Science Instruments and Targets of the Venus Climate Orbiter AKATSUKI (PLANET-C).* ISAS/JAXA. 2009. URL: https://www.stp.isas.jaxa.jp/venus/E_instrument.html.

[61] C. G. Justus et al. *Simple Thermal Environment Model (STEM) User's Guide.* Tech. rep. NASA/TM-2001-211222. NASA Marshall Space Flight Center, 2001. URL: https://ntrs.nasa.gov/api/citations/20020001443/downloads/20020001443.pdf.

[62] James R. Wertz et al. *Space Mission Engineering: The New SMAD.* Microcosm Press, 2011.

[63] Philippe Sivac and T. Schirmann. *The Venus Express Spacecraft System Design.* ESA SP-1295. European Space Agency (ESA), 2006. URL: https://sci.esa.int/documents/34571/36233/1567256526094-SivacWeb.pdf.

[64] *Thermal Emissivity Values.* No author listed; web resource. URL: https://www.design1st.com/Design-Resource-Library/engineering_data/ThermalEmissivityValues.pdf.

[65] Katja Janzer et al. "Thermal Control of Higher Power Applications on CubeSats". In: *Proceedings of the 69th International Astronautical Congress (IAC 2018).* Paper IAC-18-C2.7.11. Bremen, Germany: International Astronautical Federation (IAF), 2018.

[66] Hosei Nagano, A. Ohnishi, and Yuji Nagasaka. "Development of a lightweight deployable/stowable radiator for interplanetary exploration". In: *Applied Thermal Engineering* 31 (2011), pp. 3322–3331. DOI: 10.1016/j.applthermaleng.2011.06.012.

[67] Jonathan Schulster et al. "Blowing Hot & Cold: Flight Operations for Thermal Control on Mars & Venus Express". In: May 2008. ISBN: 978-1-62410-167-0. DOI: 10.2514/6.2008-3379.

[68] Beyond Gravity. *Thermal Insulation for Space and Launcher Applications.* Beyond Gravity. Apr. 2024. URL: https://www.beyondgravity.com/sites/default/files/media_document/2024-04/Thermal%20Insulation%20Satellites%20Launchers%20MLI%20Multilayer%20Brochure.pdf.

[69] SQUID3 Space, Inc. *Thermal Tape.* Product datasheet. SQUID3 Space, Inc. 2024. URL: https://373fb577-53de-42fe-911f-c45f83f6e446.usrfiles.com/ugd/373fb5_1146517c74934368b6176b36c0c pdf.

[70] Glavkosmos JSC. *Electric Heaters for Manned Spacecraft*. Glavkosmos JSC. URL: https://trade.glavkosmos.com/electric-heaters-for-manned-spacecraft/ (visited on 05/28/2026).

[71] Jellenie Rodriguez and Mary McCarthy. *Thermistor-Based Temperature Sensing System Explained*. Passive Components.eu. Based on an Analog Devices *Analog Dialogue* contribution. Jan. 2024. URL: https://passive-components.eu/thermistor-based-temperature-sensing-system-explained/.

[72] Japan Aerospace Exploration Agency (JAXA). *Spacecraft / Instruments / Venus Climate Orbiter AKATSUKI*. JAXA/ISAS Mission Page. Accessed: 2026-05-29. 2026. URL: https://akatsuki.isas.jaxa.jp/en/mission/spacecraft/.

[73] N. Okuizumi. *Development of the Spacecraft Structure for Akatsuki*. Part 4 of 'The Challenge of the Venus Orbiter Akatsuki', ISAS/JAXA Column. 2010. URL: https://www.isas.jaxa.jp/j/column/akatsuki/04.shtml.

[74] European Cooperation for Space Standardization (ECSS). *Space Engineering: Structural General Requirements*. Standard ECSS-E-ST-32C Rev.1. This Standard defines the mechanical engineering requirements for structural engineering. ECSS, Nov. 2008. URL: https://ecss.nl/standard/ecss-e-st-32c-rev-1-structural-general-requirements/.

[75] European Cooperation for Space Standardization (ECSS). *Space Engineering: Spacecraft Mechanical Loads Analysis Handbook*. Handbook ECSS-E-HB-32-26A. This handbook supports ECSS Standard: ECSS-E-ST-32C Rev.1 (15 November 2008). ECSS, Feb. 2013. URL: https://ecss.nl/hbs/active-handbooks/.

[76] Don Edberg and Willie Costa. *Design of Rockets and Space Launch Vehicles*. 2nd ed. Reston, VA: American Institute of Aeronautics and Astronautics, 2022. ISBN: 9781624106415. DOI: 10.2514/4.106422.

[77] Shoichiro Asada et al. "Launching Small Satellites on the H-IIA Rocket". In: *Symposium on Spacecraft Guidance, Navigation and Control Systems*. ESA Special Publication. ESA-SP-430, p. 6. URL: https://digitalcommons.usu.edu/cgi/viewcontent.cgi?article=1754&context=smallsat.

[78] N. Kawai et al. "Fracture behavior of silicon nitride ceramics subjected to hypervelocity impact". In: *International Journal of Impact Engineering* 38.7 (2011), pp. 542–545. DOI: 10.1016/j.ijimpeng.2011.01.003. URL: https://doi.org/10.1016/j.ijimpeng.2011.01.003.

[79] Shin-ya Murakami et al. *Venus Climate Orbiter Akatsuki SPICE Kernel Archive Bundle*. Version 4.0. JAXA Data Archives and Transmission System (DARTS), 2025. DOI: 10.17597/isas.darts/vco-00200. URL: https://doi.org/10.17597/isas.darts/vco-00200.

[80] B. T. C. Zandbergen. *Reader 1222 – Spacecraft Design*. Tech. rep. TU Delft, 2014. URL: https://research.tudelft.nl/files/247423772/Reader_1222_-_Spacecraft_Design_v2.3-1_total_incl_errata.pdf.

[81] European Space Agency. *Onboard Computers*. ESA Enabling & Support / Space Engineering & Technology / Onboard Computers and Data Handling. Technical description of satellite Onboard Computer (OBC) architecture, functions, and modular design. 2024. URL: https://www.esa.int/Enabling_Support/Space_Engineering_Technology/Onboard_Computers_and_Data_Handling/Onboard_Computers.

[82] European Space Agency. *Attitude and Orbit Control*. ESA Applications / Observing the Earth / Meteorological missions / MetOp. Service Module attitude and orbit control including propulsion for the MetOp satellite. 2024. URL: https://www.esa.int/Applications/Observing_the_Earth/Meteorological_missions/MetOp/Attitude_and_orbit_control.

[83] European Space Agency. *TT&C and PDT Systems and Techniques Section*. ESA Enabling & Support. Specialist section for Telemetry, Tracking and Command (TT&C) and Payload Data Transmission (PDT) systems. 2024. URL: https://www.esa.int/Enabling_Support/

Space_Engineering_Technology/Radio_Frequency_Systems/TT_C_and_PDT_Systems_and_Techniques_section.

[84] John E. Keesee. *Satellite Telemetry, Tracking and Control Subsystems*. MIT OpenCourseWare, 16.851 Satellite Engineering. Lecture notes from Fall 2003, Massachusetts Institute of Technology. Oct. 2003. URL: https://ocw.mit.edu/courses/16-851-satellite-engineering-fall-2003/35282c5f2e394c6567be2a64dd3d423a_l20_satellitettc.pdf.

[85] Jun'ichiro Kawaguchi, Akira Fujiwara, and Tono Uesugi. "Hayabusa—Its technology and science accomplishment summary and Hayabusa-2". In: *Acta Astronautica* 62.10-11 (May 2008). Hayabusa asteroid rendezvous, touch-down operations, guidance and navigation, and Hayabusa-2 follow-on mission, pp. 639–647. DOI: 10.1016/j.actaastro.2008.01.028. URL: https://www.sciencedirect.com/science/article/pii/S0094576508000441.

[86] National Aeronautics and Space Administration. *Fault Management Handbook*. NASA-HDBK-1002. Version Draft 2. Guidelines and recommendations for Fault Management (FM) of flight systems; co-sponsored by NASA SMD Discovery & New Frontiers Program Office and NESC. NASA. Apr. 2012. URL: https://s3vi.ndc.nasa.gov/ssri-kb/static/resources/636372main_NASA-HDBK-1002_Draft.pdf.

[87] BAE SYSTEMS. *RAD750™ Radiation-Hardened Microprocessor Component Datasheet*. BAE SYSTEMS Electronic Systems. Component datasheet for the RAD750 radiation-hardened PowerPC microprocessor. 2025. URL: https://www.baesystems.com/en-us/dam/jcr:c297f318-c618-4015-9399-adf76ac5cf55/16-f78-RAD750-Component-datasheet-2025-web.pdf.

[88] A. Burcin. *RAD750™: Radiation-Hardened PowerPC Microprocessor*. BAE SYSTEMS Presentation at MRQW 2002. Military and Aerospace Applications of Programmable Devices and Technologies Conference (MRQW). Dec. 2002. URL: https://web.archive.org/web/20090326020946/http://www.aero.org/conferences/mrqw/2002-papers/A_Burcin.pdf.

[89] Gordon Chin et al. "Lunar Reconnaissance Orbiter Overview: The Instrument Suite and Mission". In: *Space Science Reviews* 129.4 (2007), pp. 391–419. DOI: 10.1007/s11214-007-9153-y. URL: https://science.nasa.gov/wp-content/uploads/2024/01/lro-space-science-paper.pdf.

[90] Kenneth Li. "RAD750 SBC Usage for the Solar Dynamics Observatory (SDO) Program". In: *RAD750 User's Workshop*. NASA Technical Reports Server Document ID 20050244985. 2005. URL: https://ntrs.nasa.gov/api/citations/20050244985/downloads/20050244985.pdf (visited on 06/10/2026).

[91] European Space Agency. *OBC Mass Memory: Solid State Mass Memory Board/Module Integrated in OBC*. ESA Indico Event. Study presentation on integrating multi-user complex file-based mass memory into On-Board Computer (OBC) for space applications. 2024. URL: https://indico.esa.int/event/146/contributions/842/attachments/943/1131/03_-_OBC_Mass_Memory.pdf.

[92] Atsushi Yamazaki et al. "Ultraviolet imager on Venus orbiter Akatsuki and its initial results". In: *Earth, Planets and Space* 70.1 (2018). ISSN: 1880-5981. DOI: 10.1186/s40623-017-0772-6. URL: https://earth-planets-space.springeropen.com/articles/10.1186/s40623-017-0772-6.

[93] Takeshi Imamura. *Planned Observation by Venus Climate Orbiter*. Lecture notes. Jan. 2010. URL: https://www.cps-jp.org/~pschool/2010-01-04/04_Imamura/pub/Imamura_VCO_Kobe_final_with_reference.pdf.

[94] Naomoto Iwagami et al. "Initial products of Akatsuki 1-μm camera". In: *Earth, Planets and Space* 70.1 (2018). ISSN: 1880-5981. DOI: 10.1186/s40623-017-0773-5. URL: https://earth-planets-space.springeropen.com/articles/10.1186/s40623-017-0773-5.

[95] TEKTELIC Communications. *Data Throughput*. TEKTELIC Glossary. Definition of data throughput in the context of LoRaWAN® and IoT communications. Dec. 2023. URL: https://tektelic.com/what-it-is/data-throughput/.

[96] Jan Peleska and Oliver Schulz. "Reliability Analysis of Safety-Related Communication Architectures". In: *Unknown Conference Proceedings*. University of Bremen; railway control systems, communication architectures, fault hypotheses, mutant generation, UPPAAL model checking. 2025. URL: https://scispace.com/pdf/reliability-analysis-of-safety-related-communication-30b89ix6e9.pdf.

[97] B. Varga et al. "The Quick and the Dead: The Rise of Deterministic Networks". In: *IEEE Communications Society, Communications Technology News (CTN)* (Feb. 2021). Overview of IEEE 802.1 TSN, IETF DetNet, and 3GPP URLLC for deterministic networking. URL: https://www.comsoc.org/publications/ctn/quick-and-dead-rise-deterministic-networks.

[98] European Cooperation for Space Standardization. *Space Engineering: Interface and Communication Protocol for MIL-STD-1553B Data Bus Onboard Spacecraft*. ECSS-E-ST-50-13C. First issue; defines interface services and protocol elements for MIL-STD-1553B data bus in spacecraft applications. ECSS. Noordwijk, The Netherlands, Nov. 2008. URL: https://ecss.nl/wp-content/uploads/standards/ecss-e/ECSS-E-ST-50-13C15November2008.pdf.

[99] European Cooperation for Space Standardization. *Space Engineering: Gyro Terminology and Performance Specification*. ECSS-E-ST-60-21C. First issue; defines functional and performance requirements for space-borne gyros, excluding launch vehicle applications. ECSS. Noordwijk, The Netherlands, Feb. 2017. URL: https://ecss.nl/wp-content/uploads/2017/04/ECSS-E-ST-60-21C(15February2017).pdf.

[100] NEC. *Connecting Venus and Earth with a Flat Antenna: AKATSUKI*. URL: https://www.nec.com/en/global/ad/cosmos/akatsuki/02/index.html (visited on 06/04/2026).

[101] European Cooperation for Space Standardization. *Space Engineering: Engineering Design Model Data Exchange (CDF)*. ECSS-E-TM-10-25A. Technical Memorandum (non-normative) for model-based data exchange in concurrent design facilities, defining SEIM and SERDL for phases 0 and A. ECSS. Noordwijk, The Netherlands, Oct. 2010. URL: https://ecss.nl/wp-content/uploads/standards/ecss-e/ECSS-E-TM-10-25A20October2010.pdf.

[102] Japan Aerospace Exploration Agency. *Venus Climate Orbiter "AKATSUKI" (PLANET-C)*. JAXA Space and Astronautical Science (SAS). Latter phase in operation; launched May 21, 2010 on H-IIA Launch Vehicle No. 17; successfully inserted into Venus orbit on December 7, 2015 after initial main engine failure; equipped with five cameras for atmospheric observations. May 2010. URL: https://global.jaxa.jp/projects/sas/planet_c/.

[103] National Aeronautics and Space Administration. *NASA Systems Engineering Handbook*. NASA/SP-2016-6105 Rev 2. Supersedes SP-2007-6105 Rev 1 (December 2007). Provides guidance on implementing NPR 7123.1, including system design, product realization, and technical management processes. NASA. Washington, D.C., 2016. URL: https://explorers.larc.nasa.gov/2023ESE/pdf_files/NASA04.%20SysEng%20Handbook%20(NASA_SP-2016-6105%20Rev%202).pdf.